eport 3492

d Mixer-Nozzle

eld

perimental Study

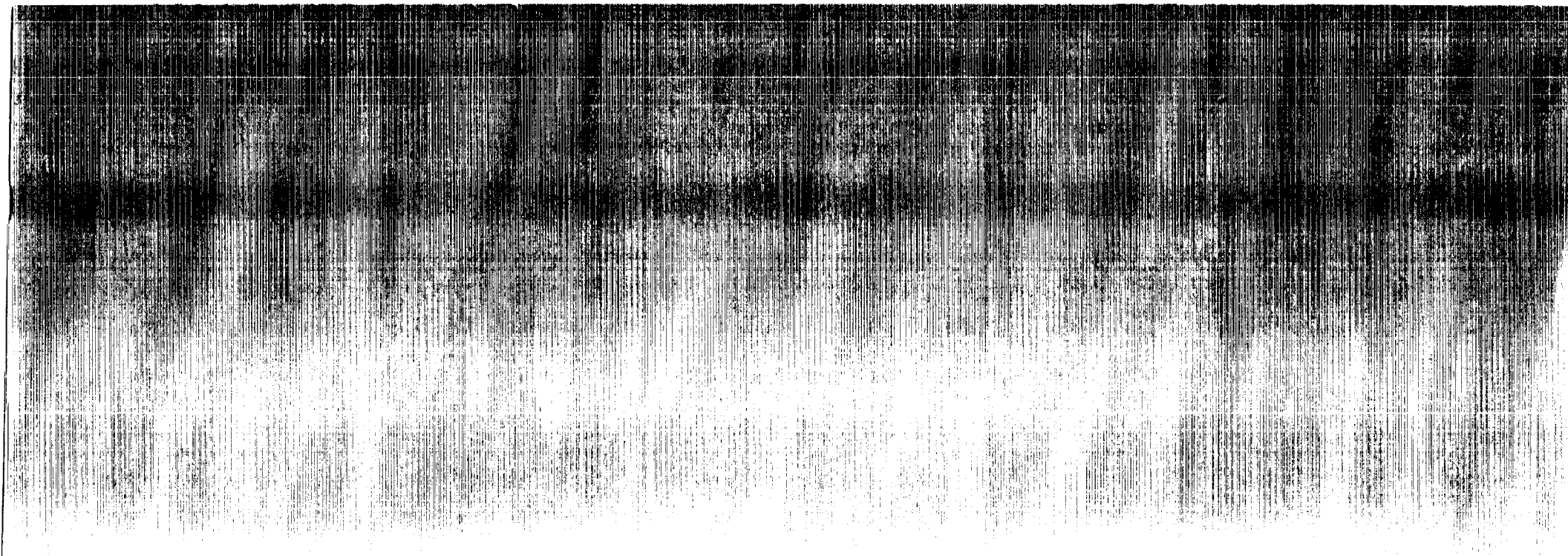

NASA Contractor Report 3492

Turbofan Forced Mixer-Nozzle Internal Flowfield

I - A Benchmark Experimental Study

Robert W. Paterson
United Technologies Research Center
East Hartford, Connecticut

Prepared for
Lewis Research Center
under Contract NAS3-20951

National Aeronautics
and Space Administration

Scientific and Technical
Information Branch

1982

TABLE OF CONTENTS

TABLE OF CONTENTS (Cont'd)

TURBOFAN FORCED MIXER-NOZZLE INTERNAL FLOWFIELD
I - A BENCHMARK EXPERIMENTAL STUDY

by

Robert W. Paterson

SUMMARY

An experimental investigation of the flowfield within a model turbofan forced-mixer nozzle was conducted in the United Technologies Research Center Jet Burner Test Stand. The test nozzle had a mixer lobe geometry representative of mixers installed in current turbofan engines. The objective of the study was to provide detailed velocity and thermodynamic state variable data for use in assessing the accuracy and assisting the further development of computational procedures for predicting the flowfield within mixer nozzles.

Tests were conducted at a primary stream pressure ratio of 2.6 and primary-to-secondary stream pressure ratio of 1.04. These values were representative of full-scale engine cruise conditions. Both cold and hot flow tests were performed. In the former, the primary-to-secondary stream total temperature ratio was unity. Hot flow tests were conducted at a temperature ratio of 2.5, which is representative of full-scale engine conditions.

Laser Doppler Velocimetry (LDV) was employed to define the three-dimensional mean and turbulent velocity fields within one segment of the nozzle at three axial cross-sections. One cross-section was located near the lobe exit plane, a second just downstream of the nozzle exit and a third at an intermediate axial position within the nozzle. Total pressure and temperature distributions were also defined at these locations. At the lobe exit plane, the velocity field was characterized by strong variations of axial velocity with azimuthal position and large radial velocities. At the nozzle exit, the velocity and temperature field was well mixed-out with nearly uniform distributions obtained in the azimuthal direction.

Velocity and temperature data suggested that the mixing process was dominated by secondary circulations which had length scales on the order of the lobe dimensions. These circulations were associated with strong radial velocities observed near the lobe exit plane. In addition to these circulations, a system of smaller scale vortices was observed within the mixer lobes. These vortices were postulated to have arisen from a horseshoe vortex formation process similar to that which occurs at the intersection of a bluff body and a wall boundary layer. While the role of these smaller vortices in the nozzle mixing process

is not presently clear, it is believed that the larger scale circulations described above represent the dominant nozzle mixing mechanism.

Hot and cold flow axial, radial and azimuthal Mach number distributions as well as total pressure distributions were found to be in close agreement throughout the nozzle flowfield. This would be predicted by isentropic flow theory although the flows considered were actually non-isentropic.

An LDV seeding development effort was conducted as part of this study resulting in a seeding system and optical arrangement that eliminated the seed particle lag problem that is commonly encountered in experiments involving strong acceleration fields. This permitted accurate velocity measurements to be acquired in the highly accelerated transonic flow region near the nozzle exit. A detailed analysis of data uncertainty was performed following guidelines established for "benchmark" experiments.

INTRODUCTION

Forced mixer nozzles are installed on some turbofan engines currently in production. It appears probable that mixers will find wider application in future engine designs as well as in newer versions of existing engines. From an engine design standpoint, the two important characteristics of mixer nozzles are the ability to achieve thrust augmentation as well as a more uniform nozzle exit plane velocity profile relative to either separate primary and secondary stream discharge configurations or common tailpipe configurations having no forced mixing element. Mixer thrust augmentation is important to overall engine performance while the degree of velocity profile uniformity affects the jet exhaust noise signature of the engine.

The magnitude of thrust augmentation achievable under ideal conditions can be defined as the thrust of a perfectly mixed-out flow less the combined thrust of primary and secondary streams discharged separately. A measure of ideal thrust augmentation is the difference between the mixed and unmixed stream thrust divided by the unmixed stream thrust. From a basic one-dimensional analysis, ideal thrust augmentation can be shown to be an increasing function of primary-to-secondary stream total temperature ratio, having a value of zero or less for a temperature ratio of unity. For typical engine temperature ratios, it is on the order of several percent. The degree to which this ideal value is achieved in practice depends upon the extent of mixing and the magnitude of loss associated with wall skin friction.

The degree of jet noise reduction achieved by an ideal mixer nozzle can be defined as the difference between the perceived noise level of a separate discharge configuration and that of a perfectly mixed out common discharge. Although this reduction cannot be calculated from first principles at present, theoretical considerations and experimental data show that the total noise power produced by jet exhaust turbulence is proportional to a characteristic jet velocity raised to the eighth power. Since this dependence on velocity is strong, reduction of primary stream exhaust velocity by secondary stream mixing is one of the few, and most effective means, to reduce jet noise from turbofan engines.

Despite the jet noise reductions achieved by the current generation of high bypass ratio engines relative to the earlier turbojet or low bypass engines, the jet exhaust noise contribution to overall engine noise remains important relative to meeting Federal noise regulations. Since future engines will be required to meet more stringent noise regulations and at the same

time show improved fuel economy (improved performance), it is likely that increased emphasis will be placed on the design of efficient, low-weight, forced mixers.

Because of the lack of a reliable analytical procedure for predicting thrust augmentation and the degree of exit velocity profile uniformity for arbitrary mixer lobe and downstream duct geometries, the mixer nozzle development process, to date, has been largely empirical. Emphasis has been placed on the correlation of thrust and jet exhaust noise data (or exit velocity and temperature profile data) obtained during testing of a wide variety of mixer geometries. While this approach has been reasonably successful, increased use of analytical methods as an adjunct to testing would be expected to accelerate the development of improved mixer designs and reduce development costs. Based upon advances made in the field of computational fluid dynamics in the last several years, it appears likely that a reliable and cost effective, three-dimensional, viscous mixer nozzle code can be developed for use in the engine design process.

Critical to this development process, however, is the availability of suitable experimental data. While presently existing thrust and exit plane total pressure and temperature data can be used to assess the overall accuracy and hence the usefulness of a given mixer calculation procedure, insufficient detail exists to identify the cause of failure of a given computational procedure to predict these properties. While such data, therefore, can assess code accuracy, they are not particularly useful for assisting code development. The usefulness of data of this nature is limited further in that mixer computational procedures are expected to be most accurate when data provides some specification of the turbulence field within the nozzle to help guide the turbulence modeling process.

A further significant limitation to existing mixer data is that a detailed definition of the lobe exit velocity, temperature and pressure fields is not available. Although the ultimate objective of mixer code development efforts is to provide a prediction based on the mixer nozzle geometry and upstream stagnation conditions, presently available computational procedures require specification of the lobe exit velocity, temperature and pressure fields. While these could be estimated to some degree from upstream conditions and the lobe geometry, use of approximate conditions as code input could preclude critical assessment of code accuracy. Measurement of all relevant lobe exit parameters, therefore, is essential in conducting a mixer code assessment experiment.

In summary, a need existed for an experimental investigation of the internal flowfield of a mixer nozzle in which the selection of measured parameters, the selection of measurement locations, the degree of spatial resolution and

the experimental accuracy were dictated by code input and assessment requirements. The present study was directed toward fulfilling these needs.

This report, as Volume 1 of a three volume series, constitutes a self-contained treatment of the "benchmark" model mixer experiment conducted for code assessment purposes. Volume 2, subtitled "Computational Fluid Dynamic Predictions" provides detailed comparisons of the present experimental results with prediction while Volume 3, subtitled "A Computer Code for 3-D Mixing in Axisymmetric Nozzles" describes the code used for prediction.

The author wishes to acknowledge helpful discussions with Edward M. Greitzer (MIT) regarding mixer nozzle aerodynamics and with Louis A. Povinelli (NASA) and Michael J. Werle (UTRC) relative to code assessment requirements. The assistance of William P. Patrick (UTRC) in LDV seeding system development, Veer N. Vatsa (UTRC) in data presentation, Steven W. Baker (UTRC) in LDV data acquisition, Charles Banning (UTRC) in rig heater development and discussions with Walter M. Presz, Jr. and Gerald E. Kardas (Pratt & Whitney Aircraft) are also appreciatively acknowledged.

LIST OF SYMBOLS

$b(x)$	Lobe width distribution
E_{Qi}	Percent error in quantity Q due to i'th parameter estimated at 0.95 confidence
E_Q	Total percent error in quantity Q estimated at 0.95 confidence
n	Number of validated LDV particle counts (velocity samples)
P_a	Test cell ambient pressure, N/m^2
P_A	Atmospheric pressure, N/m^2
P_{op}	Primary stream total pressure as indicated by probe used to set operating pressure, N/m^2
P_{os}	Secondary stream total pressure as indicated by probe used to set operating pressure, N/m^2
P_P	Primary stream average total pressure upstream of lobes, N/m^2
P_S	Secondary stream average total pressure upstream of lobes, N/m^2
P_T	Total pressure measured by probe, N/m^2
P_{R_T}	A reference total pressure selected from axial station 1 primary stream pressure measurements, N/m^2
r	Radial polar coordinate, zero on nozzle centerline, positive outward, cm
r_{MAX}	Radial position of inner surface of tailpipe or nozzle, cm
r_{MIN}	Radial position of nozzle plug surface, cm
$\bar{r}$	Radial distance from plug = $r-r_{MIN}$
R	Non-dimensional radial coordinate given by $\left(\frac{r-r_{MIN}}{r_{MAX}-r_{MIN}}\right)$ for station 1 and $\frac{r}{r_{MAX}}$ for all other stations
T_T	Total temperature measured by probe, deg Kelvin

T_{T_R}	A reference total temperature selected from axial station 1 primary stream temperature measurements, deg Kelvin
$u(t)$	Fluctuating velocity component of $\tilde{U}$ given by $\tilde{U} - \bar{U}$
u_x, u_r, u_ϕ	Root-mean-square values of turbulent velocity components in the axial, radial, and azimuthal directions, respectively, m/sec
$\overline{u_x u_r}$	Zero-time-delay cross-correlation of instantaneous axial and radial turbulent velocity components, m^2/sec^2
$\overline{u_x u_\phi}$	Zero-time-delay cross-correlation of instantaneous axial and radial turbulent velocity components, m^2/sec^2
U_x, U_r, U_ϕ	Mean velocity components in the axial, radial and azimuthal directions, respectively, m/sec
$\bar{U}$	Mean part of velocity, $\tilde{U}$, m/sec
U	Total velocity, m/sec
$\tilde{U}_1, \tilde{U}_2, \tilde{U}_3$	Magnitude of instantaneous velocity obtained with laser beam orientation, 1, 2 and 3, respectively, m/sec
$\tilde{U}_x, \tilde{U}_\phi$	Magnitude of instantaneous velocity in the x and ϕ directions, respectively, m/sec
v'	Sample root-mean-square velocity, m/sec
v'_p	Population root-mean-squre veloicty, m/sec
$\bar{V}$	Sample mean veloicty, m/sec
V_i	Velocity sample, "i", m/sec
V_p	Population mean velocity, m/sec
$\{V\}$	Velocity population
x	Axial polar coordinate, axis on nozzle centerline, positive in flow direction, cm
y	Dummy variable in Eq. (B1)

LIST OF SYMBOLS (Cont'd)

β	Laser beam orientation angle defined in Appendix B, radians
ΔP	Pressure differential between test cell and atmospheric pressure, N/m^2
ϵ	Laser beam deviation angle defined in Appendix B, radians
γ	Laser beam orientation angle defined in Appendix B, radians
λ	Normal distribution statistical parameter defined in Appendix C
λ_ℓ	Laser wavelength, 0.5415 μm
π	3.1416
ϕ	Azimuthal polar coordinate, zero corresponds to center of primary steam lobe, positive in counter-clockwise direction as viewed from downstream looking upstream, deg
σ	Standard deviation
σ_{u_x}	Standard deviation of LDV u_x measurement
σ_{U_x}	Standard deviation of LDV U_x measurement
θ	Laser beam orientation angle defined in Appendix B, radians
Ψ	Lobe inclination angle, deg

PREVIOUS INVESTIGATIONS

Despite the appreciable effort conducted to date in the development of engine mixers, neither experimental data nor descriptions of mixer design procedures are generally available in the open literature. In a series of recent publications by NASA Lewis Research Center (references 1-3), however, results of a joint analytical and experimental mixer research program have been documented. In the reference 1 paper by Povinelli, Anderson and Gerstenmaier, predictions of a three-dimensional, viscous calculation procedure, which solves a simplified form of the Navier-Stokes equations, were compared to data obtained with an eighteen-lobed and two twelve-lobed, bypass ratio four, model mixers. The primary-to-secondary total temperature ratio was low (1.35) relative to full-scale conditions; the corresponding pressure ratio was unity. Total temperature distributions were measured at the lobe exit and nozzle exit planes as well as at three intermediate planes; total pressure was measured at the lobe exit and nozzle exit.

Temperature data showed that "hot spots" of varying shape, depending on the mixer configuration, existed at the nozzle exit. An interesting observation was that the hottest portion of the spots at the exit plane existed at an outer radial position corresponding roughly to the peak of the primary lobes while the inner radial regions contained cooler fluid which had its origin in the secondary stream lobes. This indicated the existence of large-scale secondary flows in the radial-azimuthal plane and suggested that they contributed significantly to the mixing process. Preliminary LDV secondary flow data from the present study, obtained at the lobe exit plane, were cited as further support for this hypothesis regarding the role of large-scale secondary flows in determining the degree of mixing.

In addition to these experimental results, a mixer calculation procedure was applied to predict flow development within the nozzle. Secondary flows were not input as initial conditions at the lobe exit and it was concluded that accounting for these would improve agreement between analysis and data.

In the reference 2 paper by Anderson, Povinelli and Gerstenmaier, additional comparisons between analytical predictions and experiment were reported for one mixer configuration. In this case, flow angularity measurements were obtained at the lobe exit plane. These data were used to develop a representation, termed a "generic" representation, of the lobe exit plane secondary flowfield which was then included in the code initial conditions. Predictions employing these initial conditions were found to yield much better agreement with data than those in which lobe exit plane secondary flows were neglected.

In the reference 3 report by Anderson and Povinelli, the effect of including additional lobe exit plane vorticity, associated with a "passage vortex"

in the primary stream at the base of the fan trough, was investigated. Comparisons with data were made for three mixer configurations at a stream temperature ratio of 1.35 and one configuration at a ratio of 2.5. Inclusion of this "passage vortex", of assumed strength, improved agreement with data relative to a calculation which included only the larger scale secondary flowfield. The latter calculation was, in turn, more accurate than an "ideal" calculation in which lobe exit secondary flows were neglected. From these code prediction comparisons it was concluded that pressure-driven secondary flow patterns within the nozzle play a dominant role in the mixing process.

Another recent model experimental study of mixers was reported by Shumpert (reference 4). Four mixer geometries, consisting of two multi-lobe chute configurations, one injection and one vortex generator configuration were tested. The latter two models would not be expected to induce strong radial velocities. The models were operated at a bypass ratio of six over a primary pressure ratio range of 1.1 to 3.0 and primary-to-secondary temperature ratio range of 1.0 to 2.7. In addition to changes in these parameters, the length of the mixing duct within the models was varied over a length-to-diameter range of 0.7 to 2.5. Thrust and exit plane total temperature and pressure distributions were measured. No measurements were acquired within the nozzle. Exit plane velocity distributions (presumably total velocity) were calculated although it is uncertain as to how static pressure was determined within the three-dimensional velocity field at the exit.

Of the models tested, Shumpert found the multi-lobe chute models to be significantly more effective in promoting mixing than the injection and vortex generator models. Mixing effectiveness, defined in terms of a temperature mixing function, was found to be insensitive to pressure ratio and a weakly increasing function of temperature ratio. As would be expected, mixing effectiveness was observed to increase with increasing mixing duct length.

In a recent study reported by Kozlowski and Kraft (reference 5), a series of model mixer nozzles were tested to determine the effect of various geometry variables such as the number of lobes, degree of radial lobe penetration, tailpipe length, lobe cutback angle and lobe scalloping. Trends were established for each variable, however, complicated interactions among the geometry variables would be expected to preclude extrapolation of trends to designs involving multiple parameter variations. From a diagnostic standpoint, a total pressure contour at the exit of one mixer configuration showed penetration of secondary stream fluid into the inner region of the primary lobe trace as was noted in reference 1. Another recent mixer parameter variation study was reported by Kuchar and Chamberlin (reference 6). As in the case of reference 5, lobe scalloping was found to improve performance. The degree of lobe penetration was observed to have a strong effect on mixing although the largest penetration designs experienced lobe separation which increased loss. As in

the case of the reference 5 study, extrapolation of trends to configurations outside the test matrix would not be expected to be reliable. Moreover, it is uncertain whether resultant conclusions (such as the effect of lobe number) are specific to the particular test conditions and geometries or are more generally applicable.

The first analytical and experimental study of mixer nozzle flows was reported by Paynter, Birch, Spalding and Tatchell in 1977 (reference 7). A three-dimensional, viscous analysis was applied to predict exit plane total temperature and total velocity distributions for both a full-scale free mixer and a lobed mixer as well as a model scale lobed mixer. Initial conditions were not measured although an approximate scheme was applied to input radial velocities at the lobe exit. Agreement between predictions and data at the nozzle exit plane was encouraging given the lack of experimentally determined initital conditions. Based on the sensitivity of predictions to inlet plane secondary flow assumptions noted in references 2 and 3, the degree of agreement achieved in the reference 7 study probably resulted from the inclusion of approximate radial velocities at the initial station.

In summary, several experimental model studies directed toward overall performance gain have been performed; these demonstrate certain trends which can probably be interpolated within the specific text matrix but not extrapolated. Two joint analytical and experimental efforts have shown that three-dimensional, viscous codes are at a sufficient stage of development that they can be applied to lobed mixer nozzles with encouraging results. Accurate knowledge of lobe exit conditions, particularly secondary flow velocity components, however, appears essential. This, in turn, indicates the need for a method to predict the lobe exit flowfield accurately based on the upstream conditions and lobe and nozzle geometry. Furthermore, it indicates the need for experiments, such as that reported here, in which the three-dimensional, lobe exit velocity field is defined in detail.

PRESENT STUDY

Objectives

The overall objective of the present study was to provide a set of model forced turbofan mixer nozzle internal flow data to assess, critically, the accuracy and further assist the development of computational procedures for predicting mixer nozzle flows. This objective translated into a specification of a minimum number of measurements of various quantities at specified locations with a prescribed degree of maximum experimental uncertainty. A second objective was to attempt to gain insight into the dominant nozzle mixing mechanism(s) through supplementary experimentation and analysis of data.

Approach

Considering the code assessment objective, a model turbofan forced mixer nozzle having a mixer lobe geometry representative of those used in current production low-bypass-ratio commercial engines, was selected as the test model. Although this small model scale was expected to cause difficulty in surveying the internal flow of the nozzle, the concept of testing one or several nozzle segments at larger scale in the annular geometry representative of engines appeared likely to fail to meet objectives. This is because segment end-wall phenomena such as corner secondary flows and thick boundary layers, not present in the annular geometry, would be expected to alter the lobe exit and downstream duct flow significantly.

The parameters selected for measurement within the mixer flowfield were the three mean velocity and three turbulent velocity components, two of the three second-order turbulent velocity component correlations, total pressure, total temperature, wall static pressures, and primary and secondary stream mass flow rates. No attempt was made to measure static pressure within the nozzle flow-field since error bounds could not be estimated reliably. Similarly, direct measurement of static temperature was not considered feasible. The mean flow-field parameters selected for measurement ($\vec{U}$, P_T and T_T) were sufficient to define, uniquely, Mach number and all thermodynamic state variables.

Although a hot flow test represented the test case of practical interest, it was also decided to conduct a cold flow test program in which primary and secondary stream total temperatures were equal. This was motivated by the desire to provide a less demanding test case from the standpoint of code assessment and thereby assist in determining the cause(s) of any possible failure in the hot flow prediction. From the experimental viewpoint, the cold flow test series was considered important as a considerably simpler operating

mode in which to develop the basic experimental approach. Furthermore, significant differences between cold and hot flow total pressure and Mach number data, particularly at the lobe exit plane, would point to a probable measurement problem. From both code assessment and experimental technique development viewpoints, the cold flow test series proved to be an important element of the overall program.

Relative to the selection of instrumentation for the experiment, the combination of significant secondary circulation, transonic flow, and spatially varying total temperature (for hot flow testing) precluded the use of any technique (such as hot wire anemometry) except LDV or laser two-spot (time of flight) velocimetry for definition of the velocity field. LDV was selected rather than the two-spot technique since the more extensive use of LDV has led to a clearer identification of potential sources of error.

To maximize the degree of spatial resolution, it was decided to investigate the flow within a segment corresponding to one-mixer lobe (one-half of a primary and one-half of a secondary lobe). This constituted the smallest mixer element that could be used in conjunction with symmetry arguments to reconstruct the entire nozzle flow at the same cross-sectional position. The initial test plan specified a total of approximately one-hundred twenty-five (125) LDV measurement locations for the complete cold and hot flow program. The need to more clearly identify the magnitude of velocity gradients and otherwise assist interpretation of data led to an approximate doubling of the number of test locations.

In addition to the questions of parameter selection, measurement locations, etc., the code assessment objective directed that a significant degree of redundancy be built into the program. Redundancy, arising both from replication of data as well as the use, in LDV measurements, of two independent means to measure the same parameter, formed a statistically defendable means to establish uncertainty estimates. These uncertainty estimates complemented those derived by the traditional forward calculation in which estimated uncertainties in individual variables (taken at 20:1 odds) are multiplied by the partial derivatives of the data reduction equation and combined on a mean-square basis to estimate overall uncertainty of a derived quantity.

To assist meeting the second program objective of gaining further insight into nozzle mixing mechanisms, a vorticity meter, tufts and surface flow visualization were used to study the nozzle internal flowfield. Qualitative data derived in this manner, as well as code assessment data, were examined to permit hypotheses to be drawn regarding mixer nozzle mixing mechanisms.

DESCRIPTION OF THE EXPERIMENT

Experimental Arrangement

Test Model - Photographs of the test nozzle installation, with and without the convergent nozzle installed, are shown in figure 1. Figure 2 provides a detailed cross-sectional view of the nozzle in a plane passing through the nozzle centerline.

The mixer consisted of twelve primary stream lobes centered at intervals of 30 deg in azimuth which projected into the secondary stream annulus and a corresponding twelve secondary stream lobes which extended into the primary annulus. The lobes were cut back at an angle of 12 deg in the axial-radial plane. The inward slope of the straight secondary stream lobe was steep (22 deg) while the initital 19 deg outward slope of the primary stream lobe was reduced to approximately 5 deg at the lobe trailing edge by a contour which had a concave inward curvature. Additional lobe geometry details are given in figure 3 including LDV beam intersection data discussed subsequently. Primary and secondary stream total pressure rakes were located upstream of the lobes to assess lobe entrance flow uniformity. A swirl vane assembly and a simulated turbine exit guide vane assembly were located downstream of the rakes in the primary stream.

Downstream of the lobes was a "mixing duct" region bounded on the outside by the tailpipe and convergent nozzle and initially on the inside by the nozzle plug, which terminated within this duct. A nozzle with a convergence angle of 14.9 deg was connected to the aft tailpipe.

Test Cell - This study was conducted at the UTRC Jet Burner Test Stand on a test cell centerline used for model turbofan nozzle thrust measurements. This centerline is capable of providing a steady-state air supply of 4.5 kg/sec at a pressure of 2.9×10^6 N/m^2 and heated air in the primary stream at temperatures and flow rates exceeding the present test requirements of 780°K and 1.4 kg/sec. The air is dried to produce a dew point of less than 250°K; dry air is required in cold flow testing to prevent condensation on LDV seed particles which act as nucleation sites. Such condensation introduces severe particle lag problems. A sketch of the rig is given in figure 4.

Total mass flowrate was measured by a choked ASME flow nozzle at the centerline entrance. The flow was then divided into a primary stream and secondary annular stream with relative stream flowrates controlled by the position of a remotely actuated splitter plate (throttle). This throttle consisted of a perforated annular plate which was fixed and an adjacent plate of similar design that could be rotated to change the effective open area of

the secondary passage. The primary stream mass flowrate was measured by a venturi. Further downstream, a propane heater with a water-cooled flame holder heated the primary stream to the prescribed set temperature.

Exhaust from the test model exited the cell through a duct containing a butterfly throttle valve. The valve position in conjunction with the rate at which air was introduced into the cell by the ventilation system determined the cell ambient pressure. The probe and LDV data acquisition system, including the on-line LDV computer, were located in a separate control room from which the rig, traversing systems, and LDV seeder were operated.

Test Program Definition

Selection of Measured Variables - Directly measured and derived variables were selected based upon code assessment requirements. A calculational procedure for predicting three-dimensional mixing in axisymmetric nozzles from the lobe exit to the nozzle exit requires the vectorially decomposed mean velocity field and the pressure and temperature field as input. Depending on the complexity of the turbulence model used, some degree of specification of the second order velocity-correlation tensor at the starting location is also needed. Such a code can also be expected to require a definition of wall and lobe exit boundary layers when operated in its most complete form. The desired output of the calculational procedure is a complete specification of the mean velocity field and thermodynamic variables at downstream locations, and depending on the turbulence model, some turbulence field properties.

Based on these and experimental considerations, the three orthogonal mean velocity components, total pressure, total temperature and wall static pressures were selected as the mean variables to be measured directly. It did not appear feasible to measure static pressure and temperature accurately within the three-dimensional, transonic nozzle flowfield although both could be derived from the measured variables.

All components of the second order correlation tensor were also measured with the exception of the radial-azimuthal correlation ($\overline{u_r u_\phi}$) which was significantly more difficult to determine and was not considered critical to the computations.

Test Conditions - The test conditions selected for the experiment were a primary stream pressure ratio of 2.6, a primary-to-secondary stream total pressure ratio of 1.04, a primary-to-secondary temperature ratio of 2.5 for hot flow testing and a temperature ratio of unity for cold flow testing. These pressure ratios and the hot flow temperature ratio are representative of full-scale engine cruise conditions.

Operating conditions were set using a single set of probes and checked by a second set. The total pressure probes were located in the primary and secondary pressure rakes shown in figure 2 upstream of the lobes. Primary stream total temperature was measured within a primary lobe at a position diametrically opposite the test lobe. Secondary stream total temperature was measured upstream of the pressure rake. Appendix A provides a detailed discussion of the procedures used to set operating conditions including uncertainty estimates and a table of nozzle "reference" operating conditions.

Selection of Measurement Locations - To meet code assessment requirements, a "benchmark" mixer experiment must, as a minimum, provide data at a location to start the computation and at a relevant downstream location to check results. Axial measurement station 1 (figure 2), just downstream of the lobe exit, was selected to meet the former need and station 3, just downstream of the nozzle exit was chosen for the latter. Station 3 was located downstream of the nozzle exit plane to provide clearance for the incident laser beams.

A complete set of data were also obtained at an intermediate plane (station 2) within the tailpipe region. This provided an assessment of code accuracy in predicting the initial mixing out of the lobe-induced velocity gradients at low Mach number and avoided the transonic flow and convergence effects present in the nozzle region. Some data were also acquired in the plane of the nozzle exit (station 4). These measurements, in conjunction with station 3 measurements, permitted assessment of code prediction accuracy in the unbounded and highly accelerated flow region extending from the plane of the nozzle exit to station 3 (0.76 cm downstream). Measurements at station 1 were taken in a plane perpendicular to the nozzle axis rather than in the curvilinear coordinate system used for computations. Measurements in the latter system would have required a larger LDV viewing window with greater discontinuities at the wall-window junction.

At each of the three principal axial measuring stations (1, 2 and 3), data were acquired over one lobe segment of the nozzle encompassing one-half of a primary and one-half of a secondary lobe. At inlet station 1, velocity, pressure and temperature measurements were obtained along five radial lines differing in azimuth angle, ϕ, by 3.75 deg (figure 3, part (a)). At intermediate station 2 and plume-plane station 3, data were acquired along three radial lines (ϕ = 0, 7.5 and 15 deg), except for total temperature measurements at intermediate station 2, which were obtained with the finer azimuthal increment for reasons discussed subsequently. The finer resolution at inlet station 1 was considered desirable since gradients in the azimuthal direction were largest at this location and a failure to provide sufficient code input data could account for subsequent code prediction errors at downstream locations.

The LDV radial measurement increment was selected to provide a minimum of eight measurements at each azimuthal position. For temperature and pressure measurements, the resolution was increased by a factor of approximately four. The LDV measurement grid was necessarily reduced relative to the pressure and temperature grids since the vectorial decomposition of the velocity field required six laser beam orientation measurements for each spatial location. The more detailed temperature and pressure measurements were intended not only to give a more complete representation of the flowfield, but also to provide some indication of lobe surface boundary layer thicknesses and plug and tailpipe boundary layer thicknesses.

Instrumentation

Flowfield Measurements - Total pressure and temperature data were acquired with conventional stagnation probes as described in Appendix A. For reasons discussed previously, LDV was employed for velocity measurements. The LDV system consisted of an Argon-ion laser, optical system, counter-type signal processor and on-line computer for data reduction; all units are commercially available.

The LDV was operated in a dual beam or "fringe" mode in which light from the intersection of two incident beams is heterodyned to detect the Doppler shift from an injected seed particle moving at the local, instantaneous fluid velocity. In this mode, the LDV measures the velocity component in the plane of the incident beams that is perpendicular to the bisector of the beams. The effective shape of the resultant measurement volume is an ellipsoid with major axis in the direction of the bisector of the beams. Sketch A below shows these features and the theoretical measurement volume dimensions for the various axial stations assuming that the ellipsoidal surface is defined by the points where Doppler signal amplitude is $1/e^2$ of its centerline value. No direct measurement of the effective measuring volume size was made; it can be affected by signal amplitude and the signal processor threshold level setting. As an indication of the reasonable measurement resolution obtained, the ratio of the maximum measuring volume dimension, ℓ, to primary lobe width varied from a minimum of approximately 0.05 at stations 1 and 2 to 0.26 at station 3.

Figure 5 shows the LDV optical system employed. Stations 1 and 2 measurements were obtained with backscatter collection while most station 3 and 4 measurements were carried out in forward scatter. A serious seed particle lag problem was encountered in the initial stage of the present study at axial station 3 due to the high accelerations in this transonic flow region. This resulted in axial velocity measurement errors on the order of 20 percent. Forward scatter collection in conjunction with seeding system development efforts were found necessary to eliminate this lag problem. This development effort is described in Appendix E.

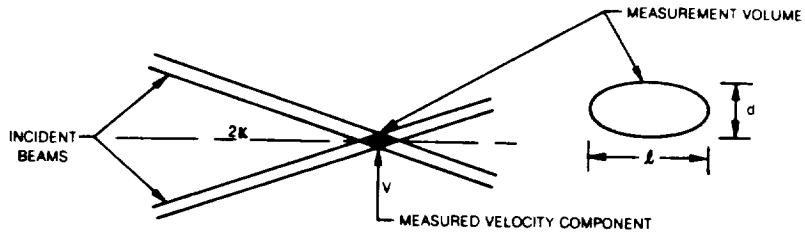

MEASURING VOLUME DIMENSIONS

STATION	ℓ, mm	d, mm
1, 2	0.75	0.072
3	4.2	0.173

SKETCH A — LDV BEAM ARRANGEMENT

A relatively wide angle lens (κ = 5.5 deg) was used at station 1 since it was found to suppress noise associated with reflections from the plug. The 2.27X beam expander shown in figure 5 was used to reduce measuring volume size (theoretically by a factor of 2.3 in minor axis and 5 in major axis) and in conjunction with the wide angle lens, yield a small measuring volume having a maximum dimension equal to five percent of the lobe width. A longer focal length transmitting lens (600 mm, κ = 2.4 deg) was required at station 3 since the Doppler frequency, given by $2V\sin\kappa/\lambda_\ell$, exceeded the 100 MHz range of the signal processor. This yielded a larger but acceptable measuring volume having a maximum dimension approximately six times smaller than the heads of the total pressure and temperature probes; without the beam expander the ellipsoid major axis would have been excessive, approximately four percent of the nozzle exit plane radius. A 250 mm focal length was retained for the collection lens to provide a large collection solid angle and therefore higher signal intensity.

The LDV system counter processor employed a 4, 5, 8 zero crossing period count for validation. To achieve acceptable data rates, the validation circuit was set to accept all data for which the period ratios were within 3 percent of expected values. Tests conducted with the most stringent limit available (0.8 percent) showed no appreciable differences. Based on the uncertainty analysis given in Appendix C, 1000 particle counts were employed in nearly all measurements to permit the on-line computer to construct velocity probability density distributions. Additional details concerning LDV data processing are given in Appendix B.

The material introduced to provide light scattering centers for LDV measurements was an Aluminum Oxide powder with a nominal particle size of 0.3 microns. A silica agent was dispersed in the powder to minimize particle agglomeration. As shown in figure 4, the seed was injected into the rig upstream of the primary-secondary split. Appendix E contains additional information regarding seed system development and particle size measurement within the flow.

Vorticity Surveys - Tufts and a UTRC fabricated vorticity meter were employed to survey the nozzle internal flow. The meter consisted of a 0.7 cm dia, 4 bladed, paddle wheel mounted on a probe support. A hot-wire, paddle-wake detector permits wheel rotational speed to be determined by spectrum analysis. When the axis of the probe is aligned with the local flow direction, the theoretical angular velocity of the paddle wheel, in the limit of infinitesimal paddle wheel diameter and zero internal friction, is one-half the component of vorticity in the direction of the probe axis. The paddle wheel will not rotate in irrotational flow regions. In the present study, the meter was used for qualitative purposes to establish boundaries of rotational flow regions.

Measurement Approach

Pressure and Temperature - Pressure and temperature probe traverses were conducted along radial lines fixed in azimuth relative to the tailpipe and nozzle. The mixer lobe assembly was sequentially rotated within the stationary tailpipe and nozzle in the required increments to generate data along the various lines of constant azimuth shown in figure 3. All measurements were acquired within one primary-secondary lobe segment. This arrangement provided an accurate and reproducible azimuthal survey since the traverse system remained fixed in space and the various mixer lobe azimuthal orientations could be set by a coded system of set screws which engaged the fixed primary supply duct. An electrical circuit was employed to detect probe contact with nozzle surfaces. This provided unambiguous radial positioning and was essential for hot flow testing where thermal expansion of the primary supply pipe shifted the nozzle plug downstream producing a corresponding increase in R_{MIN} at station 1. Additional details concerning probe measurements are given in Appendix A.

Laser Doppler Velocity Measurements - Figure 6 shows the six beam and lobe orientations used to obtain velocity data at each measurement location. Part (a) shows the horizontal line along which the measuring volume was traversed to acquire axial and azimuthal velocity component data. From the three beam orientation planes shown (1, 2 and 3), differing by increments of approximately $\pi/4$ radians, equations given in Appendix B permitted all required axial and azimuthal velocity quantities to be determined. As in the case of probe measurements, the traverse line was held fixed in space and the mixer lobe rotated within the nozzle to obtain data along radial lines of varying azimuth, ϕ. For axial-radial velocity measurements, the test lobe was rotated 90 deg to a vertical position, as shown in part (b). Three additional beam orientations (4, 5 and 6) were used to define required axial and radial quantities along the vertical traverse line.

For the beam orientation system employed, axial velocities were sufficiently large relative to instantaneous azimuthal and radial velocities that directional ambiguity in the azimuthal and radial velocity measurements did not occur. That is, the vector formed by the sum of axial and secondary flow instantaneous velocity components aligned along the perpendicular bisector of the beam in the plane of the beams always had a positive downstream component. A Bragg cell was therefore not required to frequency shift one of the heterodyned signals relative to the other to avoid folding of the probability density distribution when measuring azimuthal and radial velocities of varying sign.

The advisability of rotating the test lobe 90 deg to acquire radial velocity data can be questioned since this assumes azimuthal symmetry in the upstream flow. Other options which did not involve lobe rotation were: (1) retention of the horizontal traverse perpendicular to the axis with beams introduced vertically or (2) use of a horizontal traverse with beams skewed upstream relative to the perpendicular. The first would have required a mirror arrangement while the latter would have produced large uncertainties due to shallow angle constraints imposed by the viewing window. Based on possible vibration problems with the former option, errors with the latter, and the fact that axial velocity was found to be similar (within uncertainty bounds) for horizontal and vertical lobe measurements at the same lobe position, the lobe rotation approach was selected.

To determine the three mean velocities and five turbulent correlations, a total of five LDV beam orientations were required as indicated by the laser data reduction equations given in Appendix B. This would have produced three redundant (but independent) measurements of U_x. The six beam approach described above produced four redundant measurements of U_x and one of u_x. This permitted standard deviations to be calculated for u_x as well as U_x, thereby yielding a means to estimate uncertainties for all eight of the measured velocity quantities.

Additional Flowfield Diagnostics - Tufts and surface flow visualization were used to survey for regions of flow detachment in the mixer lobes. A vorticity meter was employed to identify regions of rotational flow within the mixer lobes and tailpipe regions. These qualitative studies were conducted to assist interpretation of the detailed flowfield measurements.

THEORETICAL CONSIDERATIONS

Implications of the Munk and Prim Substitution Theorem

The Munk and Prim substitution theorem provides insight into the kinematics and dynamics of the mixer nozzle flow field. The theorem applies to the adiabatic, steady, inviscid flow of a perfect gas. Under these conditions the flow is isentropic and the stagnation enthalpy and total pressure are constant along streamlines, although they may be different for different streamlines. As summarized by Tsien and Emmons (reference 8), the theorem requires that: "if a steady flow field is determined for specified body and stagnation enthalpy distribution among the streamlines, then a change in the stagnation enthalpy distribution requires only a change of the velocity field by a factor equal to the square root of the ratio stagnation enthalpy. The same pressure field will then keep the flow in equilibrium." This is equivalent to the statement that the vectorial Mach number and static pressure are invariant with respect to changes in upstream stagnation temperature distributions.

If the mixer internal flow were adiabatic and inviscid, therefore, the radial, azimuthal and axial Mach number and pressure distributions within the nozzle would be similar for both hot and cold flow test conditions. In the limit of adiabatic and inviscid flow, which would be expected to be reasonable assumptions for flow through the mixer lobes, hot and cold flow pressures, Mach numbers and streamlines would be identical. The velocity vector distribution at the exit of the primary lobes would be similar for hot and cold flow, differing only in magnitude by the square root of the hot-to-cold stagnation temperature ratio, i.e., 1.62. Based on the above, hot and cold LDV velocity component data at Station 1 have been compared and plotted on a Mach number basis in the following section.

Downstream of the lobes, the flow is rotational in the shear layers that emanate from the lobes. Vorticity contained in these shear layers diffuses as the fluid convects downstream, causing the regions of rotational flow to occupy an ever increasing proportion of the nozzle cross-section. In this case, the inviscid assumption invoked above is clearly violated and reasoning based on the substitution theorem can be questioned. As discussed in the section entitled "Nozzle Mixing Mechanisms", however, large scale convective transport by the essentially inviscid secondary flows set up by the lobe geometry appears to be a dominant factor in the mixing process and may be more important to overall mixing effectiveness than the smaller scale transport by turbulence. If this were true, then the substitution theorem indicates that hot and cold flow component Mach number distributions will be qualitatively similar. This is examined in the section entitled "Results and Discussion".

Mixing Mechanisms in Turbulent Flow

The transport of a scalar quantity, denoted by Θ, such as axial momentum or heat, in a turbulent steady flow can be described by an equation of the form (Hinze, reference 9):

$$\bar{U}_i \frac{\partial \bar{\Theta}}{\partial x_i} = \frac{\partial}{\partial x_i} \left(\epsilon \frac{\partial \bar{\Theta}}{\partial x_i} - \overline{u_i \theta} \right) + \bar{F} \qquad (1)$$

where θ and u_i are the unsteady parts of Θ and U_i, respectively. $\bar{F}$ is a force and ϵ is a molecular transport coefficient. The turbulent transport term $\overline{u_i \theta}$ can further be viewed as comprised of large scale convective transport and small-scale gradient-type diffusion, or symbolically:

$$\overline{u_i \theta} = \overline{u_i^* \theta} + \overline{V_i \theta} \qquad (2)$$

where u_i^* and V_i represent the small-scale and large-scale parts of the turbulence velocity. In free turbulent shear flows such as the wake flow of a cylinder or a jet, the larger scale bulk convection term is considered responsible for the broadening of the turbulence zone in the downstream direction whereas the first term is responsible for diffusing the gradients in Θ (Hinze, reference 9). If transport were caused solely by the bulk convective motion, the value of Θ would be expected to be uniform over regions comparable in size to the large scale structure (i.e. the width of the shear layer) with a sharp gradient in Θ at the edges of the region. Conversely, the presence of only the gradient-type diffusion would produce a gradual decrease of Θ from the center of the turbulence region toward its outer boundary.

In the absence of a significant force term, $\bar{F}$, and a molecular transport coefficient small compared to the turbulence terms, the dominant transport mechanisms reduce to (1) convection by the mean velocity (2) convection by large-scale turbulent motions and (3) gradient-type turbulent diffusion by small-scale turbulent motions. This simplified view provides a framework to discuss mixer nozzle mixing mechanisms. In the present mixer study, all three mechanisms appear to be operative with a dominant role being played by large-scale secondary flows (mechanism 1).

RESULTS AND DISCUSSION

Data Presentation

All velocity, temperature and pressure data obtained in this study are presented in both a tabular format in Tables I-V and in a graphical and/or contour plot format in figures 7 to 35. Tables I and II present LDV velocity data as a function of radial position, r, as well as non-dimensional radius, R, which is defined in the list of symbols. Table entries include axial, radial and azimuthal mean velocity components (U_x, U_r and U_ϕ). The sign convention for U_r is positive outward from the axis and that for U_ϕ is positive, counterclockwise, as viewed from downstream of the nozzle. Table entries also include axial, radial and azimuthal turbulence components (u_x, u_r and u_ϕ) as well as axial-azimuthal and axial-radial turbulence correlations ($\overline{u_x u_\phi}$ and $\overline{u_x u_r}$). Calculated standard deviations for axial mean and axial turbulence components (σ_{U_x} and σ_{u_x}) at each measurement position are also tabulated.

Tables III and IV provide total pressure, P_T, and total temperature, T_T, distribution data, respectively, referenced to primary stream stagnation conditions (P_{op} and T_{op}) as measured by the probes used to set operating conditions. Appendix A gives the relation between P_{op} and average upstream stagnation pressure. Table V provides nozzle wall static pressure, P_s, as well as wall boundary layer data.

General Observations

At inlet measurement station 1, the axial velocity field was characterized by a high velocity primary lobe region and a low velocity secondary lobe region, as would be expected. Axial velocity data at intermediate station 2 indicated that a large scale secondary flow circulation had transported low axial momentum secondary stream fluid into the inner portion of the primary lobe region and high momentum primary flow radially outward. By plume-plane station 3, azimuthal variations in axial velocity had been reduced to negligible proportions.

Radial velocity measurements at inlet station 1 showed strong inward velocities within the secondary stream and smaller, but significant, outward velocities in the primary stream. The magnitudes of these velocities scaled with the lobe penetration angles, as expected. The combined radial and azimuthal secondary flow components at inlet station 1 suggested the presence of a circulatory flow of the scale and direction inferred from the axial velocity measurements at intermediate station 2, as discussed above.

Hot flow temperature data provided further confirmation of the existence of a large scale lobe secondary flow pattern. While inlet station 1 measurements showed a clear division between hot and cold regions at the lobe interface which divided the primary and secondary streams, it could be inferred from intermediate station 2 measurements that cold fluid, originating in the upstream secondary stream lobe, was transported azimuthally into the primary lobe region. Conversely, hot fluid, originating in the upstream primary lobe, was transported outward into the secondary stream region. The scale and direction of the circulatory flow causing this transport of heat was in agreement with those inferred from mean velocity measurements.

In addition to this large scale secondary flow pattern, a system of smaller scale vortices was detected at inlet station 1 with a vorticity meter. An on-axis vortex was also detected downstream of the nozzle plug. The following sections provide a detailed discussion of the results of the experiment.

Nozzle Mean Velocity Field

Axial Velocities, Inlet Station 1 - At this station, located less than one-half of a primary lobe width downstream of the mixer lobes, the velocity field is characterized by high and low velocity regions separated by the lobe interface, as would be anticipated. This is shown in figure 7 for both hot and cold test conditions*. Within the majority of lobe region the velocity field is relatively uniform; velocities decrease in the tailpipe wall boundary layer at large radius. Within the inner half of the primary lobe region, the velocity field is also relatively uniform. A significantly lower velocity is observed, however, at larger radius ($R = 0.78$, $\phi = 3.75$). This is believed due to a clockwise circulating vortex located in the peak region of the primary lobe that transported secondary stream fluid into the primary lobe. The probable origin of such a vortex is a horseshoe vortex formation process as discussed in the section entitled "Origin of Observed Small-Scale Lobe Vortices".

Axial Velocities, Intermediate Station 2 - At this next downstream measuring station located approximately seven primary lobe widths downstream of the mixer, the two predominant features are: (1) strong penetration of low axial velocity secondary stream fluid into the middle of the primary lobe region, and (2) an

---

* In figure 7, axial velocities have been normalized by cold and hot flow reference velocities, U_{REF}, selected from the $\phi = 0$ data at $R = 0.3$. The primary-to-secondary stream velocity ratio is higher for hot flow than cold flow by a factor of approximately 1.6 (square-root of the hot flow temperature ratio), as would be expected from the Munk and Prim theorem. The projection of the lobe on the measurement plane shown in figure 7 is based on the laser intersection points given in figure 3.

outward displacement of high axial velocity primary stream fluid. Such azimuthal and radial transport of momentum is indicative of the existence of a large scale, secondary flow field. These two features of the station 2 measurements are shown in figure 8 for both hot and cold test conditions*.

From the contour plot, the scale of the secondary flow circulation appears to be on the order of the lobe dimensions. This circulation, of counterclockwise orientation, divides the primary lobe region into two high axial velocity regions, the highest velocity region at large radius and a somewhat lower one near the nozzle axis. It also appears to be responsible for the upward transport of primary stream fluid into the secondary lobe region observed for $R > 0.55$ although the horseshoe vortex, discussed above, could also contribute to the observed contour pattern. In summary, the interface between high and low velocity regions, which followed the lobe trace at station 1, has been significantly contorted by station 2; this suggests a two-stream mixing process dominated by large scale radial-azimuthal convection rather than turbulent diffusion at the interface between the two streams.

Axial Velocities, Plume-Plane Station 3 - At this station located approximately sixteen primary lobe widths downstream of the mixer, the axial velocity field has totally mixed-out in the azimuthal direction. This is shown in figure 9 for both hot and cold flow test conditions. The maximum azimuthal variation in axial velocity is listed for each radial position above the contour plots; the average azimuthal variations for hot and cold test conditions are 1.1% and 0.9%, respectively. Relative to the radial direction, the cold flow axial velocity increases monotonically with radius as it would in the case of a single-stream, convergent nozzle. Although, hot flow axial velocity displays a minimum at about $R = 0.4$, in apparent disagreement with the cold flow results, this can be shown to be associated with the temperature field. As discussed more fully below in the section entitled "Axial Mach Number Distributions", high temperatures in the vicinity of the nozzle axis reduced the fluid density which resulted in a higher acceleration of on-axis fluid for the hot flow case.

Axial Mach Number Distributions - If the assumptions of the Munk and Prim theorem previously discussed in the section entitled "Theoretical Considerations" were valid throughout thenozzle, then cold and hot flow axial Mach number distributions would be identical. The steady flow and ideal gas

---

*In figure 8 and subsequent station 2 and 3 contour plots, the lobe trace was plotted with the same R, ϕ coordinates as that shown for station 1 in figure 7. Because of geometry changes among stations, the shape of the trace varies from station to station.

assumptions of this theorem would be expected to apply to this experiment; the adiabatic and inviscid flow assumptions of the theorem (which result in constant entropy along streamlines) would be expected to be reasonably accurate at inlet station 1 and progressively less valid at stations 2 and 3.

Axial Mach number data at inlet station 1 appear to be in agreement with the Munk and Prim theorem. Shown in figure 10, parts (a)-(e), are hot and cold flow axial Mach number distributions plotted versus R for all five azimuthal positions. All hot and cold flow data points fall within the measurement uncertainty bands (see Appendix D) which are also shown in the figure. Although not anticipated, the hot and cold axial Mach number distributions further downstream at stations 2, 3 and 4 are also found to be substantially similar at all azimuthal positions. This is shown in figure 11 for station 2 and figure 12, parts (a)-(d) for stations 3 and 4. The great majority of hot and cold flow data points fall within the uncertainty bounds derived in Appendix D. The Munk and Prim theorem, therefore, suggests a useful method to compare hot and cold flow data.

The following two features of these axial Mach number distributions were also apparent in the previous discussion of axial velocity countour plots. At inlet station 1, large gradients occur in the vicinity of lobe boundaries (figure 10). At station 2 there is significant penetration of secondary stream fluid into the primary lobe region and radially outward displacement of primary stream fluid. This is evident in figure 11, parts (a) and (b).

Not previously discussed were nozzle exit plane data obtained at station 4. Mach number data at this station show a cold flow Mach 1 data point at $R = 0.98$ in figure 12, part (a). A choked condition was indicated by LDV measurements taken at various pressure ratios as discussed in Appendix A.

At plume-plane station 3, the underexpanded jet accelerates to a Mach number of about 1.2 at large radius as shown by figure 12, parts (b) to (d). Within experimental uncertainty, the hot flow axial Mach number is observed to increase monotonically with radius in agreement with cold flow results. This demonstrates that the apparent hot flow velocity defect at $R = 0.4$, previously noted in station 3 axial velocity data, is due to temperature. That is, the Munk and Prim theorem predicts identical nozzle static pressure distributions for both hot and cold flow. The higher temperatures measured near the axis in

hot flow (shown subsequently) reduced density in this region; under the influence of the same favorable axial pressure gradient, this relatively lighter fluid in the on-axis region will be accelerated more strongly resulting in a higher velocity on-axis than in the cooler region at larger radius. The theorem predicts, however, that Mach numbers will be similar for hot and cold flow as is observed to be the case.

In summary, reasonable agreement between hot and cold flow axial velocity distributions is achieved throughout the nozzle when velocity data are compared on a Mach number basis. Theoretical considerations show that exact agreement could be expected only in the case of inviscid and adiabatic flow in which case the flow would also be isentropic.

Radial and Azimuthal Velocities, Inlet Station 1 - At this station the predominant features of the radial-azimuthal velocity field (secondary flowfields) are: (1) a strong radial velocity field directed inward toward the hub in the secondary lobe region, (2) a weaker radial velocity field directed outward toward the tailpipe wall in the primary lobe region, and (3) azimuthal velocity components in the lobe interface region suggesting (1) and (2) are linked by a large-scale, counterclockwise circulation of the type inferred previously from axial velocity measurements. This inlet station secondary flowfield is shown for hot and cold flow test conditions in figure 13, parts (a) and (b), respectively*.

*Figure 13 shows error bounds for secondary flow vectors in various regions of the lobe segment, as circles. The radii of each circle gives the probable error (uncertainty) for these regions based on uncertainty estimates derived in Appendix D. The general consistency of results suggests that these calculated bounds are larger than the average uncertainties realized in the experiment.

Hot and cold flow results are observed to be generally consistent and satisfy symmetry arguments within experimental error bounds*. Except for inwardly directed vectors at R = 0.78, ϕ = 3.75 deg in hot and cold flow, a general counterclockwise secondary flowfield is indicated. This exception is believed caused by a clockwise oriented horseshoe vortex, the position of which is shown approximately by the circled HV symbol. The presence of this vortex was previously suggested by axial velocity data and directly confirmed by a vorticity meter survey discussed subsequently.

Also of interest is the relationship between the measured radial velocity magnitude and the lobe geometry (lobe penetration angle). In the absence of detached flow within the lobe, the magnitude of the radial velocity component would be expected to be proportional to the slope of the lobe. For the secondary stream lobe this is found to be approximately correct since the average value of the ratio of radial-to-axial velocity along the center of the secondary lobe (ϕ = 15 deg) for both hot and cold flow is about 0.37. This is close to the tangent of the 22 deg lobe penetration angle which is 0.4. This is also shown in terms of radial-azimuthal flow angle in figure 14, part (b), where the measured flow angles for both hot and cold test conditions are reasonably close to the 22 deg penetration angle in the inner radial region. Similarly, the ratio of primary lobe radial-to-axial velocity along the center of the primary lobe (ϕ = 0 deg) for both hot and cold flow is close to the slope of the primary lobe at the trailing edge (outward projection at 5 deg). This is shown in terms of flow angle in figure 14, part (a); at large radius the flow angle approaches 5 deg. The only exception to this trend is the inward vector at R = 0.78, ϕ = 3.75 deg which is believed associated with a horseshoe vortex as discussed above.

These oppositely directed radial velocities in the primary and secondary streams mean that the dividing surface between the two streams at the lobe exit plane constitutes a rotational flow region possessing axial vorticity of counter clockwise orientation. This can be viewed as a vortex layer (or vortex sheet when the limit of zero thickness is taken). Vorticity components also exist in the R,ϕ plane, tangent to the lobe trace, due to the discontinuity in axial velocity at the lobe trailing edge. The shear layer emanating from the lobe trailing edge, therefore, constitutes a complicated rotational flow region possessing vorticity components in all three coordinate directions.

---

*Azimuthal velocity components are observed along the ϕ = 0 traverse line which violate symmetry arguments assuming axial inflow to the primary lobe (no residual swirl from the upstream swirl vanes and simulated turbine exit guide vane assembly). The magnitudes of these cross-flow components, however, are generally smaller than the probable error bound shown in the figure for ϕ = 0 and the vectors appear to be randomly oriented. These apparent symmetry violations are, therefore, not considered significant.

In summary, radial and azimuthal velocity component measurements obtained at station 1 confirm the existence of a large scale counterclockwise lobe circulation previously inferred from axial velocity measurements at station 2.

Radial and Azimuthal Velocities, Station 2 - The secondary flow circulation pattern observed at inlet station 1 also exists at station 2 as shown in figure 13, parts (c) and (d) for hot and cold flow test conditions, respectively. Both hot and cold flow data indicate that a radially inward flow occurs in the center of the secondary lobe (ϕ = 15 deg) and radially inward and downward flow exists at ϕ = 7.5 deg*. At ϕ = 0 deg, hot and cold flow data both show outwardly directly radial components while the azimuthal components tend to be of opposite sign and violate symmetry arguments. This is indicative of measurement error. Since secondary flow vector magnitudes are less at station 2 than station 1 and uncertainty bounds are higher (Appendix D), greater scatter in defining the large-scale circulation field occurs at station 2.

In addition to this flow pattern, a relatively intense clockwise vortex is also indicated near the nozzle axis, presumably associated with residual swirl produced by the vanes upstream of the mixer. While the primary mixer lobes would be expected to attenuate residual swirl at moderate-to-large radius due to their axial orientation, the gap between the hub and the trough of the secondary stream lobe provides an unobstructed passage for convection of swirl downstream into the on-axis region at station 2.

Radial and Azimuthal Velocities, Station 3 - At station 3, the secondary flowfield is, in the main, radially inward, in response to the nozzle convergence. As shown in figure 13, parts (e) and (f), the circulatory flow observed at stations 1 and 2 is not evident in either hot or cold flow data. Some effect of this circulation may be present in that inward velocities along ϕ = 0 are lower than along the other two lines and vectors along ϕ = 7.5 deg tend to have downward azimuthal components. Near the axis (R < 0.3), a clockwise oriented vortex is evident as was the case at station 2. The presence of this vortex was confirmed by a vorticity meter survey, as discussed subsequently.

When radial-axial flow angles at large radius are calculated from the station 3 data, they are found to be substantially less than the nozzle metal angle of 14.9 deg as shown by the flagged symbols in figure 14, part (c). That this is due to radial expansion of the underexpanded jet downstream of the nozzle exit is demonstrated by the further upstream exit plane station 4

*Two vectors at ϕ = 7.5 between R = .4 and .6 are known to be biased in the radially inward direction as discussed in the section entitled "Radial and Axial Mach Number Distributions".

data (shown in the figure as unflagged symbols) where extrapolation of data to R = 1 would yield a value close to the nozzle metal angle.

Radial and Axial Mach Number Distributions - As in the case of the axial Mach number distributions discussed previously, hot and cold flow, radial and axial Mach number distributions are very similar. This is shown in figures 15-19. One region of disagreement is shown in figure 15, part (c), where four hot flow radial Mach number data points located between R = 0.45 and 0.6 differ substantially from cold data. These hot flow points are known to be in error since comparison of total pressure and axial velocity data in this region, as well as redundant axial velocity data, showed the LDV measuring volume was offset in azimuth for these radial velocity measurements. For code assessment purposes it is recommended that hot flow radial velocity data in this region be neglected and cold flow Mach number data be used to estimate hot flow velocities. Other examples of disagreement between hot and cold flow data are evident in the figures, however, the level of disagreement tends to be comparable to the indicated uncertainty bounds.

These data, as well as the axial Mach number results presented earlier, suggest that cold flow tests can be employed to obtain a reasonable estimate of the three-dimensional Mach number field that would exist in more complicated hot flow tests.

Nozzle Total Temperature Field

Inlet Station 1 Contours - At this station the temperature field, as expected, consists of a hot primary region and cold secondary region with the intervening temperature gradient region roughly centered on the lobe projection. This is shown in figure 20 where part (a) displays T_T/T_{op}* contours and part (b) shows the relationship of the contours to the lobe projection. In apparent confirmation of velocity data, an upward penetration of hot fluid into the secondary stream near R = 0.65 and downward penetration of cooler fluid into the primary stream at somewhat larger R indicates the presence of a small, clockwise-oriented vortex (horseshoe vortex) in the primary lobe. The presence of cold fluid within the primary lobe near the trough of the

*T_{op} is total temperature in the primary stream, the reference value for which is 755°K.

secondary stream lobe is the result of inward convection of secondary stream fluid by the strong radial velocity field during the time between leaving the lobe and arriving at station 1. This is based on a calculation using measured axial and radial velocities which predicts an inward penetration of the 0.48 contour much as shown.

Intermediate Station 2 Contours - Temperature contours at this station unequivocably confirm the existence of the large scale circulation inferred previously from velocity data. In figure 21, cool fluid is seen to have penetrated the primary lobe region, extending all the way to the lobe centerline (ϕ = 0 deg) between R = 0.3 and 0.5. Consistent with a large scale circulation of counterclockwise orientation, there is a corresponding transport of hot primary stream fluid outward and upward into the otherwise cool secondary stream region.

The only station 2 region that is mixed-out azimuthally is a hot flow area near the axis where the previously discussed on-axis vortex as well as the close proximity of the segment boundaries (small lobe width) favor mixing.

Plume-Plane Station 3 Contours - At the nozzle exit the temperature field is reasonably well mixed-out in the azimuthal direction as shown in figure 22. There is some radial stratification; the largest radial temperature gradients occur in the vicinity of the axis, where, as in the case of station 2, a relatively hot spot exists. A comparison of station 2 and 3 contours (figures 21 and 22) for the outer portion of the segment (R > 0.4) suggests that the large-scale, counterclockwise circulation that existed between stations 1 and 2 also plays an important role in the mixing occurring downstream of station 2. While the coolest region of station 2 is in the upper right corner of the contour, the coolest region at station 3 is to the left and downward; similarly the hot region at station 2, contained within the 0.79 contour, by station 3, has been displaced upward and to the right. Temperature data, therefore, provide an indication of the continued importance of secondary flow-induced convective mixing downstream of station 2; this could also be inferred, but less clearly, from axial velocity data.

Total Temperature Distributions - An alternative view of temperature results is given by radial distribution plots in figures 23-25. At station 1, figure 23 shows that the temperature distributions within the primary and secondary streams are spatially uniform (to within about 1%). From part (a), the width of the thermal gradient (shear layer) region occurring along ϕ = 0 deg near R = 0.8 is on the order of 0.1R. The gradient region is broader at ϕ = 7.5 deg since the shear layer is intersected at a shallow angle.

The significant penetration of cool secondary stream fluid into the primary lobe region at station 2 is apparent in figure 24 as is the outward convection of hot primary stream fluid to large radius. The hottest region is

near the axis. At station 3, the hottest region is again found near the axis as shown in figure 25, part (a). At this station, however, the temperature field is well mixed-out in the azimuthal direction. Figure 25, part (b) confirms the expected result that the radial distribution does not change appreciably between the nozzle exit station 4 and the plume-plane station 3.

Nozzle Total Pressure Field

Hot and cold flow total pressure distributions are found to be similar at the three axial measurement stations as shown in figures 26-28. The origin of the total pressure defect in figure 26, part (c) near R = 0.2 for cold flow is unknown; it could be the result of encountering the low momentum core of a secondary lobe horseshoe vortex which has been convected into the primary lobe region by the circulations discussed previously. No total pressure defect regions are observed at large radius although preliminary data acquired at ϕ = 0 showed such a defect; this could have been the result of a misalignment error that caused the probe traverse line to pass through the core region of the primary lobe horseshoe vortex. These vortices, rather than flow detachment within the lobes, are believed to be the source of the total pressure defect shown in figure 26 and that encountered during preliminary testing; flow visualization results, discussed subsequently, further suggest that flow detachment does not occur within the lobes.

At the interface between primary and secondary streams, the total pressure along traverse line ϕ = 0 deg at station 1 changes from a value characteristic of one stream to a value characteristic of the other in a distance that is on the order of 0.1R (0.6 cm). A similar distance was indicated by temperature data discussed previously. This then is an approximate measure of the sum of the boundary layer thicknesses existing on each surface of the mixer lobe at the lobe trailing edge.

At station 2, a region of total pressure defect is observed to encircle the nozzle axis (figure 27). The radius of this region is approximately one centimeter, which is comparable to the plug trailing edge radius. This defect, therefore, probably arises from separation of the plug boundary layer at the base of the plug. For both measurement lines ϕ = 0 and 7.5 deg, there is a region of somewhat lower total pressure near mid-radius. This is a further indication of the azimuthal transport of lower momentum secondary stream fluid into the primary lobe region by the circulatory flow patterns suggested by velocity and temperature measurements.

At station 3, the on-axis total pressure defect region is reduced in area as would be expected due to nozzle convergence. The mid-radius total pressure

defect region observed at station 2 is still somewhat apparent at station 3 along measurement lines ϕ = 0 and 7.5 deg although the magnitude of the defect is smaller at station 3. As in the case of velocity and temperature measurements, the total pressure distribution is well mixed-out in the azimuthal direction with greater variations evident in the radial direction.

Static Pressures and Wall Boundary Layer Data

Table V lists static pressures measured at the tailpipe wall at stations 1 and 2 as well as an on-axis measurement at station 2. Measurements of on-axis static pressure at station 3 are discussed in Appendix E. The wall and on-axis values at station 2 are similar, suggesting a radially uniform static pressure distribution at this location. This would be anticipated since the mixing duct is only weakly convergent in this region and streamline curvature is small. Table V also shows that hot and cold flow wall static pressures are identical at station 1 and substantially similar at station 2 (within uncertainty bounds). Equality of hot and cold static pressure fields is predicted by an isentropic flow assumption as discussed in the section entitled "Theoretical Considerations".

Table V also displays the results of a total pressure traverse of the tailpipe surface boundary layer at station 2. The thickness of this layer appears to be approximately 1.5 cm. Total pressure data listed in Table III permit estimates to be made of plug and tailpipe surface boundary layer thicknesses at station 1.

Flow Visualization

Surface flow visualization within the mixer lobes was performed to determine whether the lobe boundary layers separated under the influence of possible adverse pressure gradients associated with turning. A suspension of lampblack in a mixture of mineral oil and kerosene was applied to the lobes as a series of dots, the rig was brought up to operating condition and then shut down. From the surface patterns, there was no indication of a separation line within either the primary or secondary lobes. This confirms total pressure results from which it was also concluded that flow detachment does not occur in the lobe region.

When this flow visualization technique was applied to the plug, there was an indication of a clockwise circulation as viewed from the nozzle exit. This confirmed a similar conclusion derived from LDV measurements of the secondary flow field. To further investigate the possible circulatory flow at the plug surface, a tuft on a probe was used to survey the nozzle internal flowfield. By necessity, the rig was operated at a low subsonic exit Mach number of

approximately 0.15. On the nozzle axis downstream of the plug, the tuft was observed to spin-up, generating a cone in space in a manner similar to that which occurs when a tuft is placed within the core of an airfoil tip vortex. Although the direction of spin could not be determined, this clearly indicated the presence of axial vorticity concentrated within an on-axis vortex.

In addition to this vortex, a pair of vortices having opposite rotation was observed just downstream of the tip region of the primary lobe. The direction of rotation was evident, in the case of these vortices; as the probe entered the vortex core, the initial spin-up of the tuft occurred and the direction of rotation could be ascertained. The occurrence of this vortical flowfield, apparently convected downstream from within the primary lobe interior, was unanticipated.

Vorticity Meter Measurements

To further investigate these vortical flow patterns, a paddle-wheel vorticity meter was used to survey the nozzle flowfield with the rig operating at a low exit Mach number. When aligned with the local flow direction, this meter will rotate only if there is a fluid vorticity component in the local flow direction (along the probe axis). The on-axis vortex was easily detected with the vorticity meter and was observed to have a clockwise rotation as viewed from the nozzle exit. This vortex was found to persist from 0.3 cm downstream of the plug to a distance greater than 10 cm downstream of the nozzle exit plane. The origin of this vortex is believed to be net clockwise swirl introduced by the upstream swirl vane-turbine exit guide vane assembly.

Since the nozzle cross-sectional area continuously decreases from the lobe exit plane to the nozzle exit, vortex lines associated with this swirl would be stretched in the axial direction resulting in an intensification of the vortex. It is believed that this vortex contributed to the effective azimuthal mixing in the inner radial region near the nozzle axis. Whether a vortex of this nature is desirable in full-scale mixers is uncertain since unrecoverable swirl represents a thrust loss mechanism.

The vorticity meter also confirmed the tuft survey, indicating the presence of a pair of contra-rotating vortices within the primary lobe at the tip. These vortices are shown schematically in figure 29, part (a). The vortex on the left side of the lobe rotated clockwise while that on the right side rotated counter-clockwise. The vortices appeared relatively intense, comparable in intensity to that found on-axis. A number of primary lobes were surveyed and all such lobes displayed such a pattern.

The vortices were located approximately one centimeter inboard from the tip of the lobe. They appeared to be small in spatial extent in that a movement of the vorticity meter on the order of one-sixth to one-third of a centimeter caused the meter to stop rotating. The vortices could be tracked downstream of the lobes within the nozzle.

In addition to these two vortices, a similar pair of contra-rotating vortices was detected in the trough of the secondary lobe as shown in figure 29. These were of much weaker intensity than those encountered in the primary stream. Not only was the meter rotational speed much slower but a slight offset in meter position caused the paddle to stop rotating. The directions of rotation of the vortices in the secondary lobe were opposite to those found in the primary lobe.

The meter also indicated the presence of a thin vortex layer emanating from the interface between the primary and secondary streams on the sides of the lobe. When tracked along this interface, the meter spun continuously. The origin of this vortex layer or "sheet" was clearly the radially opposite flows existing within the primary and secondary streams. On the right side of the lobe the rotation direction was clockwise and vice versa on the left. This vortex layer is represented schematically in figure 29 as a series of open circles of appropriate rotational direction.

Outside the regions cited above, the meter did not rotate. This applies to surveys conducted within the lobes, at station 1 and at other downstream nozzle positions. Within the sensitivity limits of the vorticity meter employed, therefore, these other regions did not possess axial vorticity. A stronger inference is that the flow exiting the primary and secondary lobes is irrotational except within the concentrated vortex regions discussed above and the boundary layer regions adjacent to the lobe surfaces.

Origin of Observed Small-Scale Lobe Vortices

The origin of the observed primary and secondary stream lobe vortices was concluded to be a horseshoe vortex formation mechanism associated with the interaction of upstream duct boundary layers with the lobes, for reasons discussed below. In part (b) of figure 29, the boundary layers upstream of the lobes on the dividing surface between the primary and secondary streams are shown shaded. Since the boundary layer vorticity vector orientation and direction of rotation are related by a right-hand rule, boundary layer vortex lines are directed clockwise, in the secondary stream, as shown, and counterclockwise in the primary stream. These vortex lines encounter the lobes which penetrate into the respective streams, and wrap around the lobe as is shown schematically in figure 30, part (a) for the primary lobe. This collection

of vortex lines (or vortex tube) is convected radially inward by the secondary stream mean flow and manifests itself at the lobe exit as two vortices of opposite sign, bracketing the primary lobe at the troughs of the secondary lobe.

A similar process occurs in the primary stream. The vortex tube wraps around the secondary lobe penetration into the primary stream and is convected radially outward into the tip region of the primary lobe. The directions of rotation of the four vortices contained within a lobe segment and the locations of these vortices are consistent with the postulated mechanism and the observed lobe radial velocity fields.

With this identification of the mechanism, several features of such mixer nozzle lobe vortex systems can be predicted in a qualitative manner. First, the circulation of a vortex should scale roughly with the circulation, per unit length, of the boundary layer incident upon the lobe obstruction. This circulation per unit length is equal to the mean velocity of the approaching stream as indicated in part (b) of figure 30. As observed in the present study, therefore, primary lobe vortices should be significantly stronger than secondary lobe vortices. Second, the standoff distance of the vortex (the distance between the point of boundary layer separation and the leading edge of the obstacle) should be proportional to the width of the lobe, b(x). This arises since the magnitude of the adverse pressure gradient upstream of the obstacle is proportional to the obstacle width. The above is approximate since Belik (reference 10) has shown, for circular cylinders, that the ratio of standoff distance to cylinder diameter is a monotonically increasing function of incident boundary layer Reynolds number. Standoff distance is believed to be an indicator of horseshoe vortex size.

Third, the angle of the obstruction relative to the wall boundary layer shown in figure 30 is an important parameter. If ψ is 90 deg, the classic horseshoe vortex case exists. For small ψ, separation will not occur and a concentrated horseshoe vortex will not be produced. Fillets in the corner would also tend to inhibit vortex formation. In summary, a large turning angle (ψ) would favor vortex formation with the size of the vortex increasing with lobe width and inlet boundary layer thickness. The strength of the vortex would be proportional to the approach velocity.

Origin of Other Small-Scale Lobe Vortices

In addition to the horseshoe vortex mechanism described above, a system of four concentrated vortices per lobe segment can be produced in a different manner. Tests at UTRC with a rectangular lobe configuration have shown that vortices can spin off the ninety degree corners of inwardly and outwardly projecting lobes producing a vortex system which is the opposite of that observed

with the present model. Vortices in the secondary lobe then occur near the peak of the lobe (rather than near the trough) with the clockwise vortex on the left and the counterclockwise vortex on the right (opposite to figure 29). Conversely, a pair of primary stream vortices occurs near the base of the primary lobe with the clockwise vortex on the right side and counterclockwise vortex on the left. These vortices have been observed to be intense and can be tracked downstream of the lobes for appreciable distances.

The vortices arise in a manner similar to the trailing vortices which emanate from finite span wings or a plate of finite width inclined relative to a uniform stream. The cross-sectional shape of the lobe determines the intensity of the shed vorticity and the degree to which it will be concentrated in a point vortex.

Since both the location and direction of rotation of vortices generated by this mechanism are opposite to those encountered in the present study, this vortex generation mechanism was not significant in the present study. Model mixer studies conducted elsewhere (reference 3), however, may have encountered vortices generated in this manner. In principal, the horseshoe mechanism and this vortex generating mechanism can exist simultaneously, resulting in a vortex system consisting of eight vortices per lobe segment. At this time, the role such vortex systems play in the nozzle mixing process is unclear.

Nozzle Turbulence Field

Turbulence Kinetic Energy - Turbulence level distributions at inlet station 1 are similar for hot and cold flow test conditions. This is shown in figure 31 where the ratio of $q = \sqrt{u_x^2 + u_r^2 + u_\phi^2}$ to local axial velocity, U_x, is plotted as a function of nondimensional radius. (The quantity, q, is the square-root of twice the kinetic energy of turbulence.) Solid symbols denote points where the assumption $u_r = u_\phi$ was applied to permit q to be calculated. In regions away from lobe boundaries, figure 31 shows that the turbulence level is typically in the range from five to eight percent; turbulence levels greater than fifteen percent are observed in the shear layers that exist at the interface between primary and secondary streams. These regions of maximum shear would be expected to have the highest turbulence levels.

At station 2 turbulence levels are generally in excess of ten percent; cold flow turbulence levels are consistently lower than hot flow levels (figure 32). This trend also exists at station 3 as shown in figure 33. Turbulence levels at station 3 are significantly lower than station 2. This is believed to be due in part to the significant stream contraction that occurs between stations 2 and 3. Rapid stream contraction is predicted to attenuate all three components of turbulence relative to the local axial velocity

(reference 11). The attenuation of azimuthal mean velocity gradients by mixing between stations 2 and 3 is another possible contributor to low station 3 turbulence levels; such gradients are a source of turbulence production.

The reasonable agreement between station 3 and 4 axial turbulence component data shown in figure 33, part (d), tends to confirm the consistent trend of lower cold flow turbulence levels near the nozzle exit.

Turbulence Correlation Coefficients - Measured distributions of the axial-radial and axial-azimuthal turbulence component correlations for hot flow test conditions are shown in figures 34 and 35, respectively. Interpretation of these data based on known behavior of such functions in simpler flows such as jets and wakes is difficult in the present case due to the complexity of the three-dimensional mixer nozzle flowfield. The data may be useful in a general way to assess turbulence models employed in computational procedures.

NOZZLE MIXING MECHANISMS

As discussed in the section entitled "Mixing Mechanisms in Turbulent Flow", a simplified view of the mixing in turbulent flow results in the following three transport mechanisms: (1) convection by the mean velocity field, (2) convection by large-scale turbulent motions, and (3) gradient-type turbulent diffusion by small-scale turbulent motions. Velocity, temperature and total pressure data presented in the previous section strongly indicate that the first mechanism, convection by the mean radial-azimuthal velocity field, represents the dominant mechanism for nozzle mixing. This secondary flow field is characterized by a circulatory flow in each lobe segment established by oppositely directed radial flows in the primary and secondary stream lobes as shown schematically in figure 36, part (a). At the lobe trailing edge, these radial fields produce a net circulation around the contour shown in the figure. In a simplified view of this flowfield, the interface between the two streams can be viewed as a thin vortex layer or sheet and the circulation around the contour taken as the sum of the two radial velocity components. From Kelvin's theorem, which would be expected to apply approximately to this case, this circulation persists downstream of the lobes causing radial-azimuthal mixing of the two streams throughout the axial extent of the nozzle.

This circulation can be considered a pressure driven secondary flow since the oppositely directed radial components are established by radial pressure gradients in the lobes. Azimuthal components are established near the hub and tailpipe wall by a stagnation-type flow as indicated schematically in part (c).

The extent of nozzle mixing by this circulation would appear to be dependent upon the ratio of radial to axial velocity (U_r/U_x) rather than on the absolute magnitude of the radial velocity component. The greater this ratio, the greater will be the radial and azimuthal displacement of a fluid element in the time required to transit the nozzle, and presumably the greater the convective transport (mixing). Since radial velocity magnitude would be expected to be proportional to lobe penetration angle, in the absence of separation within the lobes, penetration angle appears to be an important parameter. Effects of other parameters such as the extent of radial lobe penetration, ℓ, lobe width and the proximity of the hub and tail pipe wall to the lobe trough and peak, respectively, would also be expected to be important since these parameters affect the scale of the secondary circulation. These conclusions regarding the importance of the lobe exit plane secondary flowfield are consistent with the reference 2 study. In that study, analytical predictions employing a representation of this secondary field were found to yield much better agreement with data than those in which lobe exit secondary flows were neglected.

In this simplified description of the mixing process, convection by large-scale turbulent motions (the second mixing mechanism listed above) would be expected to be responsible for mixing at the next smallest scale. These turbulent motions, following Hinze (reference 9), are expected to cause the lateral spreading of the shear layers shed at the lobe trailing edge and which are imbedded in the larger scale circulations. These broadened shear layers are contorted by the mean velocity field in a complicated three-dimensional manner. At the smallest scale of mixing, gradient-type diffusion by small-scale turbulent motions are expected to progressively attenuate remaining gradients.

While this picture of the mixing process is very simplified, it provides some indication of why lobed mixers are efficient. The lobed geometry not only produces an azimuthally and radially varying flowfield from an initially axially symmetric field, but sets up large-scale secondary circulations to mix-out the resultant axial and radial variations. While the lobed geometry also increases the length of the shear layer interface between the two streams resulting in enhanced mixing by virtue of shear layer broadening, this study suggests that the large-scale circulations play a major role in the mixing process. The view is consistent with the reference 1 study in which it was concluded that large-scale mixing associated with secondary flow downstream of the lobe exit is an important nozzle mixing mechanism.

SUMMARY OF RESULTS

1. The three-dimensional mean and turbulent velocity field, mean total pressure field and mean total temperature field of a multi-lobed, model mixer nozzle were defined within one lobe segment at the lobe exit, the nozzle exit and at an intermediate location within the mixing duct for both hot and cold flow test conditions.

2. Axial, radial and azimuthal Mach number distributions throughout the nozzle as well as total pressure distributions were found to be in close agreement, (generally within experimental uncertainty bounds) for both hot and cold flow test conditions.

3. Strong azimuthal and radial gradients in mean flow properties present at the lobe exit were partially attenuated at the intermediate measurement position; at the nozzle exit, distributions were relatively uniform in the azimuthal direction and less uniform in the radial direction.

4. Large, inward directed radial velocities were observed in the secondary stream at the lobe exit and smaller, but significant, outward directed radial velocities observed in the primary stream. These radial velocities, in conjunction with azimuthal velocities measured at the lobe exit indicated the presence of a circulatory (secondary) flow in the radial-azimuthal plane having a scale on the order of one lobe segment.

5. Comparison of velocity, pressure and temperature measurements at the lobe exit plane and at a downstream measurement location within the tailpipe indicated an azimuthal transport of low momentum and cold secondary stream fluid into the primary lobe region and a corresponding outward and azimuthal transport of primary stream fluid into the secondary lobe region.

6. A system of smaller-scale, intense vortices was observed at the lobe exit plane; the system consisted of two pairs of contrarotating vortices within each lobe segment. A small-scale, intense vortex was also detected on-axis downstream of the plug.

7. An LDV optical arrangement and seeding system was developed which permitted accurate velocity measurements to be made in the highly accelerated transonic flow region existing near the nozzle exit.

CONCLUSIONS

1. The multi-lobed mixer employed in the present study produced a system of adjacent, contrarotating circulatory flows at the exit of the mixer lober. These secondary flows were located in the radial-azimuthal plane (axially oriented vortices) and had a scale on the order of one lobe segment.

2. The large-scale circulations discussed above provided the dominant mechanism by which transport of heat and axial momentum occurred at length scales comparable to the nozzle radius. This large scale mixing would be expected to control the rate of mixing within the nozzle. In their absence, mixing rate would be expected to be lower, being controlled by the small scale turbulent eddy interactions within the shear layers emanating from the trailing edge regions of the lobes.

3. The observed general agreement between hot and cold flow Mach number and total pressure distributions throughout the nozzle indicates that isentropic flow theory can be used to interpret some aspects of the nozzle flow. The good agreement at the exit of the lobes as well as vorticity surveys at this position indicate that the flow through the lobes is basically inviscid.

4. Production of the observed large-scale secondary flows was dependent upon the existence of radial flows of opposite direction in the primary and secondary lobes which were in turn established by radial pressure gradients within the lobes. This secondary flow consists of a large scale irrotational flow region within which are embedded smaller rotational regions containing axial vorticity shed at the lobe trailing edge.

5. The origins of smaller-scale, more intense vortices observed in the primary and secondary lobe exit flows were the primary and secondary stream boundary layers incident upon the mixer lobes. These produced axially-aligned vortices by a horseshoe vortex formation mechanism similar to that which occurs at the intersection of a bluff-body and a wall boundary layer.

6. The importance of these horseshoe vortices relative to the nozzle mixing process is unclear at this time although they would be expected to affect mixing at a scale comparable to the lobe half-width. This is approximately one order of magnitude smaller than the scale of the vortices discussed above.

7. A second system of small-scale, intense vortices, observed in tests with a different lobe geometry, were formed by a vortex formation process similar to that which occurs at the tip of a lifting, finite span wing or an ellipsoid at angle of attack.

8. Depending upon the lobe geometry of a given mixer, both, one, or neither of the small-scale vortex systems described above may exist at the lobe exit plane.

9. Mixer designs which induce no net circulation but generate secondary flows having a scale on the order of the annular gap between the plug and tailpipe wall would be expected to be more effective than mixers having small secondary flow patterns or none. For a multi-lobed mixer, lobe penetration angle and depth would be expected to be the parameters that most affect secondary flow velocity and scale, respectively.

REFERENCES

1. Povinelli, L. A., Anderson, B. H. and Gerstenmaier, W.: Computation of Three-Dimensional Flow in Turbofan Mixers and Comparison with Experimental Data. AIAA Paper 80-0227, 1980.

2. Anderson, B., Povinelli, L. and Gerstenmaier, W.: Influence of Pressure Driven Secondary Flows on the Behavior of Turbofan Forced Mixers. AIAA Paper 80-1198, 1980.

3. Anderson, B. H. and Povinelli, L. A.: Factors Which Influence the Behavior of Turbofan Forced Mixer Nozzles. NASA TM 81668, 1981.

4. Shumpert, P. K.: An Experimental Model Investigation of Turbofan Engine Internal Exhaust Gas Mixer Configurations. AIAA Paper 80-0228, 1980.

5. Kozlowski, H. and Kraft, G.: Experimental Evaluation of Exhaust Mixers for an Energy Efficient Engine. AIAA Paper 80-1088, 1980.

6. Kuchar, A. P. and Chamberlin, R.: Scale Model Performance Test Investigation of Exhaust System Mixers for an Energy Efficient Engine Propulsion System. AIAA Paper 80-0229, 1980.

7. Paynter, G. C., Birch, S. C., Spalding, D. B. and Tatchell, D. G.: An Experimental and Numerical Study of the 3-D Mixing Flows of a Turbofan Engine Exhaust System. AIAA Paper 77-204, 1977.

8. Tsien, H. S.: The Equations of Gas Dynamics. Section A in Fundamentals of Gas Dynamics. H. W. Emmons, Ed., Princeton University Press, 1958.

9. Hinze, J. O.: Turbulence. McGraw-Hill, 1959.

10. Belik, L.: The Secondary Flow about Circular Cylinders Mounted Normal to a Flat Plate. Aero. Quarterly, February 1973, pp. 47-54.

11. Bradshaw, P. and Pankhurst, R. C.: The Design of Low-Speed Wind Tunnels. Chapter 1 in Progress in Aeronautical Sciences, Vol. 5, D. Kuchemann and L. H. G. Sterne, Eds., MacMillan, New York, 1964.

12. Bryer, D. W. and Pankhurst, R. C.: Pressure-Probe Methods for Determining Wind Speed and Flow Direction. National Physical Laboratory. H. M. Stationary Office, London, 1971.

13. Dean, R. C., Jr.: Aerodynamic Measurements. Gas Turbine Laboratory, M.I.T., 1953.

14. Liepmann, H. W. and Roshko, A.: Elements of Gas Dynamics, John Wiley, New York, 1957.

15. Ladenburg, R. W., Ed.: Physical Measurements in Gas Dynamics and Combustion, Part 1, Volume IX, High Speed Aerodynamics and Jet Propulsion. Princeton University Press, Princeton, N. J., 1954.

16. Doeblin, E. O.: Measurement Systems: Application and Design. McGraw-Hill, New York, 1966.

17. Schenck, H., Jr.: Theories of Engineering Experimentation. McGraw-Hill, New York, 1961.

18. Burington, R. S. and May, D. C.: Handbook of Probability and Statistics. McGraw-Hill, New York, 1970.

19. Patrick, W. P. and Paterson, R. W.: Seeding Technique for Laser Doppler Velocimetry Measurements in Strongly Accelerated Nozzle Flowfields. AIAA Paper 81-1198, 1981.

APPENDIX A

EXPERIMENTAL PROCEDURE

Method of Setting Operating Conditions

The nominal operating conditions selected for this experiment were a primary stream pressure ratio of approximately 2.6, a primary-to-secondary pressure ratio of 1.04, a primary-to-secondary total temperature ratio of 2.5 for hot flow testing and a temperature ratio of 1.0 for cold flow testing. Two variables which affected operating conditions were the air supply temperature to the rig and ambient pressure in the test cell.

The air supply total temperature, which was a function of the temperature of outdoor storage tanks and the operating schedule of the supply air compressors, varied from 280°K to 305°K during the cold flow test program. Most measurements were acquired near 295°K. During cold flow testing, the primary and secondary stream total temperatures were typically within 1°K of the air supply temperature. For hot flow testing the secondary stream total temperature was continuously monitored and the primary stream total temperature adjusted to provide a nominal 2.5 temperature ratio. During the hot flow test program, secondary stream temperature varied from 295°K to 315°K requiring a corresponding primary total temperature near 750°K. During data acqusition, the primary stream temperature was held within 6°K of the nominal set point. This set tolerance correponds to a primary-to-secondary total temperature ratio range of 2.500 ± 0.02. LDV velocity data given in this report have been corrected to account for a variable air supply temperature as discussed in this appendix.

Secondary stream total temperature was measured upstream of the model at a secondary stream temperature rake for both hot and cold flow tests. For cold flow, primary stream total temperature was measured at the primary stream temperature rake; for hot flow, primary stream total temperature was measured by a probe located within one of the primary mixer lobes. A second total temperature probe was installed in an adjacent primary lobe to provide a redundant measurement of the set point.

Primary and secondary stream total pressure probes used to control nozzle operating conditions were set at gauge pressures of 1.61×10^5 N/m^2 (23.4 psig) and 1.50×10^5 N/m^2 (21.8 psig), respectively. Average inlet total pressures differed slightly from these values as discussed in the following section. These pressures were maintained throughout the test program, independent of small changes in ambient pressure, since the Mach number distribution within a choked nozzle is not dependent upon nozzle pressure ratio, being set only by the nozzle area distribution. The velocity distribution within the choked nozzle then depends only on the nozzle inlet total temperature. To demonstrate

that the nozzle was choked, inlet total pressures were varied about the operating point while velocity at a point in the nozzle was monitored with the LDV system. Independence of velocity and inlet total pressure demonstrated a choked condition.

The test cell ambient pressure P_a, was given by

$$P_a = P_A - \Delta P \tag{A1}$$

where P_A is atmospheric pressure and ΔP is the pressure differential between atmospheric and test cell pressure. During the test program, P_A varied from 1.000×10^5 to 1.026×10^5 N/m^2. The cell differential pressure, ΔP, which was set by a valve in the cell exhaust stack was zero for cold flow and 990N/m^2 for hot flow testing. The maximum variation in ambient pressure P_a, during the cold flow testing was 1.005×10^5 to 1.020×10^5 N/m^2 and 9.878×10^4 to 1.010×10^5 N/m^2 during hot flow. The maximum primary stream pressure ratio variation due to ambient pressure changes was therefore 0.77 percent for cold flow and 1.1 percent for hot flow.

Two other sources of pressure ratio variation were the accuracy of the pressure transducers used to set primary pressure and the tolerance achieved in holding the pressure at the desired value. The transducers were calibrated at 137.9×10^5 N/m^2 and zero gauge pressure periodically using a primary pressure standard with an accuracy of 0.025 percent of reading. The small difference between the calibration and operating pressure effectively eliminated nonlinearity and hysteresis errors, hence, transducer errors can be neglected. The primary stream automatic pressure controller was observed to hold the nominal pressure setting of 1.61×10^5 N/m^2 within 350 N/m^2 although periodic adjustments were required to maintain this tolerance when large air supply pressure variations associated with the compressor operating schedule occurred. This tolerance corresponds to a variation of 0.12 percent about the nominal pressure ratio.

The same transducer accuracy and set tolerance apply to the secondary stream total pressure. The probable error in setting the nominal secondary-to-primary pressure ratio is given by

$$\frac{E_{PR}}{(P_{op}/P_{os})} = \sqrt{\left(\frac{\Delta P_{op}}{P_{op}}\right)^2 + \left(\frac{\Delta P_{os}}{P_{os}}\right)^2} \tag{A2}$$

The calculated percentage probable error in pressure ratio obtained by taking $\Delta P_{o_p} = \Delta P_{o_s} = 350$ N/m^2 was 0.2 percent.

Reference Conditions

Nozzle inlet total pressures and temperatures were set throughout the cold and hot flow test program using a single set of probes (and checked by a second set) as discussed in the preceding section. During the cold flow test program, the total pressure distribution upstream of the nozzle was defined by four rakes in the secondary stream and three rakes in the primary stream. Figure 2 shows the axial location of the rakes, which were spaced at equal intervals in azimuth. The secondary and primary stream rakes consisted of twelve and ten probes, respectively, spaced at equal radial intervals across each stream.

In terms of azimuthal symmetry, the average total pressure of the four secondary rakes differed from the mean by 0.07 percent, 0.43 percent, 0.31 percent, and 0.06 percent, respectively. Similar data for the primary stream were 0.07 percent, 0.08 percent, and 0.14 percent. Typical rake radial pressure distributions for the two streams are given below:

Ratio of Rake Local to Radially Averaged Total Pressure
(location numbers increase from inner-to-outer wall)

LOCATION	PRIMARY	SECONDARY
1	0.954	0.984
2	1.008	1.005
3	1.009	1.004
4	1.010	0.999
5	1.013	1.004
6	1.011	1.004
7	1.009	1.003
8	0.988	1.003
9	0.997	1.001
10	1.002	1.000
11	---	0.998
12	---	0.994

The above results indicate that the total pressure distribution upstream of the nozzle was reasonably uniform in both the radial and azimuthal directions. The ratios of the average of the rake total pressures in the primary and secondary stream to the total pressures of the primary and secondary probes used to set operating conditions were 0.9966 and 0.9951, respectively. Designating P_P and P_S as primary and secondary average inlet total pressures and P_{op} and P_{os} as the total pressures of the primary and secondary probes used to set operating conditions:

$$P_P = 0.9966\ P_{op};$$

$$P_S = 0.9951\ P_{os}; \qquad \text{(A3)}$$

These ratios should be applied to convert pressure ratios tabulated in Table III (which are presented in terms of total pressure relative to the probe used to set operating conditions) to pressures referred to average inlet conditions.

The primary stream total pressure rakes failed at the outset of hot flow testing. Since secondary stream inlet total pressure distributions should not have been altered by primary stream heating in hot flow and primary stream total pressure distributions downstream of the primary lobe (for example, azimuthal position ϕ = 0 deg in Table III) were similar in the mid-lobe region for both hot and cold flow, it is reasonable to apply equation (A3) to both hot and cold test conditions.

Table A1 given below summarizes mixer nozzle operating parameters at reference conditions. For the purpose of calculating nozzle pressure ratios, a standard atmospheric pressure of 1.013×10^5 N/m^2 has been assumed.

TABLE A1

NOZZLE OPERATING PARAMETERS AT REFERENCE CONDITIONS[a]

FLOW CONDITION	P_{op}, N/m^2	P_{os}, N/m^2	P_P, N/m^2	P_S, N/m^2	
COLD	2.623×10^5	2.513×10^5	2.605×10^5	2.501×10^5	
HOT	2.623×10^5	2.513×10^5	2.605×10^5	2.501×10^5	
FLOW CONDITION	P_a, N/m^2	P_P/P_a	P_p/P_s	T_{op}, °K	T_{os}, °K
COLD	1.013×10^5	2.572	1.042	288.8	288.8
HOT	1.003×10^5	2.597	1.042	755.6	302.2

[a] Table gives absolute pressures; LDV data have been corrected to the reference temperatures cited above; P_a is test cell pressure.

Total Pressure Measurements

Total pressure measurement surveys at axial stations 1 and 2 were carried out with a Kiel-type stagnation-pressure probe similar to that shown in figure 5(b) of reference 12. The outer diameter of the probe's cylindrical shield was 0.159 cm. This shielded or shrouded type of probe was selected since LDV velocity measurements indicated significant radial flows at these stations and such a probe is relatively insensitive to incident flow angle. LDV data show that the largest deviation of the flow from the axial direction at stations 1 and 2 occurred at station 1, where a flow angle of 26 deg was obtained in the secondary stream. Based on references 12 and 13, the probe used in this study would be expected to produce a 1 percent error in dynamic head at a flow angle of 45 deg and negligible error at 26 deg.

The above references also note that stream turbulence can cause indicated total pressure to exceed actual. Since the error depends on the scale of turbulence as well as the turbulence intensity and probe design, a clear correction procedure is not available. An estimate of the total pressure error, E_p, however, can be obtained from

$$\frac{E_p}{\frac{1}{2}\rho V^2} = \frac{u^2+v^2+w^2}{V^2} \qquad \text{(A4)}$$

While figures 31-33 show that turbulence levels are low at station 3, values of q/U_x of 0.2 are obtained at stations 1 and 2. With this turbulence level, equation (A4) would predict a total pressure error equal to four percent of the local dynamic head. This error can, therefore, be appreciable and may need to be accounted for in interpreting the total pressure data. Since a rigorous correction procedure is not presently available, data tabulated in Table III have not been corrected for this effect.

Total pressure surveys at axial station 3 were conducted with a 0.32 cm dia modified Prandtl-type pitot-static probe with an internal bore cone angle to sharpen the leading edge. Such probes (reference 12) would be expected to measure total pressure with negligible error for flow angles less than 20 deg over the relevent Mach number range of 0.9 to 1.3 assuming the Rayleigh supersonic pitot formula (reference 14) is applied at supersonic Mach numbers to account for the bow shock. Since the LDV measured flow angles at axial station 3 were appreciably less than the nozzle metal angle of 15 deg, flow angle errors would be expected to be negligibly small. The total pressures listed in Table III represent "as measured" values that have not been corrected by the Rayleigh formula for the effect of the probe bow shock.

Total Temperature Measurements

Total temperature measurement surveys at axial stations 1 through 4 were carried out with a stagnation-temperature probe consisting of a Chromel/Alumel thermocouple housed within a 0.3 cm dia cylindrical shield. This shield was similar to that employed in Kiel head total pressure probes to reduce sensitivity to flow incidence angle. The aft end of the cylindrical shield was closed except for an 0.08 cm dia vent hole. The purpose of the vent hole was to provide a continuous supply of fluid in the cylindrical stagnation chamber to reduce conduction and radiation losses. The small size of the vent hole was selected to restrict flow such that stagnation conditions were essentially preserved.

Radial surveys were conducted along lines of constant azimuth (ϕ = 0 to 15 deg) using a remotely operated traverse unit. For measurements at station 1, an electrical circuit was used to indicate contact with the nozzle plug and therefore provide a reference point which took into account downstream motion of the plug due to thermal expansion of the rig. The temperature probe was stepped in radial increments of either 0.159 cm (stations 1, 3 and 4) or 0.318 cm (station 2) and at each position, both the probe and primary total temperature were acquired by a data logger, simultaneously. After an interval of approximately 30 sec, a second set of readings was acquired and the two results averaged to produce the probe-to-primary total temperature ratios given in Table IV.

Potential sources of error in the total temperature measurements described above were a failure to achieve a recovery factor of 1.0 and inaccuracies in the thermocouple measurement of stagnation chamber temperature. The recovery factor for the probe employed in this study was expected to be comparable to that of the Pratt & Whitney probe of similar design shown in figure D, 2.4d, p. 192 of reference 15. That probe displays a recovery factor of 0.98 at approximately Mach 0.9, decreasing to 0.95 at Mach 0.4. When such recovery factors are applied to the measured Mach number distribution of the present nozzle, measured total temperatures are calculated to be lower than actual by 0.6°K or less at stations 1 and 2 and approximately 1.7 to 2.2°K at station 3. The data shown in Table IV have not been corrected for this relatively small effect. A recovery factor assumption of 0.98 at station 3 appears reasonable should it be desired to correct the Table IV data for this effect.

Inaccuracy in the Chromel/Alumel thermocouple measurement of probe stagnation chamber temperature is estimated from reference 16 to be $\pm$ 2.8°K between 300 and 640°K, increasing to $\pm$ 3.9°K at the reference primary temperature of 756°K. The resultant probable error in the Table IV values of the ratio of probe-to-primary temperature, E_T, is given by

$$\frac{E_T}{(T_o/T_{op})} = \sqrt{\left(\frac{\Delta T_o}{T_o}\right)^2 + \left(\frac{\Delta T_{op}}{T_{op}}\right)^2} \qquad \text{(A5)}$$

The calculated percentage probable error in temperature ratio obtained by taking T_{op} = 756°K, ΔT_{op} = 4°K, T_o = 290 to 756°K and T_o = 2.8 to 3.9°K, therefore, varies between 0.7 percent and 1.1 percent.

Nozzle Mass Flowrate Measurement

The total air mass flow to the test nozzle was measured with a 3.561 cm throat diameter ASME long radius, low beta series flow nozzle (discharge coefficient = 0.997) located downstream of the inlet plenum as shown in figure 4. This nozzle was choked for both hot and cold flow test conditions. In addition to this air, nitrogen used to inject LDV seed particles into the flow was introduced at the rate of 0.018 kg/sec downstream of this nozzle but upstream of the primary/secondary flow splitter.

A venturi was provided in the primary stream to measure primary mass flowrate. This venturi was choked for cold flow conditions but unchoked for hot flow. The upstream flow nozzle was used to calibrate the venturi by blocking off the secondary duct and throttling the primary duct downstream of the venturi to achieve various venturi inlet-to-throat pressure ratios. In the heater downstream of the venturi, propane was injected into the primary stream at the rate of 0.023 kg/sec.

The following table provides measured primary and secondary mass flow rates for both hot and cold test conditions at reference conditions as defined in Table A1, that is, cold flow mass flowrates pertain to a nozzle stagnation temperature of 289°K whereas hot flow mass flowrates are based upon a secondary total temperature of 302°K and primary total temperature of 756°K. Listed flowrates include both injected nitrogen and propane and are given in both International and U.S. customary units.

TABLE A2

NOZZLE MASS FLOWRATES AT REFERENCE CONDITIONS, KG/SEC (LB/SEC)

	Cold Flow	Hot Flow
Primary Stream	2.21 (4.88)	1.36 (2.99)
Secondary Stream	1.82 (4.01)	1.61 (3.55)

Based on pressure gage accuracies of 0.1 percent and thermocouple accuracies given previously in this appendix, uncertainties in the calculated flowrates are as follows: 0.5 percent for total and primary stream flowrate; 1.4 percent for secondary stream flowrate.

Temperature Compensation

Since air supply temperature varied during the test program, as discussed above, LDV velocity data had to be corrected for this effect. It was assumed (and subsequently demonstrated by the test results) that the Mach number distribution within the nozzle was independent of inlet total temperature. Measured velocities can therefore be corrected to reference total temperature conditions by multiplying them by the square-root of the ratio of reference-to-measured total temperature. This correction was applied to all LDV data.

APPENDIX B

DATA REDUCTION

Rejection of Data

Chauvenet's criterion (reference 17) was applied as a consistent method for rejecting data. This criterion states that any data point out of a series of n points obtained under nominally identical conditions shall be rejected if the magnitude of its deviation from the mean is such that the probability of occurrence, assuming a Gaussian distribution, does not exceed 1/2n. That is, a point is rejected if the inequality given below is satisfied:

$$1 - \frac{1}{\sqrt{2\pi}\,\sigma} \int_{-x}^{+x} e^{-\frac{y^2}{4\sigma^2}}\, dy < \frac{1}{2n} \qquad \text{(B1)}$$

where y is the deviation from the mean, $\overline{Y}$, and σ is the standard deviation. In application, the mean and standard deviation are calculated from the complete data set and equation (1) defines a maximum deviation, Y_{max}, which if exceeded by a given point, results in point rejection. The maximum deviation is a monotonically increasing function of n, varying from 1.15σ for n = 2 to 3.48σ for n = 1000. The criterion is applied once and then a corrected mean and standard deviation are calculated from the remaining points. In the current study, a modified form of this criterion was applied. Data were rejected if a point deviated by more than 2σ. Application of this criterion resulted in the rejection of approximately five percent of the U_x and u_x data points. While effective in eliminating spurious measurements of these two quantities, it was less effective for other velocity measurements where the degree of redundancy was significantly smaller. The criterion was also applied to pressure and temperature data.

In addition to Chauvenet's criterion, velocity data points were rejected if there was noticeable clipping of the probability distribution by the signal processor or an error in the operation of the rig or instrumentation. Pressure and temperature data were also rejected if the operating conditions exceeded the nominal bounds given in Appendix A.

Laser Data Reduction Equations

Sketch B1 below shows the three laser beam orientations used to extract axial and azimuthal velocity data with a horizontal traverse of the LDV measuring volume. Equations similar to those given below apply to axial and radial velocity measurements obtained with a vertical traverse. $\hat{U}_1$, $\hat{U}_2$, and $\hat{U}_3$ represent the magnitudes of the instantaneous velocity in the directions indicated by the sketch during a validated particle count. The angles γ, β and θ, which are defined relative to the rig axis, were measured by projecting the beams on a large screen.

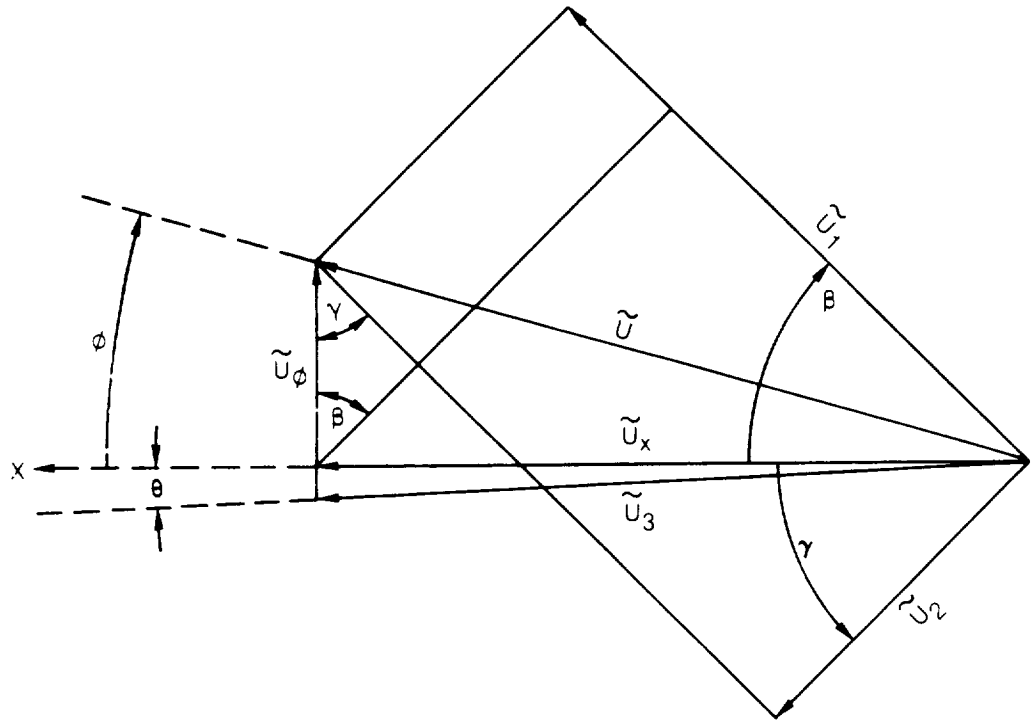

Sketch B1 — LDV Measurement Geometry in Axial-Radial Plane

Angle θ typically deviated from zero by less than $\varepsilon = 0.026$ radians while β and γ were typically within ε of $\pi/4$ radians. The desired axial and azimuthal velocities are related to measured velocities by the following equations:

$$\tilde{U}_1 = \tilde{U}_x \cos\beta + \tilde{U}_\phi \sin\beta \tag{B2}$$

$$\tilde{U}_2 = \tilde{U}_x \cos\gamma - \tilde{U}_\phi \sin\gamma \tag{B3}$$

$$\tilde{U}_3 = \tilde{U}_x \cos\theta - \tilde{U}_\phi \sin\theta \tag{B4}$$

Taking each velocity, $\tilde{U}$, as the sum of a mean, $\bar{U}$, and fluctuating part, u(t), and time averaging yields the mean velocity equations (B5) through (B7) whereas squaring, time averaging and subtracting the mean flow equations yields the turbulence equations (B8) through (B10).

$$U_x = \frac{U_2 + \left(\frac{\sin\beta}{\sin\gamma}\right) U_1}{\left(\cos\beta + \frac{\cos\gamma\sin\beta}{\sin\gamma}\right)} \tag{B5}$$

$$U_\phi = \frac{U_1\left(\frac{\cos\gamma}{\cos\beta}\right) - U_2}{\left(\frac{\sin\beta\cos\gamma}{\cos\beta} + \sin\gamma\right)} \tag{B6}$$

$$U_x = \frac{U_3}{\cos\theta} - O(U_\phi\epsilon) \tag{B7}$$

$$\overline{u_\phi^2} = \frac{\overline{u_2^2} + \overline{u_1^2} - \overline{u_x^2}(\cos^2\beta - \cos^2\gamma) - \overline{u_\phi^2}(\sin^2\beta - \sin^2\gamma)}{2(\sin^2\beta - \sin^2\gamma)} \tag{B8}$$

$$\overline{u_x u_\phi} = \frac{\overline{u_2^2} - \overline{u_1^2} - \overline{u_x^2}(\cos^2\beta - \cos^2\gamma) - \overline{u_\phi^2}(\sin^2\beta - \sin^2\gamma)}{2(\cos\beta\sin\beta + \cos\gamma\sin\gamma)} \tag{B9}$$

$$\overline{u_x^2} = \frac{\overline{u_3^2}}{\cos^2\phi} - O(U_\phi^2\epsilon^2, u_\phi^2\epsilon^2) \tag{B10}$$

The symbol O ( ) denotes the order of additional small terms which were neglected. The measurement of U_x is redundant in that equations (B5) and (B7) are independent. The equations for radial components U_r, u_r^2 and $\overline{u_x u_r}$ result from substituting the subscript, r, for, ϕ, in equations (B5) through (B10).

APPENDIX C

CONFIDENCE INTERVALS FOR LDV VELOCITY MEASUREMENTS

The number of validated LDV seed particle samples used in this study to construct velocity probability distributions was based on desired confidence intervals for the mean velocity, $\overline{V}$, and rms turbulence velocity, $v' = \sqrt{\overline{v(t)^2}}$. The results presented here are based on reference 18.

Assuming that n velocity samples, V_i, randomly selected from a population {V}, are normally distributed, an unbiased estimate of the population rms velocity is:

$$v'_p = \sqrt{\sum_{i=1}^{n} \frac{(V_i - \overline{V})^2}{n-1}} \tag{C1}$$

where the sample mean velocity, $\overline{V} = \sum_{i=1}^{n} \frac{V_i}{n}$, is an unbiased estimate of the population mean velocity V_p. For large n, v'_p is given, approximately, by the sample rms velocity v', which is:

$$v' = \sqrt{\sum_{i=1}^{n} \frac{(V_i - \overline{V})^2}{n}} \tag{C2}$$

Since the mean square turbulence velocity has a Chi-squared distribution, confidence levels for rms turbulence can be obtained from tables by entering with the number of degrees of freedom, n-1. This is inconvenient since a simple equation to predict probable error at a given confidence coefficient as a function of n is not available. For large sample size, however, (n>50), the sampling distribution of v' is approximately normal about the population standard deviation v'_p as mean with a standard deviation of $v'_p/\sqrt{2n}$.

Taking v' as a normally distributed variable with the above mean and standard deviation, the probability that a computed value of v' based on n samples differs from v'_p in either direction by more than $\lambda v'_p/\sqrt{2n}$ is given in reference 18. For the present study, a probability of 0.05 has been selected, yielding a value of λ of 1.97. This means that a computed value of v' will have a 95% probability (confidence coefficient of 0.95) that it is within $1.97\ v'_p/\sqrt{2n}$ of v'_p. At 0.95 confidence, therefore, the probable error in v' is:

$$\frac{v' - v'_p}{v'_p} = \frac{1.97}{\sqrt{2n}} \tag{C3}$$

which yields a percent error of 6.2 percent for n = 500, 4.4 percent for n = 1000 and 3.1 percent for n = 2000.

As a compromise between accuracy and data acquisition rate, a sample size of 1000 was selected for the LDV measurements. This was reduced to 500 in about five percent of the measurements, typically near the plug at station 1, where the data rate was slow.

Relative to mean velocity measurements, the sampling distribution of $\overline{V}$ is normal about $\overline{V}_p$ as a mean with standard deviation $v'_p/\sqrt{n}$. At 0.95 confidence, therefore, the probable error in $\overline{V}$ is:

$$\frac{\overline{V}-\overline{V}_p}{\overline{V}_p} = \frac{1.97}{\sqrt{n}} \left(\frac{v'_p}{V_p}\right) \qquad (C4)$$

which is a function of turbulence level. The quantity in parentheses is unknown, but can be approximated by the measured ratio of rms turbulence to mean velocity, $\frac{v'}{\overline{V}}$.

The percent error in $\overline{V}$ is tabulated below for sample sizes of 500 and 1000 and various percent turbulence levels.

Percent Uncertainty in Mean Velocity
at 0.95 Confidence
$(v'/V) \times 100$

n	1%	5%	10%	15%	20%
500	0.09	0.44	0.88	1.32	1.76
1000	0.06	0.31	0.63	0.94	1.25

The probable errors calculated above are inherent in the signal processing associated with random phenomena and are additive to any other errors in the experiment such as those due to beam orientation angle, measuring volume position, etc. If all of the above independent errors, E_{Qi}, are estimated at the same 0.95 confidence, (20 to 1 odds), they can be combined on a mean-square basis:

$$E_Q = \sqrt{\sum_{i=1}^{m} E_{Qi}^2} \qquad (C5)$$

APPENDIX D

LDV UNCERTAINTY ESTIMATES

Mean Velocity - Uncertainty estimates for LDV mean velocity and turbulence measurements can be determined by either a statistical method based on redundant measurements or by a forward calculation from component error estimates. In the former method, redundant measurements at each nozzle measurement position are used to calculate the standard deviation of the axial mean or axial turbulent velocity component at that position. These deviations are then averaged along lines of constant azimuth and uncertainty estimates for all derived quantities then calculated for each station and azimuth angle. In the latter method, probable errors are estimated for each variable that enters the LDV data reduction equations and a forward calculation of error propagation is performed to derive uncertainty bounds for each quantity. Both approaches are considered below.

The fourth columns of tables I and II provide calculated standard deviations for axial velocity, U_x, at each measurement location based on the following independent measurements:

1. direct measurement of U_x with horizontal lobe orientation (beam orientation no. 3 in figure 6(a))

2. direct measurement of U_x with vertical lobe orientation (beam orientation no. 6 in figure 6(b))

3. two values of U_x calculated using equation (B5) based on beam orientation pairs 1 and 2, and 4 and 5, of figure 6

4. repeated measurements of the above

These deviation values then averaged along lines of constant azimuth (ϕ = constant) yielding the following average standard deviations expressed as a percentage of the axial velocity:

Average Standard Deviation ($\bar{\sigma}$) for LDV Measurements
(azimuth averaged; expressed as % of U_x)

	Hot Flow			Cold Flow		
Station / ϕ, deg	1	2	3	1	2	3
0	1.9	2.2	1.7	3.3	3.3	0.3
3.75	1.1	-	-	1.0	-	-
7.5	2.5	3.3	1.0	2.9	3.6	0.4
11.25	2.6	-	-	2.6	-	-
15	2.8	3.4	1.1	4.2	5.0	0.7
AVG.	2.3	3.0	1.3	2.8	4.0	0.5

The above table can be used to estimate uncertainties for U_x, U_r and U_ϕ measurements. As noted in Appendix C, the standard deviation of the mean value of a single set of data containing "n" samples is:

$$\sigma_M = \frac{\sigma}{\sqrt{n}} \tag{D1}$$

where σ is the standard deviation of the set of samples. Since a minimum of 4 independent measurements of U_x were obtained at each measurement location (as noted in the list numbered 1-4 above), the standard deviation of the calculated mean velocity, σ_M, was a factor of two smaller than the standard deviations listed in the above table.

Assuming a Gaussian error distribution, it can be stated with 0.95 confidence (20 to 1 odds) that the true mean axial velocity lies within $2\sigma_M = \bar{\sigma}$ of the calculated mean axial velocity, U_x. The above table of $\bar{\sigma}$ values, therefore, provides estimates of the uncertainty in quoted mean axial velocity at 0.95 confidence.

Radial and azimuthal velocity components were calculated using equation (B5), which for the normal $\pm$ 45 deg beam orientations employed is:

$$U_\phi \text{ (or } U_r) = \frac{(U_2 - U_1)}{2} \tag{D2}$$

The standard deviation for U_1 and U_2 measurements was assumed to be the same as for U_x (table values, $\bar{\sigma}$). Since U_2 and U_1 were each typically measured twice, the uncertainties in U_2 and U_1 at 0.95 confidence, based on equation (D1), were $\sqrt{2}\,\bar{\sigma}$. Combining uncertainties on a mean square basis, the resultant unceratinty, $E_{U\phi}$, in U_ϕ was:

$$\frac{E_{U_\phi}}{U_x} = \sqrt{2}\,\sigma \tag{D3}$$

with a similar result applying to the radial component. The values given in the table, multiplied by $\sqrt{2}$, therefore provide one estimate of radial and azimuthal velocity component uncertainties at 0.95 confidence.

The following discusses the alternative method for estimating errors. Appendix C provides a table of mean velocity uncertainties at 0.95 confidence as a function turbulence level for LDV particle count samples of 500 and 1000. Since the maximum total turbulence level encountered in this study was approximately 25 percent (figures 31-33), a conservative single component turbulence level for estimating uncertainty is 20 percent. Based on 1000 particle counts (that used for 95% of the measurements), the table in Appendix C yields a mean velocity measurement uncertainty of 1.25%.

A second source of error was measuring volume position uncertainty which was estimated at $\pm$ 0.005 cm based on the calibration accuracy of the slide potentiometer used to indicate position. The maximum axial velocity gradient along an LDV traverse line occurred at station 1 for hot flow and was on the order of 0.18 m/sec. per 0.001 cm. This in conjunction with the quoted position uncertainty yields an uncertainty in axial velocity measurement of 0.9%. A position measurement error of 0.9% was therefore assumed as a worst case.

A third source of error is beam orientation angle, β. Although detents in the LDV optical system provide alignment at 0, -45 and +45 deg, tolerances in machined parts result in an uncertainty in β, which by a trial of twenty samples was found to be 0.1 deg at 0.95 confidence. When this uncertainty is combined with an estimated calibration error of 0.2 deg in determining the angle of the beams in the three beam orientations relative to the rig axis, a total angle uncertainty $\Delta\varepsilon$, of 0.3 deg results. By use of equation (B5) it can be shown that this uncertainty in beam angles β and λ produces a probable error on the order of $U_2\Delta\varepsilon$.

When the above three error estimates were combined, based on a measurement redundance of two, radial and aximuthal velocity measurement uncertainties were found to be 1.5% with the axial velocity uncertainty 1.3%. These estimates tend to be lower than those obtained by the statistical approach considered previously.

Since the previously discussed statistical approach was applied to the radial and azimuthal velocity components in an indirect manner, the overall conclusion drawn here is that the standard deviations shown in the table can be taken as reasonable estimates of measurement uncertainty for the axial component as well as the radial and aximuthal components. That is, the multiplying factor of 1.4 in equation (D3) appears overly conservative and therefore has been neglected.

APPENDIX E

LDV SEED PARTICLE LAG INVESTIGATION

Initial comparisons of LDV-measured, cold flow, axial velocity data at plume-plane station 3 with velocities predicted by Pratt & Whitney indicated that the measured velocities were significantly low. A series of checks showed that the LDV system was accurately measuring velocity. This indicated that the source of the problem was seed particle lag in the highly accelerated transonic flow region, within and downstream of, the nozzle. To verify that a particle lag problem existed, total and static pressure measurements were obtained on the nozzle axis in the vicinity of the nozzle exit. Calculated fluid Mach numbers were then compared to Mach numbers obtained with the LDV system.

Figure 37 shows the calibration test results. A modified Prandtl-type pitot-static probe was positioned at four axial locations in the nozzle exhaust. Part (a) of the figure shows the measured total pressure at the various locations relative to the total pressure one-half centimeter upstream of the nozzle exit. In subsonic flow this ratio should be one whereas in supersonic flow this ratio should decrease with increasing Mach number in proportion to the strength of the bow shock standing off the pitot port. This ratio provides a direct indication of local Mach number in supersonic flow by use of normal shock relations. Mach numbers derived in this manner are shown as two open circles in figure 37, part (b). In addition, probe total and static measurements in the supersonic flow region can also (through use of the Rayleigh supersonic pitot formula (reference 9)) provide an indication of local Mach number. In a flow such as this, where significant acceleration occurs over a distance equal to the total and static port separation distance, the most appropriate location to assign to the Mach number determination is the static port position. Measurements obtained in this manner are shown as squares in figure 37, part (b). These values are within 0.5 percent of the values obtained from the bow shock total pressure ratios discussed above.

In the subsonic flow region (x less than approximately 2 cm), the conventional pitot-static isentropic relations were employed to obtain Mach number. These measurements are shown as inverted triangles. As shown in the figure, local Mach numbers derived from these three pneumatic measurement techniques appear consistent.

LDV measurements of velocity were acquired at five locations and converted to local Mach number assuming adiabatic flow. These data are shown as triangles. The LDV data are consistently low relative to pneumatic results with the error on the order of 11.5 to 14.8 percent. This demonstrated that a serious particle lag problem existed.

Development of an improved seeding system was initiated based on seed particle size distribution measurements, development of a computer program to calculate particle lag in compressible nozzle flow and LDV measurements in a calibration jet. This development effort is described in detail elsewhere (Patrick and Paterson, reference 19). The lag problem was eventually eliminated by implementing a series of changes in test technique and seed system design. These included changes in seed handling procedures, use of a vortex-tube separator in the seeding system to remove large particles, application of Chauvenet's criterion in the on-line reduction of data to discriminate against large seed particle samples and use of forward rather than back-scatter collection.

At the conclusion of this development effort, on-axis Mach number at plume-plane station 3 was measured with the LDV system and compared to that obtained from total and static pressure measurements. While total pressure is readily obtained, static pressure is difficult to determine accurately. To measure static pressure, a small tube was attached to the nozzle plug and extended on-axis through the nozzle exit with the pneumatic connection made about two nozzle diameters downstream. A ring of four static ports in the tube was aligned with the axial position of station 3. Comparison of Mach number determined in this manner with LDV results showed agreement within 1.3 percent. Given the uncertainty bounds in both measurements, this was considered acceptable.

TABLE I
NOZZLE LDV VELOCITY DATA FOR HOT FLOW TEST CONDITIONS

$T_{op} = 755\,°K$; $T_{os} = 302\,°K$

AXIAL STATION 1, AZIMUTHAL POSITION $\phi = 0$ deg

r, cm	R	U_x, m/sec	$\sigma U_x/U_x$ × 100, %	U_r, m/sec	U_r/Ux × 100, %	U_ϕ m/sec	U_ϕ/U_x × 100, %	u_x, m/sec	u_r, m/sec	u_ϕ, m/sec	$\overline{u_x u_\phi}$, m^2/sec^2	$\overline{u_x u_r}$, m^2/sec^2	σ_{u_x}/u_x × 100, %
3.658	0.093	144.3	3.3	-14.2	-9.8	—	—	12.3	5.3	—	—	-14	1.7
3.937	0.143	154.1	0.3	-6.9	-4.5	—	—	9.7	4.1	—	—	—	14.6
4.064	0.165	158.3	1.5	0.5	0.3	—	—	8.9	4.0	—	—	- 9	3.7
4.343	0.215	161.3	1.7	5.5	3.4	3.5	2.2	6.9	3.1	3.6	3	- 9	13.2
4.572	0.255	163.6	0.9	10.7	6.5	—	—	—	—	—	—	—	—
4.978	0.327	161.8	1.2	13.2	8.2	1.0	0.6	7.1	3.2	2.7	0	4	2.0
5.207	0.367	166.9	2.0	13.9	8.3	—	—	—	—	—	—	—	—
5.613	0.439	156.2	0.9	8.3	5.3	2.1	1.3	7.2	4.7	4.7	- 4	10	10.9
5.842	0.479	160.9	3.2	10.2	6.3	—	—	8.9	5.1	—	—	—	—
6.248	0.551	146.0	2.5	9.5	6.5	3.4	2.3	9.5	6.1	3.3	-12	21	6.9
6.477	0.592	147.1	1.2	16.7	11.4	—	—	—	—	—	—	—	—
6.883	0.663	145.9	2.6	15.7	10.8	-4.0	-2.7	7.8	4.7	4.7	- 5	3	6.0
7.112	0.704	148.9	1.0	13.3	8.9	—	—	—	—	—	—	—	—
7.518	0.776	141.6	5.4	17.3	12.2	0.5	0.4	9.1	5.2	8.9	2	11	22.9
8.153	0.888	47.9	11.5	—	—	-2.1	-4.3	7.1	—	—	-15	—	7.8

AXIAL STATION 1, AZIMUTHAL POSITION $\phi = 3.75$ deg

4.064	0.165	158.1	1.5	-5.2	-3.3	—	—	6.8	7.1	—	4	-15	—
4.343	0.215	162.3	1.1	1.8	1.1	-1.7	-1.0	6.8	2.5	5.1	4	1	19.6
4.978	0.327	162.0	0.3	7.0	4.3	-1.0	-0.6	7.0	4.0	4.7	7	14	14.2
5.613	0.439	157.7	0.9	16.4	10.4	1.0	0.6	7.0	3.1	4.1	6	3	8.3
6.248	0.551	151.9	1.0	16.1	10.6	2.4	1.6	7.8	4.4	5.4	-5	7	10.3
6.883	0.663	151.7	2.1	15.1	10.0	-3.1	-2.0	7.9	5.7	4.7	-6	6	9.7
7.518	0.776	100.3	—	-19.3	-19.2	-1.1	-1.1	8.9	5.9	3.7	7	-20	7.1
8.153	0.888	53.3	—	—	—	-3.3	-6.2	5.0	—	2.3	-1	—	—

TABLE I CONTINUED
NOZZLE LDV VELOCITY DATA FOR HOT FLOW TEST CONDITIONS

$T_{op} = 755°K$; $T_{os} = 302°K$

AXIAL STATION 1, AZIMUTHAL POSITION $\phi = 7.5$ deg

r, cm	R	U_x, m/sec	$\sigma U_x/U_x$ × 100,%	U_r, m/sec	U_r/Ux × 100,%	U_ϕ m/sec	U_ϕ/U_x × 100,%	u_x, m/sec	u_r, m/sec	u_ϕ, m/sec	$\overline{u_x u_\phi}$, m^2/sec^2	$\overline{u_x u_r}$, m^2/sec^2	σ_{u_x}/u_x × 100,%
4.064	0.165	155.5	1.9	-7.8	-5.0	—	—	8.0	5.2	—	—	-6	7.1
4.343	0.215	159.0	1.1	0	0	-6.7	-4.2	7.7	3.4	2.1	7	-5	5.8
4.978	0.327	160.2	0.9	11.8	7.4	-3.9	-2.4	8.9	2.8	4.0	4	3	—
5.613	0.439	154.4	2.5	-24.7	-16.0	-0.3	0.2	12.9	—	4.9	-2	10	—
5.918	0.493	138.1	—	-24.2	-17.5	—	—	14.4	—	—	—	—	—
6.248	0.551	129.7	2.3	-21.5	16.6	7.2	5.6	16.4	—	6.6	-7	2	—
6.553	0.605	76.1	—	-19.9	26.1	—	—	12.9	—	—	—	—	—
6.883	0.663	56.9	4.8	-17.5	-30.8	1.1	1.9	5.8	—	6.3	12	0	—
7.087	0.699	51.1	—	-16.9	-33.1	—	—	3.9	—	—	—	—	—
7.518	0.776	52.4	3.9	-11.7	-20.4	1.4	2.4	3.6	1.3	5.1	1	1	32.1
8.153	0.888	47.0	2.6	—	—	-0.8	-1.7	4.8	—	1.8	2	—	1.1

AXIAL STATION 1, AZIMUTHAL POSITION $\phi = 11.25$ deg

4.064	0.165	48.8	1.8	-22.5	-46.1	-4.4	-9.0	2.8	3.1	3.6	0	4	6.3
4.343	0.215	53.1	3.8	-26.1	-49.2	-3.3	-6.2	4.0	4.7	1.7	0	—	45.0
4.978	0.327	55.5	4.1	-25.0	-45.0	-1.5	-2.7	2.8	1.9	1.7	0	2	6.3
5.613	0.439	55.7	3.8	-22.8	-40.9	-0.3	-0.5	2.6	1.9	1.7	0	2	2.2
6.248	0.551	54.2	2.8	-19.0	-35.1	1.1	2.0	2.5	1.6	1.8	0	2	0
6.883	0.663	53.4	1.5	-14.9	-27.9	0.8	1.5	2.7	1.0	1.9	1	2	9.6
7.518	0.776	50.6	1.0	-11.7	-23.1	0.1	0.2	3.4	2.8	1.5	1	2	3.9
8.153	0.888	44.0	2.3	-22.5	-51.1	0.8	1.8	5.0	—	2.4	3	2	—

AXIAL STATION 1, AZIMUTHAL POSITION $\phi = 15$ deg

3.858	0.093	121.3	—	30.0	-24.7	—	—	13.1	16.9	—	—	-16	—
3.937	0.143	49.5	2.6	-22.7	-45.9	-0.5	-1.0	3.2	4.1	3.0	0	-3	22.1
4.343	0.215	52.0	3.2	-25.4	-48.8	0.5	1.0	3.0	2.4	2.7	1	-3	21.3
4.572	0.255	53.8	1.3	-25.8	-48.0	—	—	3.5	2.1	—	—	-4	—
4.978	0.327	56.2	1.8	-25.3	-45.0	—	—	2.6	1.4	2.3	0	-1	4.2
5.207	0.367	56.3	3.7	-25.2	-44.8	0	0	2.6	2.1	—	—	-2	—
5.613	0.439	55.7	2.9	-22.6	-40.6	-0.4	-0.7	2.5	1.6	2.1	-1	-1	0.6
6.248	0.551	55.7	3.9	-17.7	-31.8	-0.7	-1.3	2.4	1.7	2.2	0	1	5.9
6.883	0.663	53.9	3.0	-15.6	-28.9	-0.6	-1.1	2.8	1.3	1.8	0	0	4.3
7.518	0.776	50.6	4.0	-12.4	-24.5	-1.3	-2.6	4.1	1.0	2.1	2	1	5.5
8.153	0.888	41.1	1.5	—	—	-0.5	-1.2	5.2	—	3.8	2	—	—

TABLE I CONTINUED
NOZZLE LDV VELOCITY DATA FOR HOT FLOW TEST CONDITIONS

$T_{op} = 755°K$; $T_{os} = 302°K$

AXIAL STATION 2, AZIMUTHAL POSITION $\phi = 0$ deg

r, cm	R	U_x, m/sec	$\sigma U_x/U_x$ × 100, %	U_r, m/sec	U_r/Ux × 100, %	U_ϕ m/sec	U_ϕ/U_x × 100, %	u_x, m/sec	u_r, m/sec	u_ϕ, m/sec	$\overline{u_x u_\phi}$, m^2/sec^2	$\overline{u_x u_r}$, m^2/sec^2	σ_{u_x}/u_x × 100, %
0	0	99.9	3.3	0.1	0.1	5.4	5.4	9.4	11.7	10.5	13	-11	13.2
0.968	0.127	114.7	2.5	-1.3	-1.1	-9.0	-7.8	7.8	11.5	12.1	-14	-35	3.7
1.798	0.236	104.3	2.4	2.5	2.4	-1.7	-1.6	10.3	10.3	11.4	-15	34	6.0
2.642	0.346	84.8	1.4	-0.7	-0.8	2.1	2.5	9.9	8.5	10.4	-1	7	0.6
3.454	0.453	85.5	3.0	4.2	4.9	4.5	5.3	10.1	8.8	9.8	4	11	4.8
4.293	0.563	109.1	2.7	2.3	2.1	3.5	3.2	14.0	15.3	12.3	18	-44	15.0
5.131	0.673	142.3	2.2	11.1	7.8	2.5	1.8	14.9	15.0	12.3	-40	-85	17.9
5.969	0.783	151.9	1.8	5.0	3.3	2.8	1.8	11.9	6.1	6.1	26	23	30.2
6.782	0.889	148.0	0.9	—	0.6	-2.2	-1.5	12.0	—	9.0	-38	—	9.4

AXIAL STATION 2, AZIMUTHAL POSITION $\phi = 7.5$ deg

0	0	99.9	3.3	0.1	0.1	5.4	5.4	9.4	11.7	10.5	13	-11	13.2
0.968	0.127	110.7	1.1	0	0	-10.6	-9.5	7.8	10.8	10.2	-8	-19	4.5
1.798	0.236	102.7	0.3	-3.6	-3.5	-0.3	-0.3	10.5	9.5	12.6	-35	41	5.4
2.642	0.346	89.4	1.1	-6.7	-7.5	0.3	0.3	9.7	7.8	11.6	-4	2	12.4
3.454	0.453	85.5	2.3	-6.2	-7.3	-0.7	-0.8	9.7	9.9	11.3	22	-6	0.7
4.293	0.563	102.6	5.2	-4.8	-4.7	-3.0	-2.9	13.1	8.9	14.7	78	10	13.5
5.131	0.673	121.0	6.2	-8.5	-7.0	-4.6	-3.8	14.7	6.3	17.3	145	-11	3.3
5.969	0.783	124.8	5.4	-7.6	-6.1	-5.2	-4.2	16.4	8.7	15.7	135	25	11.6
6.782	0.889	101.4	4.4	—	—	-5.3	-5.2	16.2	—	—	139	—	—

AXIAL STATION 2, AZIMUTHAL POSITION $\phi = 15$ deg

0	0	99.9	3.3	0.1	0.1	5.4	5.4	9.4	11.7	10.5	13	-11	13.2
0.968	0.127	114.3	5.4	0.7	0.6	-10.5	-9.2	10.7	6.9	9.3	-27	-20	—
1.798	0.236	109.5	2.0	-0.5	-0.5	-1.0	-0.9	10.9	11.0	9.8	-30	35	7.2
2.642	0.346	82.4	2.7	-3.8	-4.6	-0.1	-0.1	10.3	8.6	11.8	20	15	15.7
3.454	0.453	77.8	2.1	-6.2	-8.0	-0.3	-0.4	9.0	8.7	9.1	29	1	6.1
4.293	0.563	80.8	3.7	-9.6	-11.9	1.9	2.4	11.2	10.0	10.6	-2	0	8.3
5.131	0.673	75.8	4.6	-10.9	-14.4	-1.3	-1.7	10.9	9.2	11.5	4	5	14.0
5.969	0.783	62.8	5.4	-7.2	-11.5	0.2	0.3	8.3	8.4	8.7	9	2	17.2
6.782	0.889	57.9	1.4	—	—	-0.1	-0.2	6.4	—	6.4	-5	—	2.5

TABLE I CONTINUED
NOZZLE LDV VELOCITY DATA FOR HOT FLOW TEST CONDITIONS

$T_{op} = 755°K$; $T_{os} = 302°K$

AXIAL STATION 3, AZIMUTHAL POSITION $\phi = 0$ deg

r, cm	R	U_x, m/sec	$\sigma U_x/U_x$ × 100, %	U_r, m/sec	U_r/U_x × 100, %	U_ϕ m/sec	U_ϕ/U_x × 100, %	u_x, m/sec	u_r, m/sec	u_ϕ, m/sec	$\overline{u_x u_\phi}$, m^2/sec^2	$\overline{u_x u_r}$, m^2/sec^2	σ_{u_x}/u_x × 100, %
0	0	397.0	0.6	1.3	0.3	2.3	0.6	15.4	6.9	13.7	-4	4	4.0
0.594	0.127	395.7	0.9	2.0	0.5	-12.4	-3.1	13.7	7.1	9.1	29	16	16.7
1.102	0.236	390.0	1.5	9.0	-2.3	-12.6	-3.2	16.6	9.5	10.1	10	92	11.3
1.613	0.345	368.0	1.2	-13.8	-3.8	-2.8	-0.8	14.2	9.7	10.8	4	37	15.4
2.121	0.454	368.4	1.0	10.8	-2.9	0.7	0.2	11.8	11.5	9.9	22	4	9.1
2.642	0.565	381.6	0.8	12.4	-3.2	2.5	0.7	13.3	11.3	11.9	21	6	4.6
3.150	0.674	399.1	1.9	20.0	-5.0	3.7	0.9	13.7	15.9	14.1	5	-63	17.4
3.658	0.783	429.4	3.1	-14.8	-3.4	-6.7	-1.6	17.2	16.4	16.3	-4	-35	3.0
4.166	0.891	463.4	3.1	-13.3	-2.9	-4.2	-0.9	17.6	20.5	18.0	1	3	8.1
4.445	0.951	491.0	2.9	-14.4	-2.9	-6.2	-1.3	19.8	21.5	20.3	61	58	5.3

AXIAL STATION 3, AZIMUTHAL POSITION $\phi = 7.5$ deg

0	0	397.0	0.6	1.3	0.3	2.3	0.6	15.4	6.9	13.7	-4	4	4.0
0.594	0.127	389.5	1.1	-2.0	-0.5	-12.0	-3.1	13.9	8.9	9.7	-14	61	10.9
1.102	0.236	382.3	2.5	-9.1	-2.4	-9.2	-2.4	17.1	5.1	8.9	-40	87	5.6
1.613	0.345	370.3	0.8	-14.2	-3.8	-5.2	-1.4	15.7	5.1	9.3	-4	69	2.2
2.121	0.454	366.3	1.2	-13.0	-3.5	-7.1	-1.9	11.7	8.6	10.7	-11	5	0.2
2.642	0.565	381.8	0.9	-15.9	-4.2	-3.1	-0.8	13.1	10.2	11.1	-8	2	5.8
3.150	0.674	400.7	1.3	-26.5	-6.6	-1.2	-0.3	13.7	17.1	13.1	-1	-5	1.2
3.658	0.783	431.8	0.8	-34.2	-7.9	-7.3	-1.7	15.7	17.2	15.5	-18	-46	0.3
4.166	0.891	468.4	0.5	-29.9	-6.4	-0.8	-0.2	18.6	19.2	17.0	56	—	0.1
4.445	0.951	489.5	0.5	-26.6	-5.4	5.7	1.2	22.2	14.7	20.6	128	—	9.9

AXIAL STATION 3, AZIMUTHAL POSITION $\phi = 15$ deg

0	0	397.0	0.6	1.3	0.3	2.3	0.6	15.4	6.9	13.7	-4	4	4.0
0.594	0.127	391.5	1.0	-0.4	-0.1	-11.0	-2.8	12.9	9.6	8.7	29	29	8.9
1.102	0.236	384.9	0.9	-10.1	-2.6	-13.3	-3.4	14.8	8.2	8.6	-4	69	21.5
1.613	0.345	364.5	1.0	-14.7	-4.1	4.7	1.3	15.9	8.6	—	31	56	0.9
2.121	0.454	370.9	1.2	-13.0	-3.5	2.6	0.7	11.9	9.5	9.7	21	4	4.8
2.642	0.565	381.2	1.2	-22.0	-5.8	-1.5	-0.4	12.6	14.5	11.7	-8	-9	14.0
3.150	0.674	400.2	1.1	-26.9	-6.8	3.8	0.9	14.4	15.9	11.8	21	8	0.5
3.658	0.783	432.7	0.7	-36.6	-8.5	2.8	0.6	15.5	18.0	17.8	-16	-29	6.8
4.166	0.891	471.3	1.5	-26.8	-5.7	-1.7	-0.4	18.1	14.5	18.5	24	-9	12.9
4.445	0.951	484.1	1.9	-20.6	-4.3	-3.3	-0.7	18.6	13.3	20.5	-39	-3	4.7

TABLE I (CONTINUED)
NOZZLE LDV VELOCITY DATA FOR HOT FLOW TEST CONDITIONS

$T_{op} = 755°K$; $T_{os} = 302°K$

AXIAL STATION 4, AZIMUTHAL POSITION $\phi = 7.5$ deg

r, cm	R	U_x, m/sec	$\sigma U_x/U_x \times 100$, %	U_r, m/sec	$U_r/Ux \times 100$, %	u_x, m/sec	u_r, m/sec	$\overline{u_x u_r}$, m^2/sec^2
0	0	357.1	0.3	4.8	1.3	12.6	8.3	11
0.594	0.127	348.0	1.0	2.3	0.7	13.0	9.8	13
1.102	0.236	345.2	0.3	-6.4	-1.9	12.4	8.5	33
1.613	0.345	330.8	1.6	-16.0	-4.8	13.0	10.7	69
2.121	0.454	322.6	0.9	-22.6	-7.0	10.0	9.5	16
2.642	0.565	329.0	1.3	-28.3	-8.6	11.0	12.0	27
3.150	0.674	344.1	0.6	-31.9	-9.3	13.3	13.5	-52
3.658	0.783	361.5	1.9	-46.2	-12.8	13.9	13.2	-24
4.166	0.891	379.6	0	-60.6	-16.0	15.0	9.0	-38
4.445	0.951	393.5	0.2	-75.9	-19.3	15.5	16.6	-108

TABLE II
NOZZLE LDV VELOCITY DATA FOR COLD FLOW TEST CONDITIONS

$T_{op} = 289°K$; $T_{os} = 289°K$

AXIAL STATION 1, AZIMUTHAL POSITION $\phi = 0$ deg

r, cm	R	U_x, m/sec	σ_{U_x}/U_x × 100, %	U_r, m/sec	U_r/U_x × 100, %	U_ϕ m/sec	U_ϕ/U_x × 100, %	u_x, m/sec	u_r, m/sec	u_ϕ, m/sec	$\overline{u_x u_\phi}$, m^2/sec^2	$\overline{u_x u_r}$, m^2/sec^2	σ_{u_x}/u_x × 100, %
3.937	0.165	101.3	2.5	-4.7	-4.6	5.2	5.1	4.7	3.7	4.6	-6	-1	17.8
4.343	0.235	102.3	3.4	1.7	1.7	1.9	1.9	4.1	3.9	4.1	-3	-2	4.7
4.978	0.344	104.6	3.2	6.4	6.1	-0.8	-0.8	3.8	4.9	2.9	0	4	3.9
5.613	0.454	102.0	3.8	7.8	7.6	0.6	0.6	4.2	3.0	2.8	-1	-1	4.5
6.248	0.563	93.1	4.8	7.1	7.6	3.0	3.2	5.9	2.0	4.7	-6	1	15.1
6.883	0.672	93.6	1.4	8.9	9.5	-4.8	-5.1	5.5	3.0	5.0	-14	0	16.8
7.518	0.781	94.0	2.3	6.1	6.5	-3.8	-4.0	6.5	4.4	4.1	0	12	17.4
8.153	0.891	40.7	4.7	—	—	-4.4	-10.8	4.2	—	3.7	-2	—	9.5

AXIAL STATION 1, AZIMUTHAL POSITION $\phi = 3.75$ deg

3.937	0.165	101.7	0.4	-2.6	-2.6	1.0	1.0	4.2	3.7	2.4	-3	2	12.1
4.343	0.235	103.2	1.0	1.5	1.5	0.6	0.6	3.8	1.8	2.8	-1	0	5.5
4.978	0.344	102.8	1.6	6.2	6.0	0.3	0.3	3.9	1.9	2.2	-1	1	4.1
5.613	0.454	100.2	0.8	8.6	8.6	0.8	0.8	4.3	2.3	2.9	0	2	11.4
6.248	0.563	95.4	1.4	10.0	10.5	2.3	2.4	4.4	4.4	3.4	0	3	14.5
6.883	0.672	92.4	1.4	9.1	9.8	0	0	4.7	5.8	4.7	-7	14	6.4
7.518	0.781	75.8	—	-9.1	-12.0	-2.7	-3.6	8.5	3.2	—	-2	-6	27.0
8.153	0.891	48.8	0.4	—	—	1.6	3.3	3.4	—	1.7	1	—	—

AXIAL STATION 1, AZIMUTHAL POSITION $\phi = 7.5$ deg

3.937	0.165	104.2	3.0	-11.0	-10.6	-8.9	-8.5	4.6	2.1	3.0	0	-1	19.3
4.343	0.235	104.9	2.3	-2.4	-2.3	-6.1	-5.8	4.0	2.4	2.9	0	1	19.0
4.978	0.344	102.6	1.9	4.9	4.8	-3.8	-3.7	5.1	2.0	3.6	-1	2	11.6
5.613	0.454	98.1	0.7	6.1	6.2	-2.2	-2.2	6.5	6.0	4.4	0	19	—
6.248	0.563	85.3	2.6	-0.8	-0.9	1.2	1.4	11.6	7.2	5.1	9	15	—
6.883	0.672	52.4	3.4	-15.9	-30.3	1.1	2.1	3.1	6.2	1.9	0	-6	16.6
7.518	0.781	48.0	2.9	-10.1	-21.0	0.8	1.7	3.9	0.2	0.8	2	0	9.0
8.153	0.891	38.8	6.7	—	—	0.6	1.5	4.7	—	2.2	2	—	—

TABLE II
NOZZLE LDV VELOCITY DATA FOR COLD FLOW TEST CONDITIONS (CONTINUED)

$T_{op} = 289°K$; $T_{os} = 289°K$

AXIAL STATION 1, AZIMUTHAL POSITION $\phi = 11.3$ deg

r, cm	R	U_x, m/sec	σ_{U_x}/U_x × 100, %	U_r, m/sec	U_r/U_x × 100, %	U_ϕ m/sec	U_ϕ/U_x × 100, %	u_x, m/sec	u_r, m/sec	u_ϕ, m/sec	$\overline{u_x u_\phi}$, m^2/sec^2	$\overline{u_x u_r}$, m^2/sec^2	σ_{u_x}/u_x × 100, %
3.937	0.165	48.5	3.7	-23.5	-48.5	-1.7	-3.5	3.5	2.0	1.7	2	-5	6.3
4.343	0.235	52.1	4.0	-24.2	-46.4	-2.4	-4.6	3.1	2.0	1.2	0	-1	6.3
4.978	0.344	54.4	2.0	-23.4	-43.0	-0.8	-1.5	2.6	1.8	1.3	0	-1	1.6
5.613	0.454	54.1	1.5	-19.9	-36.8	0	0	2.4	1.7	1.9	0	-1	11.5
6.248	0.563	53.5	1.1	-16.0	-29.9	0.7	1.3	2.5	1.0	2.0	0	0	19.5
6.883	0.672	52.1	1.0	-12.3	-23.6	1.3	2.5	2.8	0.9	2.5	0	0	19.7
7.518	0.781	48.3	1.7	-9.4	-19.5	1.7	3.5	4.0	1.7	1.8	1	-1	7.8
8.153	0.891	38.6	5.4	—	—	1.8	4.7	5.4	—	2.8	5	—	—

AXIAL STATION 1, AZIMUTHAL POSITION $\phi = 15$ deg

3.937	0.165	45.6	3.1	-19.9	-43.6	-1.5	-3.3	3.3	3.2	2.2	4	-5	5.9
4.343	0.235	51.5	5.0	-22.6	-43.9	-1.1	-2.1	2.8	2.7	1.4	0	-4	7.8
4.978	0.344	53.6	1.7	-23.1	-43.1	-1.3	-2.4	2.3	1.6	1.9	1	-1	11.9
5.613	0.454	53.4	1.7	-20.2	-37.8	-1.1	-2.1	2.4	1.2	1.7	0	-1	10.9
6.248	0.563	52.5	2.5	-17.7	-33.7	-1.5	-2.9	2.4	0.8	1.9	0	0	10.5
6.883	0.672	50.1	4.8	-13.3	-26.5	-1.6	-3.2	3.2	0.8	2.0	0	0	7.7
7.518	0.781	48.3	3.9	-10.4	-21.5	-1.5	-3.1	4.2	1.8	1.9	-1	1	12.3
8.153	0.891	36.3	11.0	—	—	-1.4	-3.9	4.9	—	3.3	0	—	12.2

TABLE II
NOZZLE LDV VELOCITY DATA FOR COLD FLOW TEST CONDITIONS

$T_{op} = 289\,°K$; $T_{os} = 289\,°K$

AXIAL STATION 2, AZIMUTHAL POSITION $\phi = 0$ deg

r, cm	R	U_x, m/sec	$\sqrt{u_x^2}/U_x$ x 100, %	U_r, m/sec	U_r/U_x x 100, %	U_ϕ m/sec	U_ϕ/U_x x 100, %	u_x, m/sec	u_r, m/sec	u_ϕ m/sec	$\overline{u_x u_\phi}$, m^2/sec^2	$\overline{u_x u_r}$, m^2/sec^2
0	0	65.3	3.5	1.9	2.9	-7.8	-11.9	4.7	8.6	5.3	-5	-5
0.968	0.127	77.4	5.8	1.2	1.6	-6.7	-8.7	4.6	4.2	4.5	-5	-5
1.798	0.236	72.9	5.3	1.7	2.3	-3.1	-4.3	6.4	4.7	4.6	-11	8
2.642	0.346	67.7	3.8	0.6	0.9	-1.5	-2.2	6.2	5.1	5.6	-21	2
3.454	0.453	71.4	0.4	1.7	2.4	-2.3	-3.2	6.3	5.8	6.9	-19	-5
4.293	0.563	89.2	0.8	4.4	4.9	-5.0	-5.6	6.5	7.1	5.1	-5	-4
5.131	0.673	99.2	3.1	6.3	6.4	-3.6	-3.6	3.8	5.3	3.4	0	0
5.969	0.783	97.0	3.4	6.7	6.9	-5.5	-5.7	6.5	—	2.8	-3	0
6.604	0.866	89.9	—	—	—	-7.1	-7.9	5.2	—	—	—	—
6.782	0.889	88.8	—	—	—	—	—	3.2	—	—	—	—

AXIAL STATION 2, AZIMUTHAL POSITION $\phi = 7.5$ deg

0	0	65.3	3.5	1.9	2.9	-7.8	-11.9	4.7	8.6	5.3	-9	-6
0.968	0.127	80.6	4.2	-0.2	-0.2	-6.1	-7.6	4.7	4.3	5.7	-9	-7
1.798	0.236	77.3	2.7	1.3	1.7	-1.3	-1.7	6.4	4.5	6.1	-3	7
2.642	0.346	70.7	1.7	0	0	-1.9	-2.7	6.7	4.9	6.7	13	-2
3.454	0.453	70.8	6.1	-2.6	-3.7	-4.2	-5.9	7.6	3.2	6.7	23	0
4.293	0.563	72.9	1.6	-1.0	-1.4	-2.6	-3.6	8.6	5.7	7.3	34	12
5.131	0.673	81.1	5.9	-5.2	-6.4	-2.0	-2.5	8.7	7.7	7.9	35	1
5.969	0.783	85.8	3.4	-1.7	-2.0	0.2	0.2	8.7	8.5	7.1	31	7
6.604	0.866	73.3	—	—	—	-0.8	-1.1	10.6	—	5.3	42	—
6.782	0.889	72.1	—	—	—	-2.0	-2.8	10.6	—	6.7	47	—

AXIAL STATION 2, AZIMUTHAL POSITION $\phi = 15$ deg

0	0	65.3	3.5	1.9	2.9	-7.8	-11.9	4.7	8.6	5.3	-8	-2
0.968	0.127	83.5	1.1	1.5	1.8	-7.3	-8.7	5.1	6.9	5.4	-9	5
1.798	0.236	79.4	5.2	2.6	3.3	-0.9	-1.1	6.5	5.0	6.9	-5	4
2.642	0.346	63.9	1.1	-0.7	-1.1	-1.6	-2.5	4.8	5.8	6.2	5	3
3.454	0.453	61.9	7.3	-4.0	-6.5	-2.8	-4.5	4.1	3.7	3.1	0	2
4.293	0.563	64.0	9.8	-7.1	-11.0	-2.6	-4.1	5.1	3.5	4.3	1	5
5.131	0.673	60.5	7.4	-8.7	-14.4	-1.7	-2.8	6.0	4.4	3.5	-2	-2
5.969	0.783	54.6	6.0	-4.8	-8.8	-0.4	-0.7	5.0	5.3	4.2	-1	6
6.782	0.889	52.9	3.2	—	—	-0.2	-0.4	5.0	—	5.4	-6	—

TABLE II
NOZZLE LDV VELOCITY DATA FOR COLD FLOW TEST CONDITIONS (CONTINUED)

$T_{op} = 289°K$; $T_{os} = 289°K$

AXIAL STATION 3, AZIMUTHAL POSITION $\phi = 0$ deg

r, cm	R	U_x, m/sec	σ_{U_x}/U_x × 100, %	U_r, m/sec	U_r/U_x × 100, %	U_ϕ m/sec	U_ϕ/U_x × 100, %	u_x, m/sec	u_r, m/sec	u_ϕ, m/sec	$\overline{u_x u_\phi}$, m^2/sec^2	$\overline{u_x u_r}$, m^2/sec^2	σ_{u_x}/u_x × 100, %
0	0	275.0	0.7	5.7	2.1	2.7	1.0	4.1	5.8	6.6	4	0	14.3
0.594	0.127	275.4	0.4	-6.5	-2.4	3.5	1.3	3.8	5.6	8.9	7	2	20.5
1.102	0.236	276.4	0.4	-8.4	-3.0	-12.3	-4.5	3.6	5.5	6.3	2	3	13.8
1.613	0.345	277.2	0.3	-11.3	-4.1	-4.7	-1.7	3.8	5.2	5.7	-2	3	18.6
2.121	0.454	281.6	0	-12.7	-4.5	-2.0	-0.7	3.7	6.3	5.9	0	1	0
2.642	0.565	289.6	0.1	-11.5	-4.0	-4.5	-1.6	4.4	6.8	7.6	6	1	12.9
3.150	0.674	303.8	0.2	-11.3	-3.7	-2.9	-1.0	4.4	7.6	8.9	3	2	6.4
3.658	0.783	322.3	0.6	-6.2	-1.9	-5.4	-1.7	5.3	7.7	8.6	5	9	6.7
4.166	0.891	345.9	0.4	-6.8	-2.0	-4.7	-1.4	5.7	7.8	6.9	1	15	16.1
4.445	0.951	360.5	0.3	-11.2	-3.1	-1.1	-0.3	4.6	5.7	7.6	1	2	4.6

AXIAL STATION 3, AZIMUTHAL POSITION $\phi = 7.5$ deg

0	0	275.0	0.7	5.7	2.1	2.7	1.0	4.1	5.8	6.6	4	0	14.3
0.594	0.127	275.9	0.4	5.3	1.9	-8.0	-2.9	3.2	6.2	5.4	-2	-1	—
1.102	0.236	278.2	0.5	-0.8	-0.3	-6.5	-2.3	3.3	5.5	7.3	-15	0	—
1.613	0.345	280.4	0.2	-6.5	-2.3	-5.2	-1.9	3.6	5.8	5.7	-12	5	—
2.121	0.454	283.5	0.2	-10.2	-3.6	-6.4	-2.3	3.8	6.2	6.4	-4	3	—
2.642	0.565	294.2	1.0	-7.1	-2.4	-6.9	-2.3	4.2	8.4	8.9	-22	6	—
3.150	0.674	305.7	0.4	-12.1	-4.0	-7.2	-2.4	4.4	10.2	9.0	-3	1	—
3.658	0.783	324.0	0.5	-13.5	-4.2	-9.5	-2.9	5.1	9.6	8.7	-7	5	—
4.166	0.891	347.8	0.2	-11.4	-3.3	-0.4	-0.1	4.4	6.5	10.3	-28	0	—
4.445	0.951	362.0	0.1	-13.6	-3.8	-6.2	-1.7	4.0	5.3	—	-48	5	—

AXIAL STATION 3, AZIMUTHAL POSITION $\phi = 15$ deg

0	0	275.0	0.7	5.7	2.1	2.7	1.0	4.1	5.8	6.6	4	0	14.3
0.594	0.127	275.8	0.6	3.1	1.1	-12.9	-4.7	4.7	5.4	7.3	3	0	25.5
1.102	0.236	278.5	0.6	-3.4	-1.2	-6.8	-2.4	4.6	5.8	6.5	-5	0	29.8
1.613	0.345	280.3	0.5	-7.7	-2.7	-6.9	-2.5	4.9	5.9	7.5	2	6	19.6
2.121	0.454	284.1	0.7	-14.3	-5.0	-8.2	-2.9	5.0	7.1	7.4	-3	4	17.4
2.642	0.565	293.5	0.7	-19.0	-6.5	-9.0	-3.1	5.8	8.4	9.8	0	9	17.2
3.150	0.674	307.4	0.7	-23.9	-7.8	-6.0	-2.0	6.8	10.4	6.6	0	12	36.5
3.658	0.783	323.4	1.1	-29.7	-9.2	-2.4	-0.7	6.6	10.1	4.6	5	7	12.6
4.166	0.891	346.0	0.5	-26.3	-7.6	-6.9	-2.0	6.1	7.4	8.9	-1	6	25.1
4.445	0.951	359.9	0.6	-16.4	-4.6	-11.5	-3.2	5.7	6.1	12.7	-13	10	23.9

TABLE II
NOZZLE LDV VELOCITY DATA FOR COLD FLOW TEST CONDITIONS (CONTINUED)
$T_{op} = 289°K$; $T_{os} = 289°K$

AXIAL STATION 4, AZIMUTHAL POSITION $\phi = 7.5$ deg

r, cm	R	U_x, m/sec	$\sigma_{U_x}/U_x \times 100$, %	U_r, m/sec	$U_r/Ux \times 100$, %	u_x, m/sec	u_r, m/sec	$\overline{u_x u_r}$, m^2/sec^2
0	0	245.0	0	3.2	1.3	4.5	6.6	3
0.594	0.127	245.0	0.2	-1.4	-0.6	4.2	6.3	7
1.102	0.236	248.1	0	-6.2	-2.5	4.0	5.6	-4
1.613	0.345	249.4	0.1	-12.7	-5.1	4.0	5.8	7
2.121	0.454	250.0	0.1	-17.7	-7.1	4.5	6.2	5
2.642	0.565	253.3	0.1	-20.5	-8.1	5.1	8.0	5
3.150	0.674	259.1	0.3	-22.4	-8.6	4.1	8.9	1
3.658	0.783	266.2	0.3	-32.0	-12.0	5.9	7.8	3
4.166	0.891	274.2	0.1	-44.9	-16.4	5.4	6.8	4
4.445	0.951	279.6	0.8	-58.6	-20.9	6.5	5.0	-2

TABLE III
NOZZLE TOTAL PRESSURE DISTRIBUTION FOR HOT AND COLD FLOW TEST CONDITIONS: P_T/P_{op}[a]

AXIAL STATION 1[b]

RADIAL POSITION, r, cm[c]	AZIMUTHAL POSITION									
	ϕ = 0 deg		ϕ = 3.75 deg		ϕ = 7.5 deg		ϕ = 11.3 deg		ϕ = 15 deg	
	COLD	HOT	COLD	HOT	COLD	HOT	COLD	HOT	COLD	HOT
0.079	0.975	0.970	0.977	0.973	0.978	0.974	0.973	0.970	0.971	0.967
0.238	0.981	0.978	0.978	0.975	0.983	0.978	0.976	0.974	0.980	0.976
0.397	0.981	0.979	0.981	0.979	0.986	0.981	0.962	0.967	0.973	0.966
0.556	0.980	0.977	0.983	0.979	0.986	0.983	0.948	0.948	0.947	0.947
0.715	0.982	0.981	0.986	0.980	0.978	0.985	0.948	0.946	0.947	0.947
0.873	0.985	0.980	0.986	0.983	0.979	0.986	0.949	0.948	0.948	0.948
1.032	0.986	0.984	0.987	0.984	0.970	0.985	0.949	0.948	0.948	0.947
1.191	0.988	0.983	0.988	0.983	0.974	0.986	0.952	0.954	0.951	0.949
1.350	0.989	0.986	0.988	0.986	0.980	0.986	0.954	0.951	0.953	0.954
1.508	0.989	0.987	0.989	0.987	0.982	0.985	0.954	0.954	0.954	0.953
1.667	0.990	0.987	0.989	0.988	0.983	0.986	0.955	0.957	0.954	0.953
1.826	0.991	0.987	0.990	0.988	0.982	0.986	0.955	0.955	0.955	0.955
1.985	0.992	0.989	0.990	0.990	0.982	0.986	0.955	0.954	0.954	0.958
2.143	0.992	0.992	0.990	0.988	0.983	0.985	0.955	0.955	0.955	0.955
2.302	0.993	0.990	0.990	0.991	0.983	0.986	0.956	0.956	0.955	0.957
2.461	0.992	0.989	0.989	0.991	0.979	0.986	0.956	0.957	0.955	0.954
2.620	0.992	0.992	0.989	0.989	0.978	0.982	0.956	0.956	0.958	0.957
2.778	0.992	0.989	0.989	0.990	0.978	0.980	0.957	0.956	0.956	0.958
2.937	0.990	0.988	0.988	0.986	0.973	0.974	0.957	0.955	0.955	0.953
3.096	0.989	0.987	0.989	0.989	0.967	0.967	0.957	0.956	0.955	0.954
3.255	0.989	0.985	0.989	0.988	0.962	0.959	0.957	0.956	0.955	0.955
3.413	0.988	0.984	0.989	0.989	0.957	0.957	0.957	0.956	0.956	0.959
3.572	0.988	0.986	0.989	0.990	0.954	0.958	0.957	0.954	0.955	0.954
3.731	0.989	0.987	0.989	0.990	0.955	0.955	0.956	0.954	0.955	0.952
3.890	0.990	0.984	0.988	0.988	0.955	0.956	0.957	0.955	0.953	0.952
4.048	0.990	0.986	0.985	0.985	0.955	0.956	0.956	0.953	0.954	0.955
4.207	0.989	0.985	0.981	0.981	0.955	0.956	0.956	0.953	0.952	0.954
4.366	0.988	0.982	0.976	0.980	0.954	0.955	0.955	0.953	0.952	0.950
4.525	0.986	0.978	0.973	0.975	0.954	0.955	0.954	0.952	0.952	0.950
4.683	0.983	0.974	0.969	0.968	0.953	0.953	0.952	0.950	0.950	0.949
4.842	0.981	0.970	0.959	0.954	0.952	0.954	0.952	0.950	0.949	0.949
5.001	0.971	0.953	0.953	0.949	0.951	0.953	0.951	0.951	0.948	0.948
5.160	0.955	0.951	0.951	0.951	0.950	0.952	0.950	0.947	0.947	0.948
5.318	0.951	—	0.950	0.947	0.949	0.951	0.950	0.947	0.948	0.946
5.414	0.950	—	0.949	—	—	0.951	0.950	—	0.946	0.944

(a) TABLE ENTRIES ARE VALUES OF THE RATIO, P_T/P_{op}, WHERE P_T = TOTAL PRESSURE INDICATED BY THE TRAVERSED TOTAL PRESSURE PROBE AND P_{op} = PRIMARY STREAM TOTAL PRESSURE MEASURED UPSTREAM OF THE NOZZLE BY THE PROBE USED TO SET PRIMARY OPERATING PRESSURE; THE REFERENCE VALUE OF P_{op} WAS 26.2×10^4 N/m^2 (38.1 psia).

(b) THE AXIAL LOCATION OF STATION 1 TOTAL PRESSURE MEASUREMENTS FOR AZIMUTHAL POSITIONS ϕ = 0, 3.75, 11.3 AND 15 deg WAS 0.63 cm DOWNSTREAM OF THE AXIAL STATION 1 LDV MEASUREMENT PLANE SHOWN IN FIGURE 2; FOR AZIMUTHAL POSITION ϕ = 7.5 deg, THE TOTAL PRESSURE MEASUREMENTS WERE TAKEN IN THE LDV MEASUREMENT PLANE (NO DOWNSTREAM OFFSET).

(c) RADIAL MEASUREMENT LOCATIONS FOR AXIAL STATIONS 2 AND 3 ARE GIVEN IN TERMS OF THE RADIAL DISTANCE FROM THE NOZZLE CENTERLINE, r. RADIAL MEASUREMENT LOCATIONS FOR AXIAL STATION 1 ARE GIVEN IN TERMS OF THE RADIAL POSITION RELATIVE TO THE NOZZLE PLUG, r; THE RADIAL LOCATION OF THE PLUG SURFACE, WHICH VARIES WITH THE AXIAL LOCATIONS OF THE TRAVERSE AND THE NOZZLE OPERATING TEMPERATURE, ARE GIVEN BELOW:

PLUG RADIUS, cm
(r = 0 LOCATION)

AZIMUTHAL TRAVERSE	COLD FLOW	HOT FLOW
ϕ = 7.5 deg	2.977	3.128
ϕ = 0, 3.75, 11.3 AND 15 deg	2.723	2.875

TABLE III (CONTINUED)
NOZZLE TOTAL PRESSURE DISTRIBUTIONS FOR HOT AND COLD FLOW TEST CONDITIONS: P_T/P_{op}[a]

AXIAL STATION 2

RADIAL POSITION, r, cm	AZIMUTHAL POSITION					
	ϕ = 0 deg		ϕ = 7.5 deg		ϕ = 15 deg	
	COLD	HOT	COLD	HOT	COLD	HOT
0	0.967	0.962	0.967	0.962	0.967	0.962
0.318	0.964	0.958	0.964	0.960	0.969	0.966
0.635	0.967	0.959	0.964	0.963	0.974	0.969
0.953	0.972	0.964	0.969	0.967	0.979	0.973
1.270	0.974	0.971	0.973	0.969	0.976	0.974
1.588	0.972	0.968	0.974	0.970	0.972	0.970
1.905	0.968	0.964	0.970	0.967	0.966	0.968
2.223	0.965	0.963	0.966	0.964	0.961	0.964
2.540	0.963	0.961	0.963	0.961	0.958	0.959
2.858	0.962	0.959	0.961	0.961	0.958	0.961
3.175	0.962	0.959	0.962	0.959	0.958	0.959
3.493	0.963	0.961	0.960	0.962	0.958	0.961
3.810	0.966	0.961	0.959	0.963	0.959	0.960
4.128	0.970	0.965	0.959	0.963	0.959	0.961
4.445	0.976	0.970	0.960	0.966	0.958	0.961
4.763	0.982	0.979	0.961	0.968	0.958	0.958
5.080	0.986	0.981	0.967	0.967	0.957	0.959
5.400	0.987	0.988	0.969	0.970	0.955	0.959
5.715	0.987	0.987	0.968	0.967	0.953	0.956
6.033	0.985	0.987	0.965	0.966	0.951	0.955
6.350	0.984	0.986	0.962	0.966	0.952	0.955
6.668	0.983	0.984	0.958	0.962	0.952	0.955
6.985	0.983	0.982	0.956	0.961	0.953	0.958
7.303	0.984	0.983	0.958	0.967	0.952	0.956
7.549	0.981	0.980	0.961	0.971	0.940	0.945

AXIAL STATION 3[d]

0	0.969	0.965	0.969	0.965	0.969	0.965
0.318	0.968	0.965	0.969	0.965	0.967	0.963
0.635	0.973	0.968	0.973	0.964	0.972	0.968
0.953	0.973	0.968	0.973	0.967	0.975	0.964
1.270	0.970	0.966	0.969	0.966	0.971	0.963
1.588	0.964	0.964	0.966	0.966	0.966	0.958
1.905	0.962	0.962	0.963	0.962	0.963	0.959
2.223	0.961	0.960	0.963	0.962	0.964	0.960
2.540	0.961	0.960	0.965	0.961	0.965	0.963
2.858	0.963	0.962	0.966	0.964	0.967	0.962
3.175	0.964	0.963	0.966	0.960	0.967	0.965
3.493	0.966	0.962	0.968	0.966	0.968	0.964
3.810	0.969	0.965	0.970	0.968	0.971	0.965
4.128	0.972	0.968	0.972	0.969	0.972	0.966
4.445	0.974	0.969	0.976	0.969	0.970	0.965
4.547	—	—	—	—	0.960	—
4.636	—	—	—	0.902	0.831	0.875
4.763	0.386	—	—	—	—	—

(d) TABULATED TOTAL PRESSURES FOR AXIAL STATION 3 REPRESENT "AS MEASURED" VALUES WHICH HAVE NOT BEEN CORRECTED FOR TOTAL PRESSURE LOSS DUE TO THE PROBE BOW SHOCK WAVE AT SUPERSONIC VELOCITIES.

TABLE IV
NOZZLE TOTAL TEMPERATURE DISTRIBUTION FOR HOT FLOW TEST CONDITION; T_T/Top[a]

AXIAL STATION 1[b]

RADIAL POSITION, r, cm[c]	AZIMUTHAL POSITION				
	ϕ = 0 deg	ϕ = 3.75 deg	ϕ = 7.5 deg	ϕ = 11.3 deg	ϕ = 15 deg
3.099	0.998	0.998	0.997	0.936	0.936
3.258	0.997	0.983	0.999	0.869	0.880
3.416	0.997	0.977	0.990	0.863	0.883
3.575	1.000	0.973	0.971	0.490	0.490
3.734	1.000	0.979	0.975	0.480	0.481
3.893	1.000	0.986	0.974	0.471	0.475
4.052	1.000	0.992	0.981	0.452	0.457
4.210	1.000	0.988	0.986	0.435	0.439
4.369	1.000	0.988	0.988	0.426	0.428
4.528	1.000	0.993	0.984	0.421	0.421
4.687	1.000	0.990	0.982	0.417	0.417
4.846	0.999	0.989	0.975	0.418	0.414
5.004	1.000	0.982	0.975	0.412	0.413
5.163	1.000	0.989	0.971	0.411	0.411
5.322	0.997	0.987	0.964	0.411	0.410
5.481	0.994	0.985	0.961	0.411	0.409
5.640	0.990	0.984	0.951	0.409	0.403
5.798	0.989	0.981	0.932	0.409	0.405
5.957	0.983	0.979	0.900	0.407	0.406
6.116	0.981	0.978	0.865	0.406	0.405
6.275	0.982	0.979	0.816	0.405	0.404
6.434	0.984	0.975	0.754	0.406	0.402
6.592	0.977	0.970	0.672	0.405	0.401
6.751	0.976	0.964	0.557	0.404	0.400
6.910	0.972	0.955	0.454	0.403	0.400
7.069	0.963	0.936	0.417	0.403	0.402
7.228	0.952	0.912	0.406	0.402	0.400
7.386	0.922	0.878	0.403	0.401	0.400
7.545	0.862	0.812	0.402	0.402	0.401
7.704	0.713	0.670	0.398	0.402	0.400
7.863	0.479	0.459	0.401	0.402	0.399
8.022	0.403	0.403	0.405	0.401	0.400
8.179	0.404	0.400	0.401	0.401	0.400
8.291	—	—	—	0.405	—

TABLE IV (CONTINUED)
NOZZLE TOTAL TEMPERATURE DISTRIBUTION FOR HOT FLOW TEST CONDITION; T_T/Top[a]

AXIAL STATION 2

RADIAL POSITION, cm	AZIMUTHAL POSITION				
	$\phi = 0$ deg	$\phi = 3.75$ deg	$\phi = 7.5$ deg	$\phi = 11.3$ deg	$\phi = 15$ deg
0	0.885				
0.318	0.877	0.887	0.901	0.914	0.903
0.635	0.890	0.893	0.905	0.915	0.909
0.953	0.884	0.883	0.900	0.891	0.894
1.270	0.844	0.846	0.868	0.834	0.852
1.588	0.775	0.780	0.811	0.774	0.792
1.905	0.712	0.718	0.754	0.717	0.731
2.223	0.664	0.669	0.705	0.669	0.676
2.540	0.636	0.637	0.669	0.627	0.629
2.858	0.626	0.625	0.648	0.603	0.593
3.175	0.633	0.629	0.641	0.601	0.583
3.493	0.650	0.649	0.651	0.613	0.583
3.810	0.678	0.676	0.670	0.633	0.611
4.128	0.715	0.711	0.694	0.652	0.623
4.445	0.759	0.751	0.717	0.662	0.634
4.763	0.798	0.794	0.737	0.667	0.632
5.080	0.833	0.822	0.752	0.664	0.619
5.400	0.849	0.856	0.757	0.649	0.590
5.715	0.843	0.860	0.757	0.633	0.559
6.033	0.829	0.855	0.749	0.606	0.522
6.350	0.842	0.842	0.738	0.585	0.496
6.668	0.860	0.840	0.728	0.564	0.482
6.985	0.886	0.841	0.725	0.558	0.481
7.303	0.879	0.836	0.734	0.568	0.484
7.475	0.832	0.814	0.739	0.582	0.477

TABLE IV
NOZZLE TOTAL TEMPERATURE DISTRIBUTION FOR HOT FLOW TEST CONDITION; T_T/Top[a]

AXIAL STATIONS 3 AND 4

RADIAL POSITION, cm	STATION 3 AZIMUTHAL POSITION			STATION 4 AZIMUTHAL POSITION
	ϕ = 0 deg	ϕ = 7.5 deg	ϕ = 15 deg	ϕ = 7.5 deg
0	0.779	0.804	0.788	0.813
0.159	—	—	—	0.813
0.318	0.792	0.805	0.799	0.811
0.476	—	—	—	0.802
0.635	0.787	0.793	0.786	0.794
0.794	—	—	—	0.783
0.953	0.767	0.766	0.763	0.772
1.111	—	—	—	0.758
1.270	0.731	0.737	0.734	0.743
1.429	—	—	—	0.727
1.588	0.686	0.711	0.700	0.713
1.746	—	—	—	0.704
1.905	0.659	0.693	0.678	0.693
2.064	—	—	—	0.688
2.223	0.655	0.686	0.670	0.688
2.381	—	—	—	0.688
2.540	0.658	0.685	0.675	0.690
2.699	—	—	—	0.690
2.858	0.666	0.693	0.677	0.698
3.016	—	—	—	0.703
3.175	0.677	0.700	0.684	0.705
3.334	—	—	—	0.707
3.493	0.685	0.709	0.690	0.714
3.651	—	—	—	0.719
3.810	0.694	0.722	0.697	0.724
3.969	—	—	—	0.730
4.128	0.710	0.735	0.706	0.735
4.286	—	—	—	0.740
4.445	0.731	0.742	0.714	0.744
4.636	0.723	—	0.695	—
4.783	0.513	0.486	0.475	—

FOOTNOTES FOR TABLE IV

(a) TABLE ENTRIES ARE VALUES OF THE RATIO, T_T/T_{op}, WHERE T_T = TOTAL TEMPERATURE INDICATED BY THE TRAVERSED TOTAL TEMPERATURE PROBE AND T_{op} = PRIMARY STREAM TOTAL TEMPERATURE MEASURED IN THE MIXER LOBE BY THE PROBE USED TO SET PRIMARY OPERATING TEMPERATURE, THE REFERENCE VALUE OF T_{op} WAS 755°K (1360°R).

(b) THE AXIAL LOCATION OF STATION 1 TOTAL TEMPERATURE MEASUREMENTS WAS 0.47 cm DOWNSTREAM OF THE AXIAL STATION 1 LDV MEASUREMENT PLANE SHOWN IN FIGURE 2.

(c) RADIAL MEASUREMENT LOCATIONS ARE GIVEN IN TERMS OF THE RADIAL DISTANCE FROM THE NOZZLE CENTERLINE, r. THE RADIAL LOCATION OF THE NOZZLE PLUG SURFACE AT AXIAL STATION 1 IN THE PLANE OF THE TEMPERATURE MEASUREMENTS WAS r = 2.946 cm FOR HOT FLOW TEST CONDITIONS

TABLE V
NOZZLE STATIC PRESSURES AND SURFACE BOUNDARY LAYER DATA

STATIC PRESSURES; P_s/P_{op}[a]

AXIAL STATION 1		AXIAL STATION 2		
NOZZLE WALL		NOZZLE WALL		ON-AXIS
COLD	HOT	COLD	HOT	COLD
0.941	0.941	0.936	0.939	0.935

AXIAL STATION 1 OUTER WALL BOUNDARY LAYER DATA (COLD FLOW; AXIMUTHAL POSITION $\phi = 7.5$ deg)

DISTANCE FROM WALL, cm	P_T/P_{op}[b]	CALCULATED VELOCITY, m/sec[c]	LDV TOTAL VELOCITY, m/sec
0.083	0.944	22.3	—
0.240	0.946	30.9	—
0.401	0.948	34.3	—
0.493	0.949	37.5	—
0.653	0.950	39.8	37.3
0.810	0.951	41.9	—
0.970	0.952	44.0	—
1.128	0.953	45.9	—
1.288	0.954	47.8	48.2
1.445	0.954	47.8	—
1.605	0.955	49.6	—
1.763	0.955	49.6	—
1.923	0.955	49.6	53.3

(a) TABLE ENTRIES ARE VALUES OF THE RATIO P_s/P_{op}, WHERE P_s = MEASURED STATIC PRESSURE AND P_{op} = PRIMARY STREAM TOTAL PRESSURE MEASURED UPSTREAM OF THE NOZZLE BY PROBE USED TO SET PRIMARY OPERATING PRESSURE; THE REFERENCE VALUE OF P_{op} WAS 26.3×10^4 N/m^2 (38.1 psia).

(b) COLUMN GIVES THE RATIO, P_T/P_{op}, WHERE P_T = TRAVERSED PROBE TOTAL PRESSURE.

(c) VELOCITIES CALCULATED AT 306°K USING LISTED PROBE TOTAL PRESSURES AND A WALL STATIC PRESSURE OF 0.941 P_{op}.

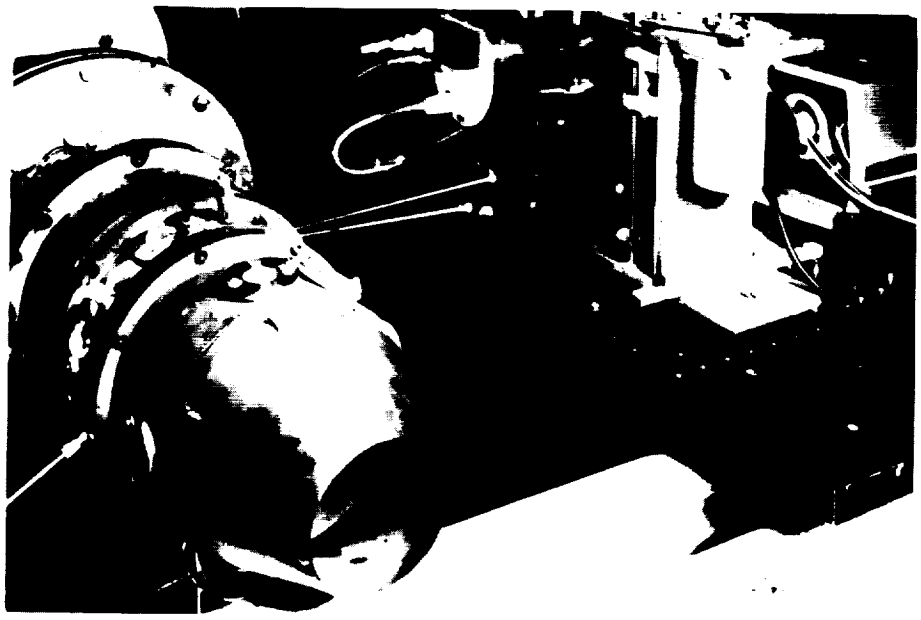

a) EXHAUST NOZZLE INSTALLED

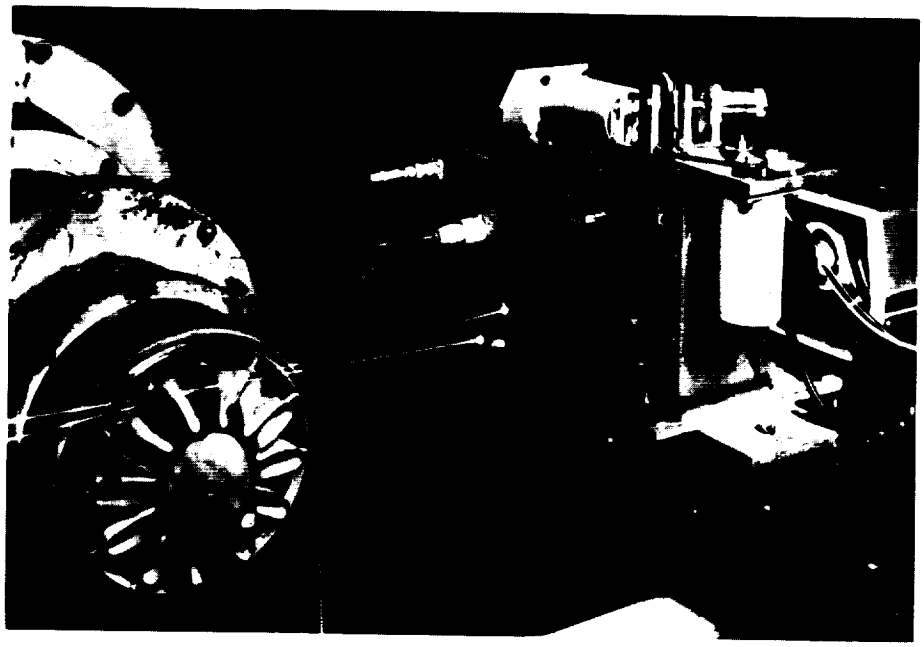

b) EXHAUST NOZZLE REMOVED

Figure 1. Model Mixer Test Arrangement

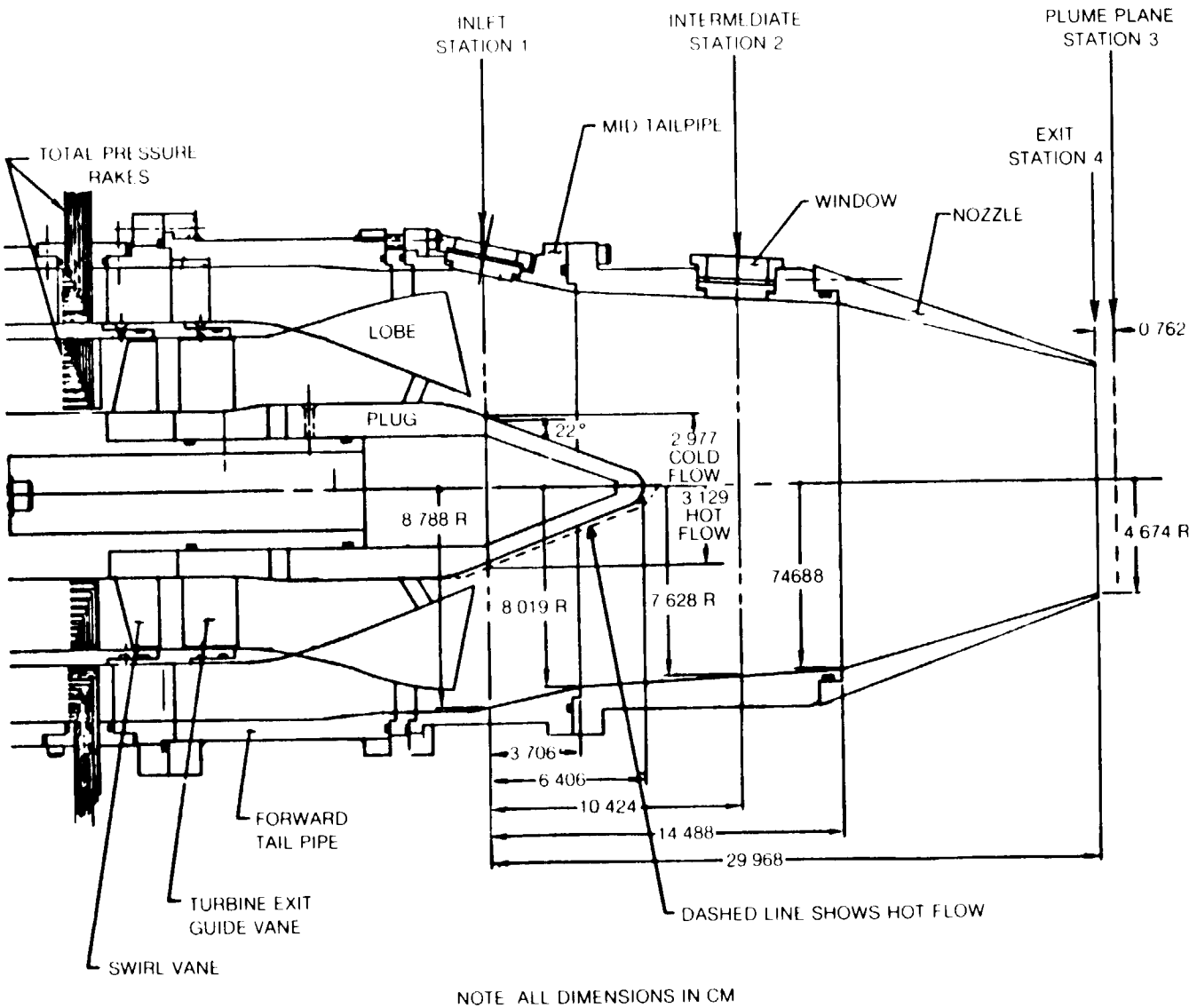

Figure 2 — Model Mixer Nozzle

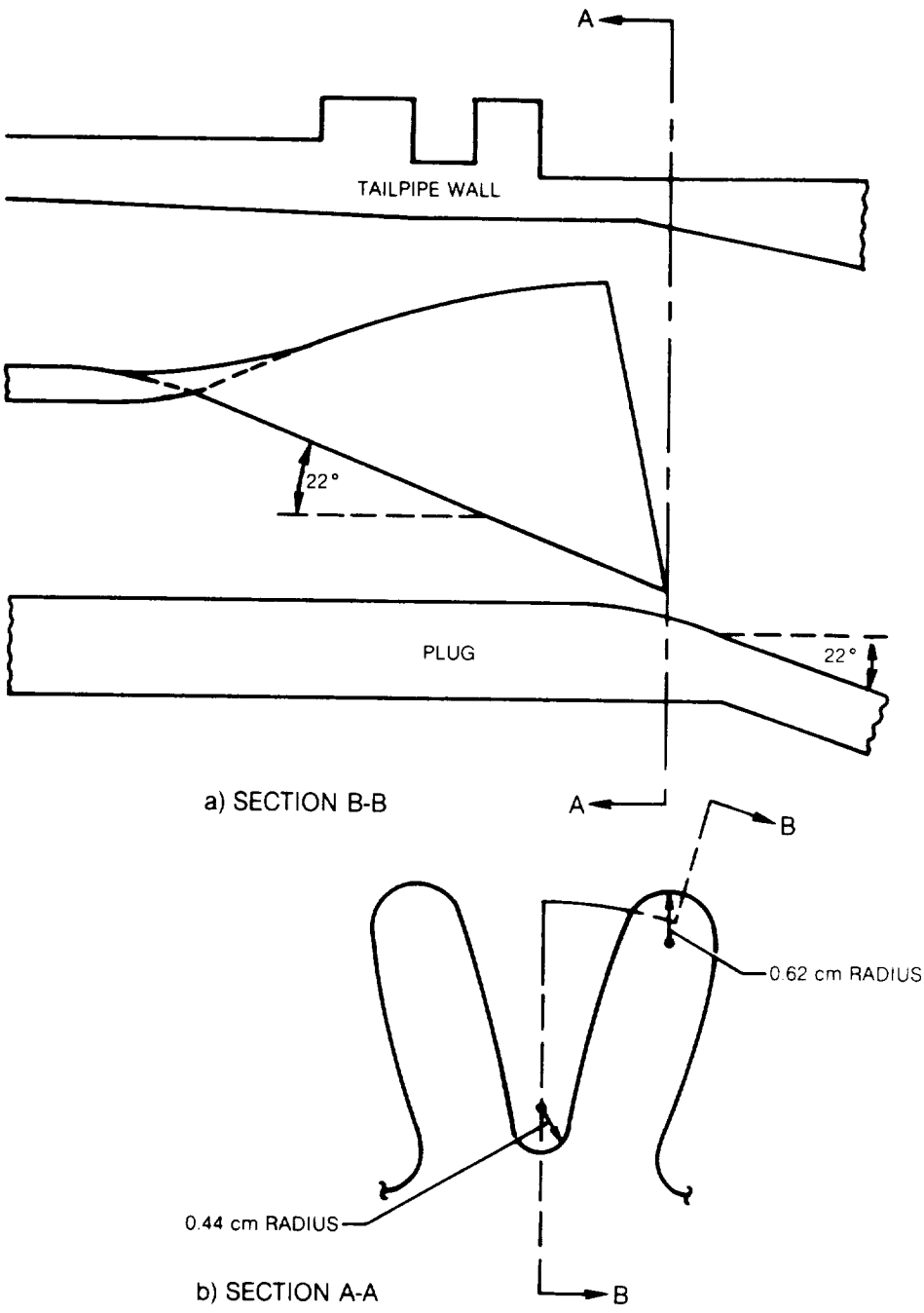

Figure 3 — Mixer Lobe Geometry Definition

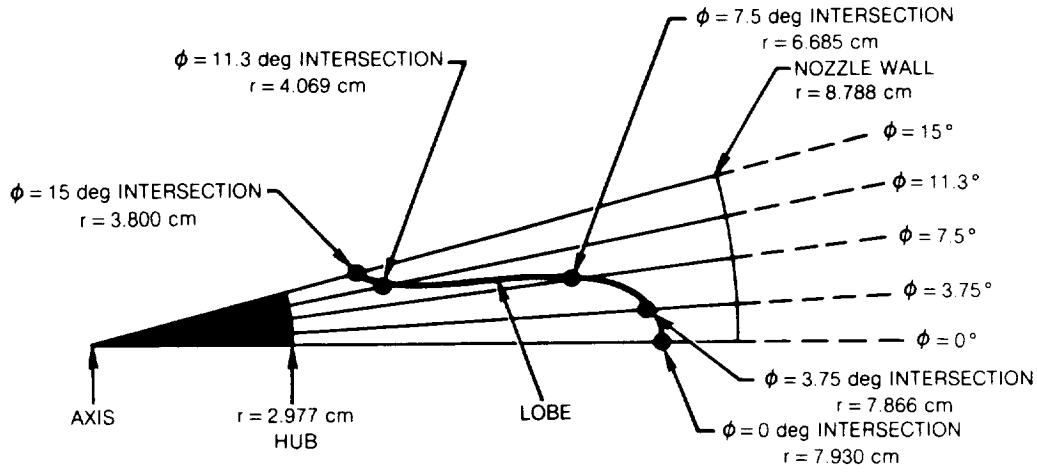

a) PROJECTION OF INTERSECTION POINTS OF RADIAL LDV TRAVERSE LINES AND LOBE ON A PLANE PERPENDICULAR TO NOZZLE AXIS

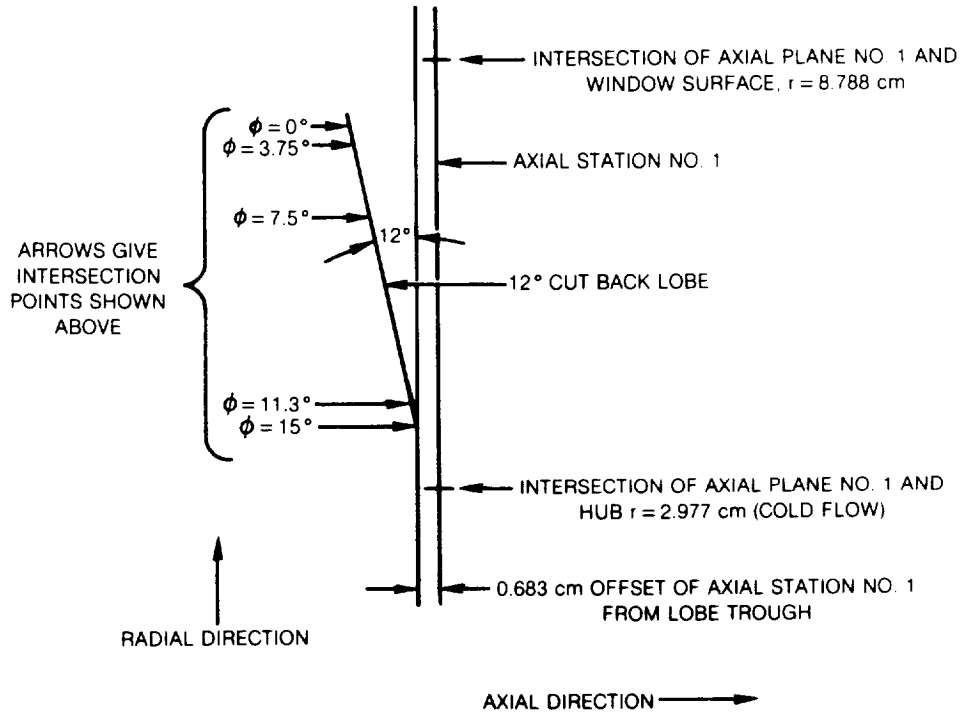

b) INTERSECTION POINTS OF PART (a) ABOVE SHOWN IN SIDE ELEVATION

Figure 3 — Concluded

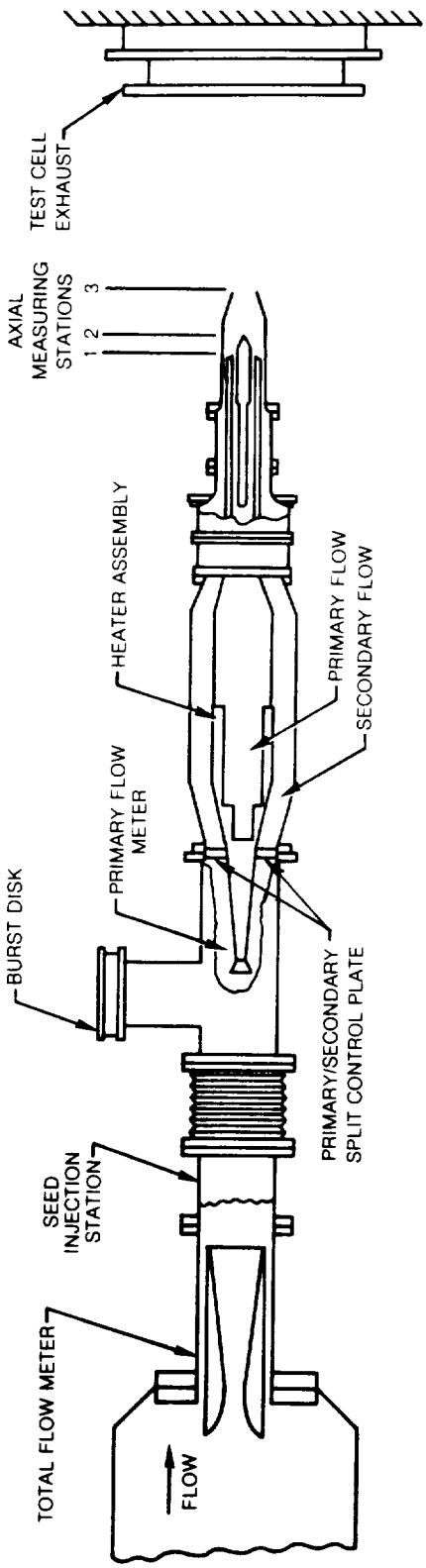

Figure 4 — Overall Test Rig Arrangement

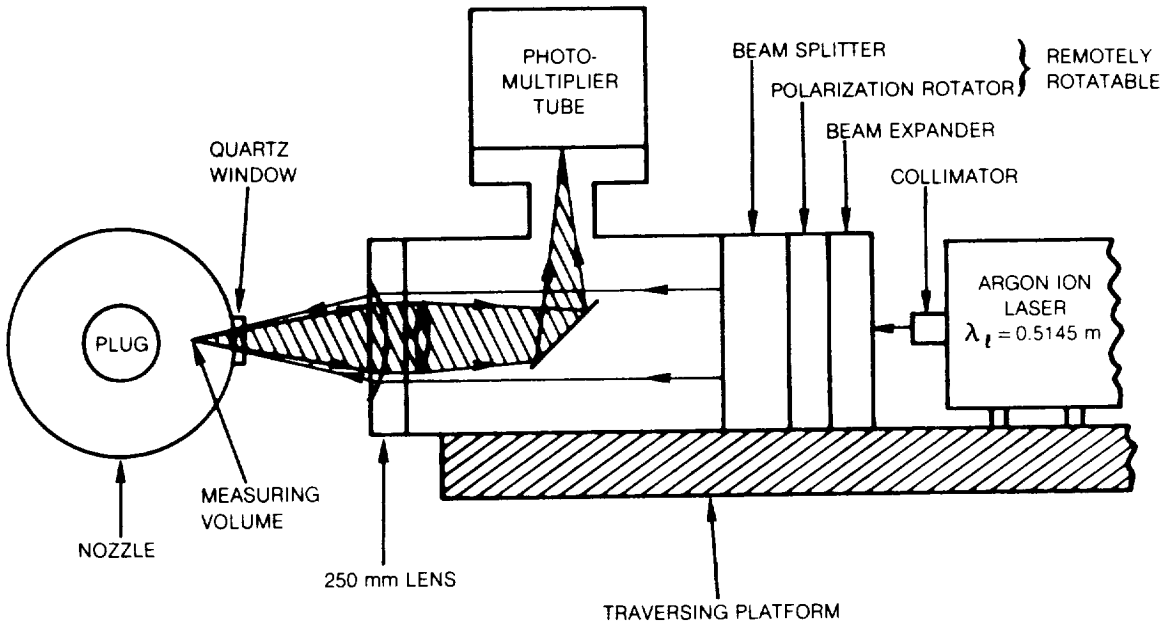

a) BACKSCATTER COLLECTION SYSTEM (AXIAL STATIONS 1 AND 2)

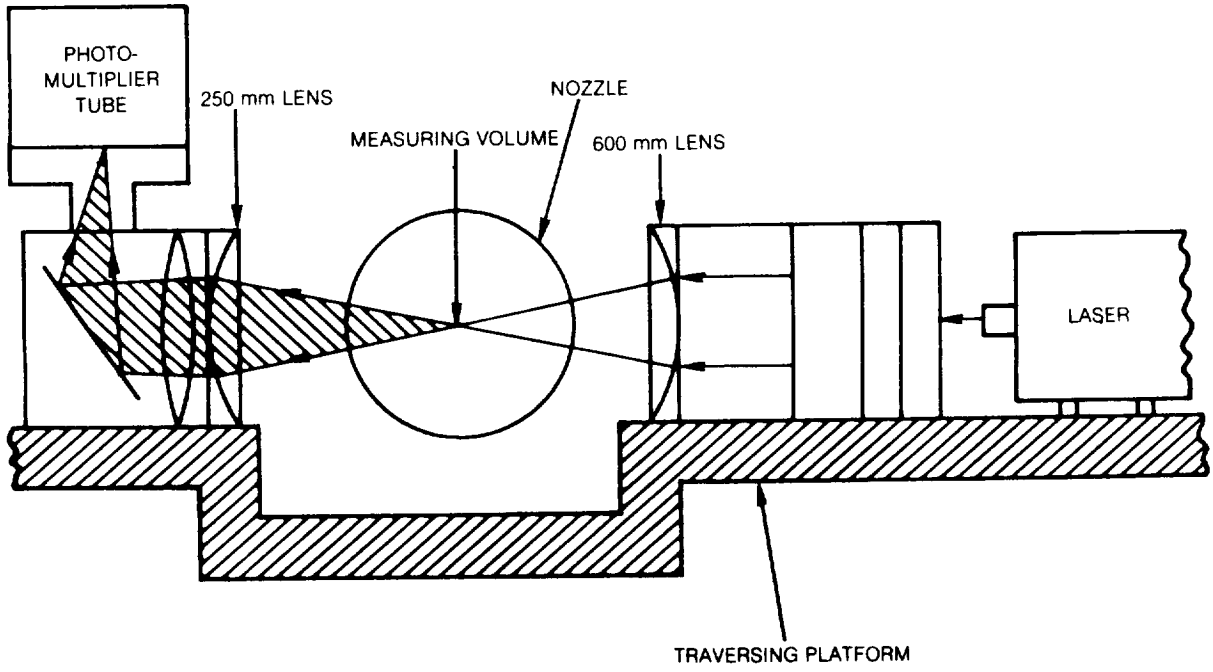

b) FORWARD SCATTER COLLECTION SYSTEM (AXIAL STATIONS 3 AND 4)

Figure 5 — LDV OPTICAL ARRANGEMENT

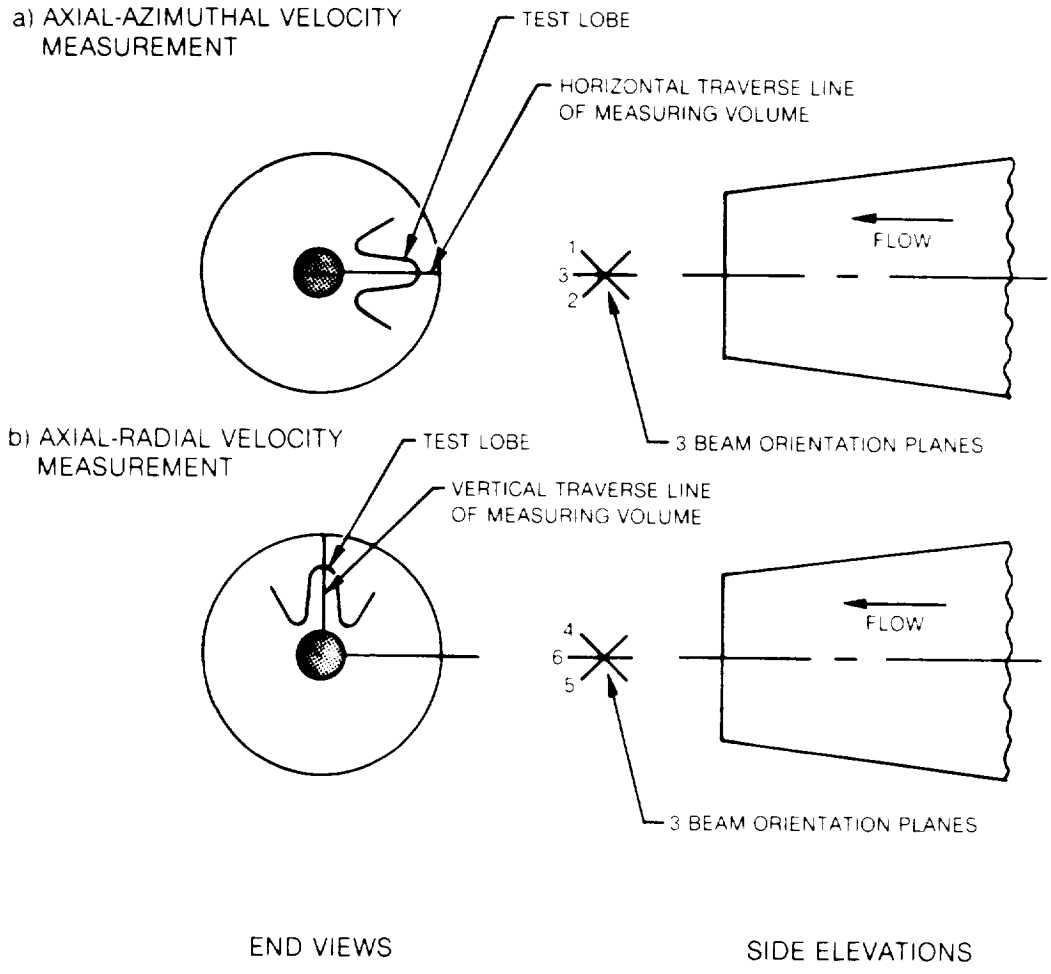

Figure 6 — Schematic of LDV Beam Orientations for Velocity Measurements at Azimuthal Position $\phi = 0$

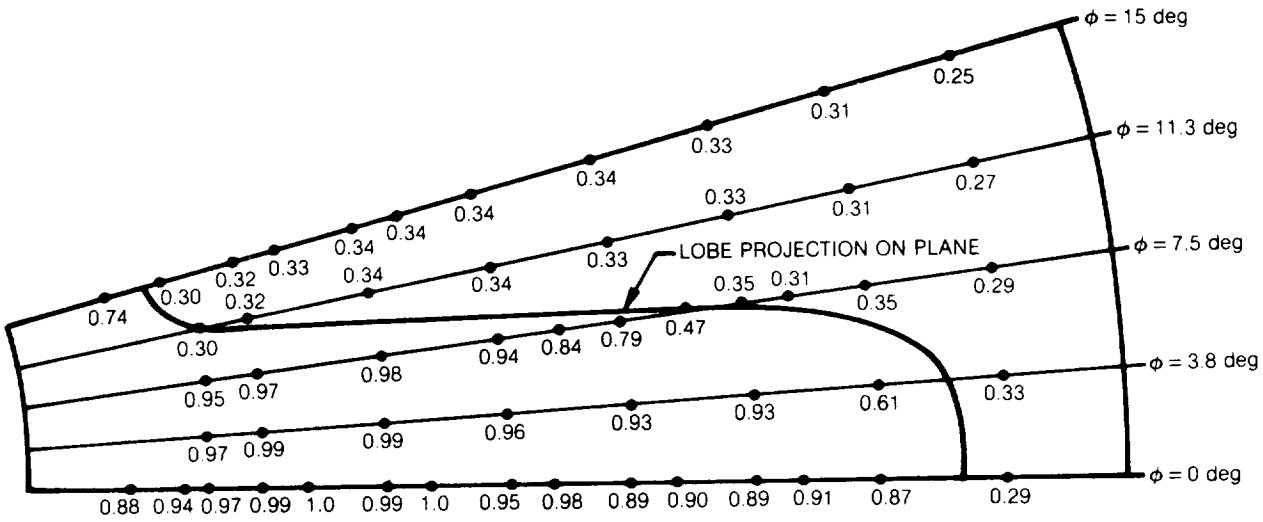

(a) HOT FLOW Ux/U_{REF} DISTRIBUTION, U_{REF} = 163.6 m/sec

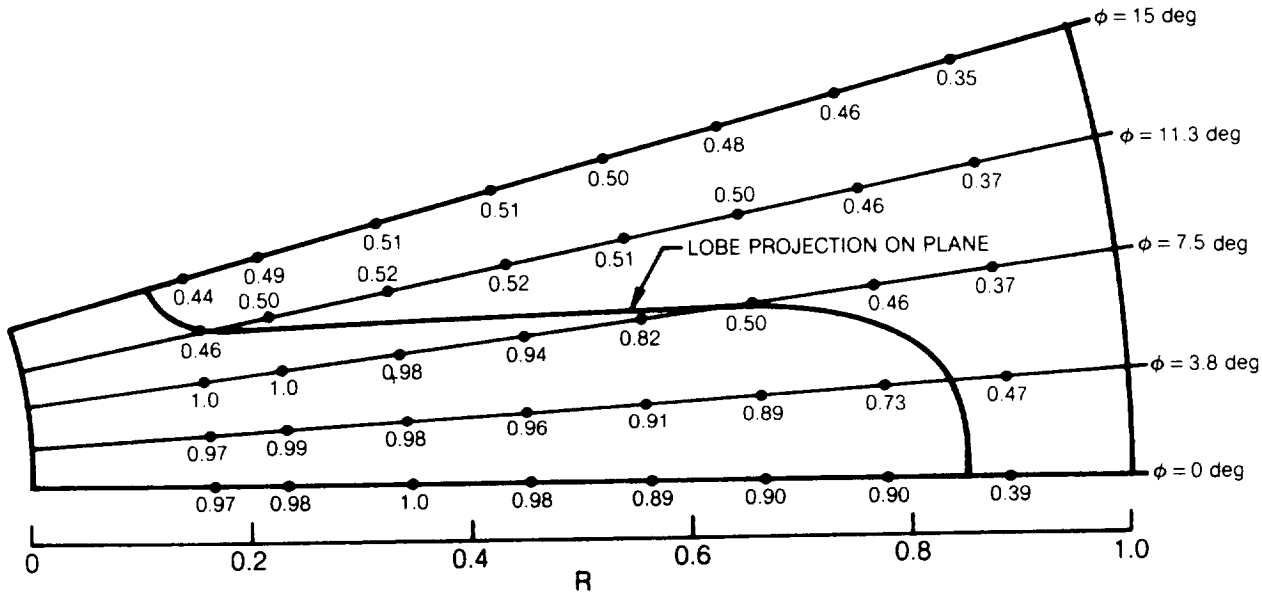

(b) COLD FLOW Ux/U_{REF} DISTRIBUTION, U_{REF} = 104.6 m/sec

Figure 7 — Axial Velocity Distributions for Hot and Cold Flow Test Conditions at Inlet Station 1

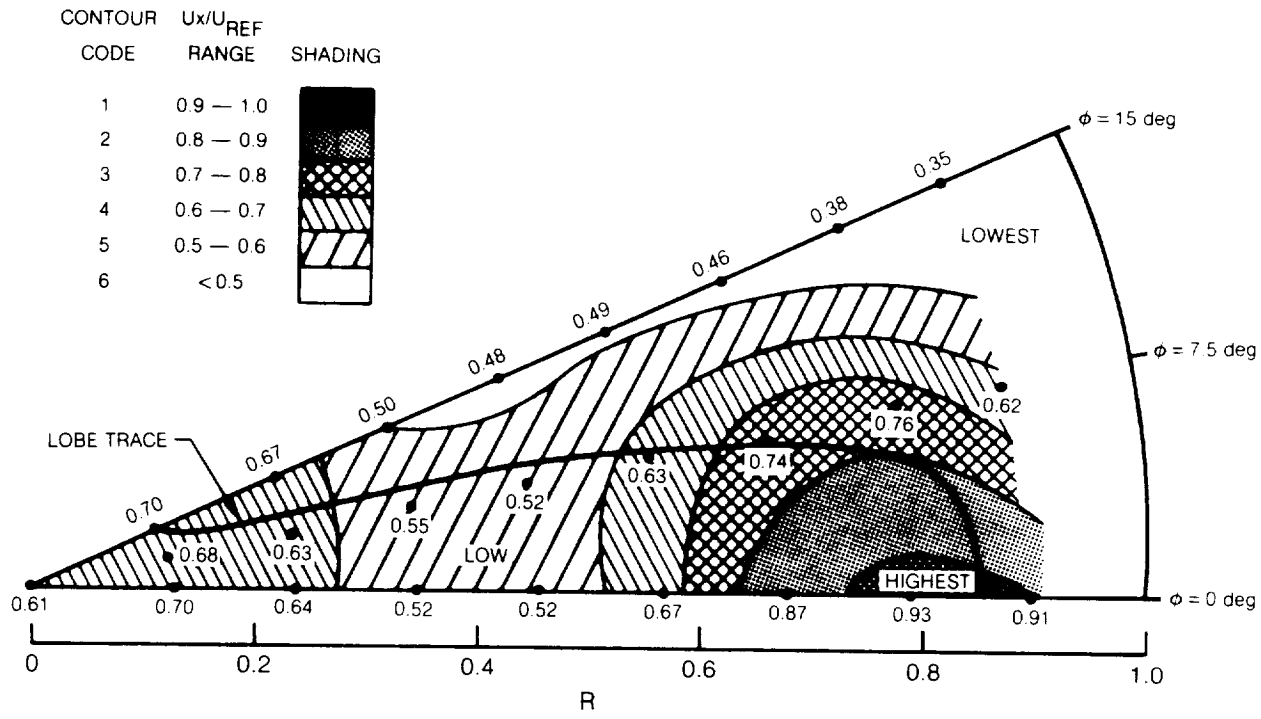

(a) HOT FLOW Ux/U_{REF} DISTRIBUTION, U_{REF} = 163.6 m/sec

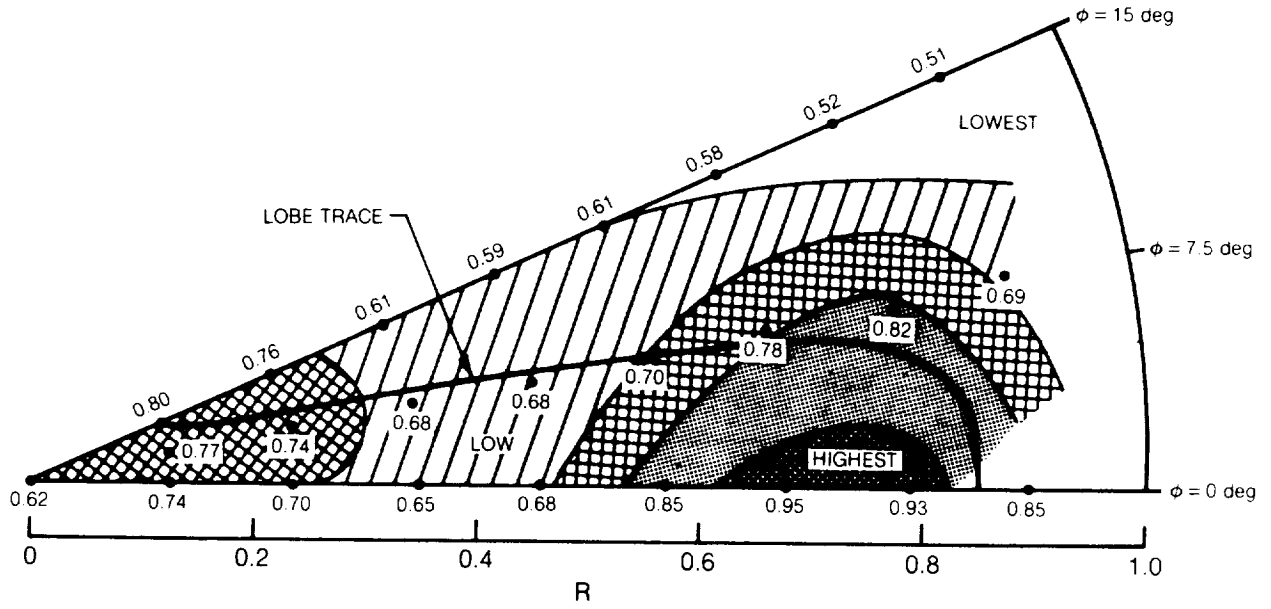

(b) COLD FLOW Ux/U_{REF} DISTRIBUTION, U_{REF} = 104.6 m/sec

Figure 8 — Axial Velocity Distributions for Hot and Cold Flow Test Conditions at Intermediate Station 2

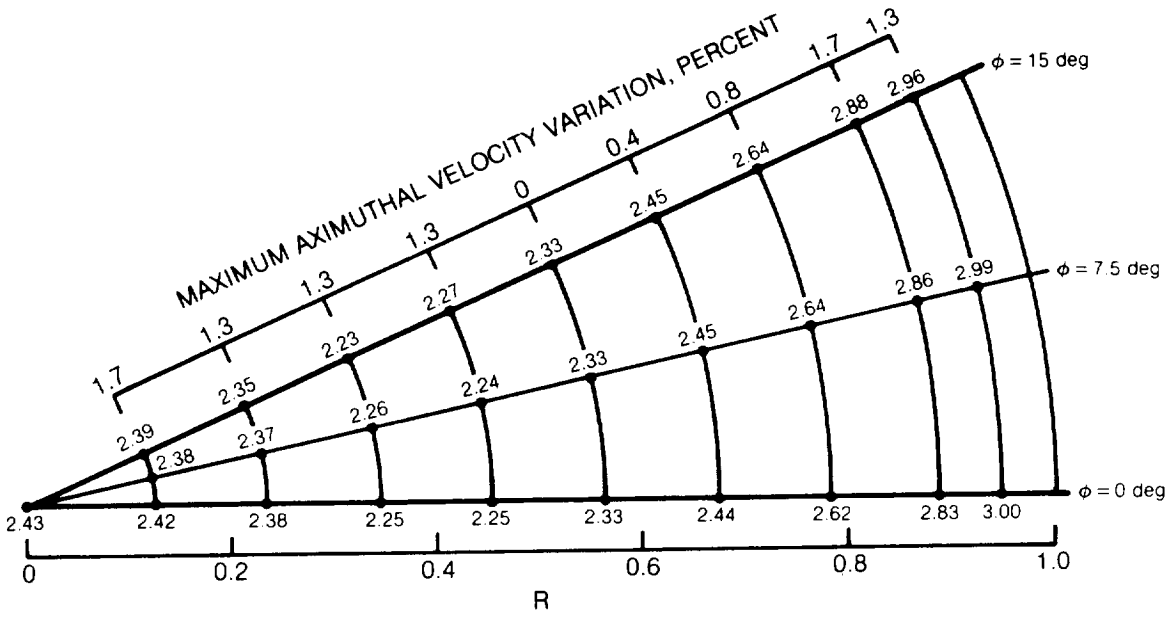

(a) HOT FLOW Ux/U_{REF} DISTRIBUTION, U_{REF} = 163.7 m/sec

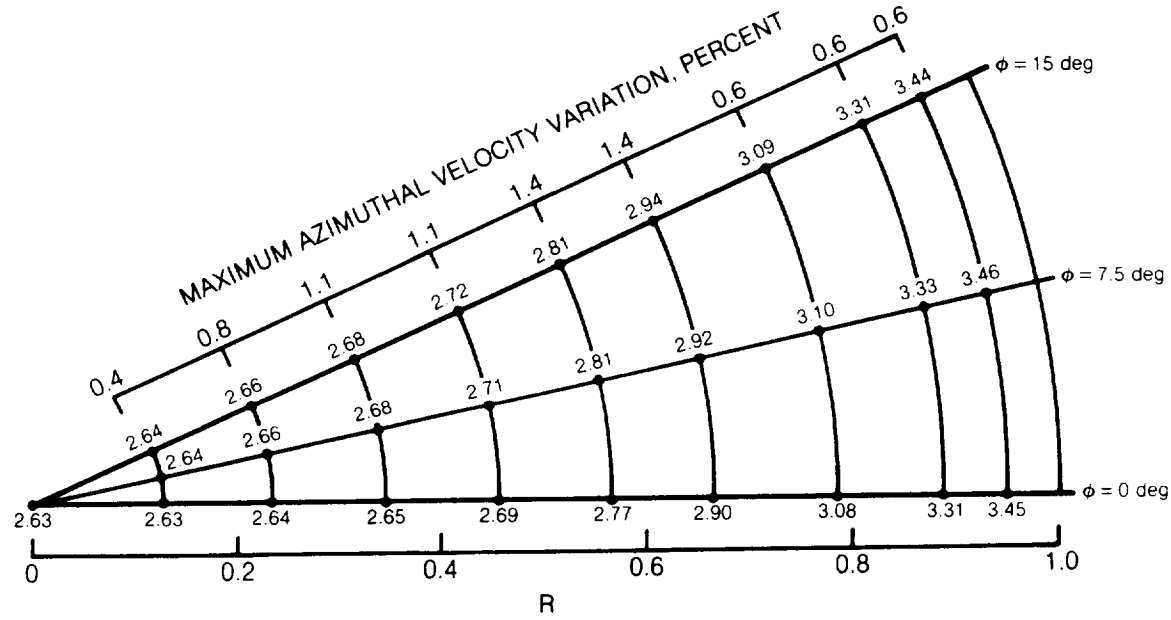

(b) COLD FLOW Ux/U_{REF} DISTRIBUTION, U_{REF} = 104.6 m/sec

Figure 9 — Axial Velocity Distributions for Hot and Cold Flow Test Conditions at Plume Plane Station 3

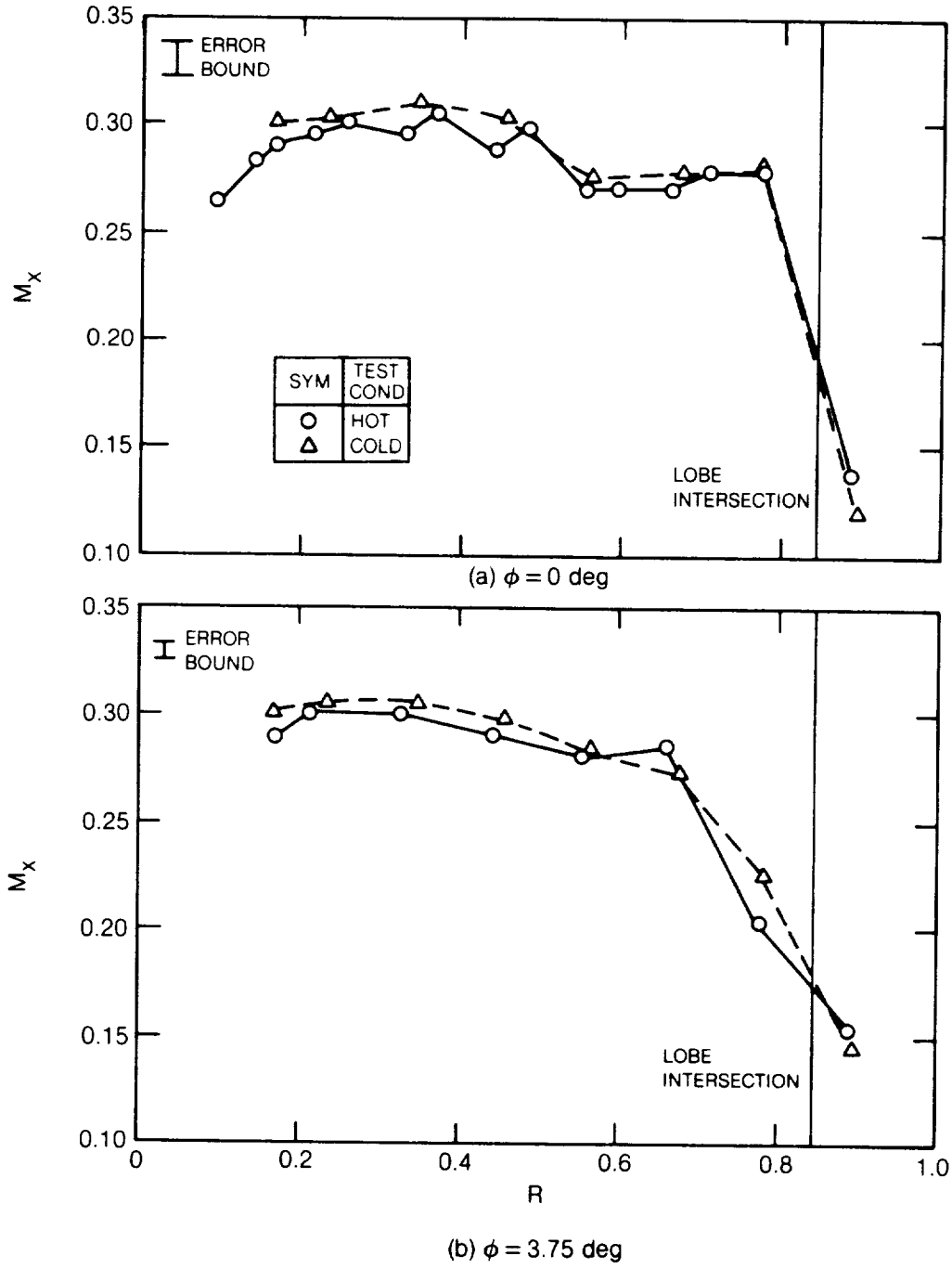

Figure 10 — Axial Mach Number Distributions for Hot and Cold Test Conditions at Inlet Station 1

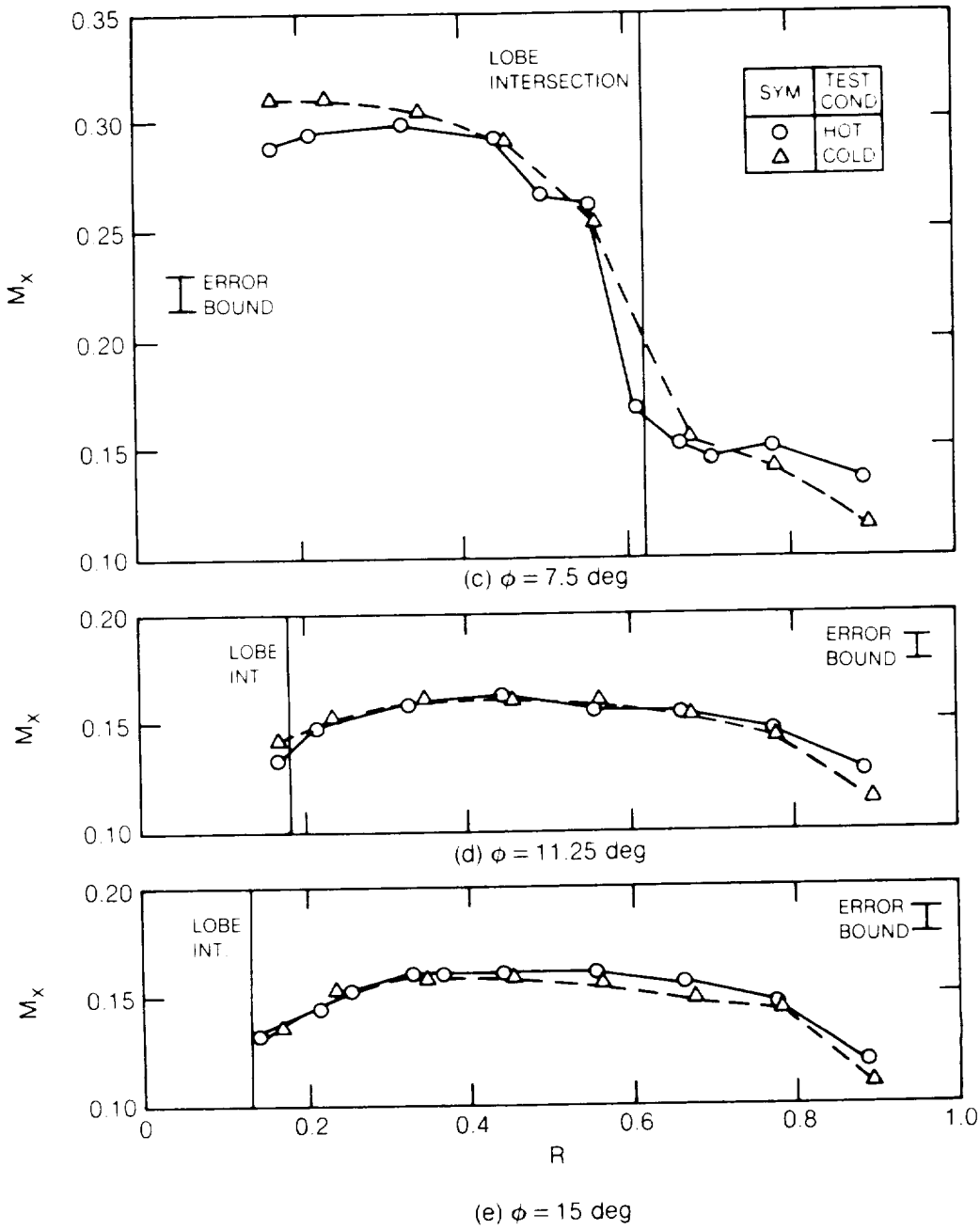

Figure 10 — Concluded

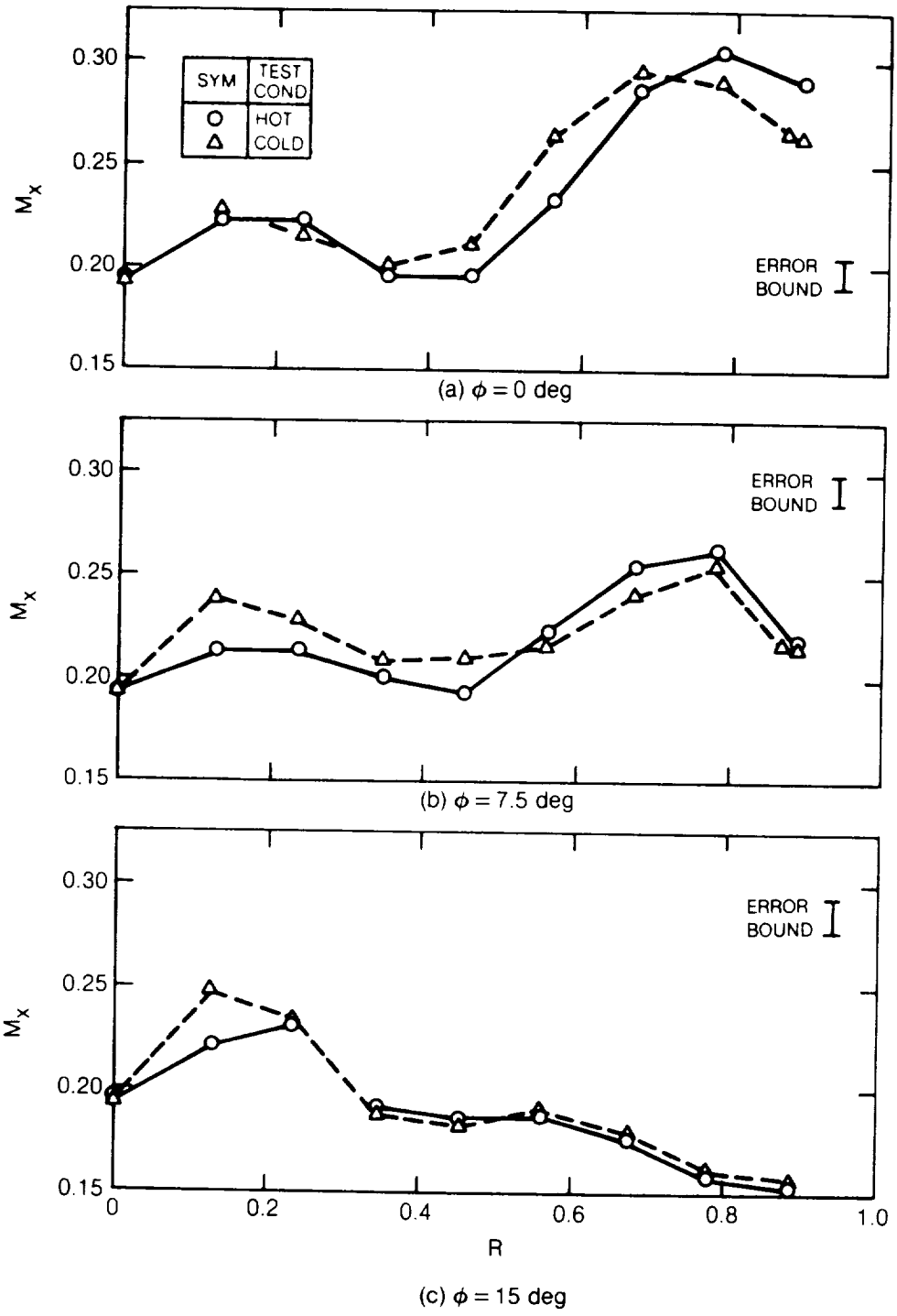

Figure 11 — Axial Mach Number Distributions for Hot and Cold Flow Test Conditions at Intermediate Station 2

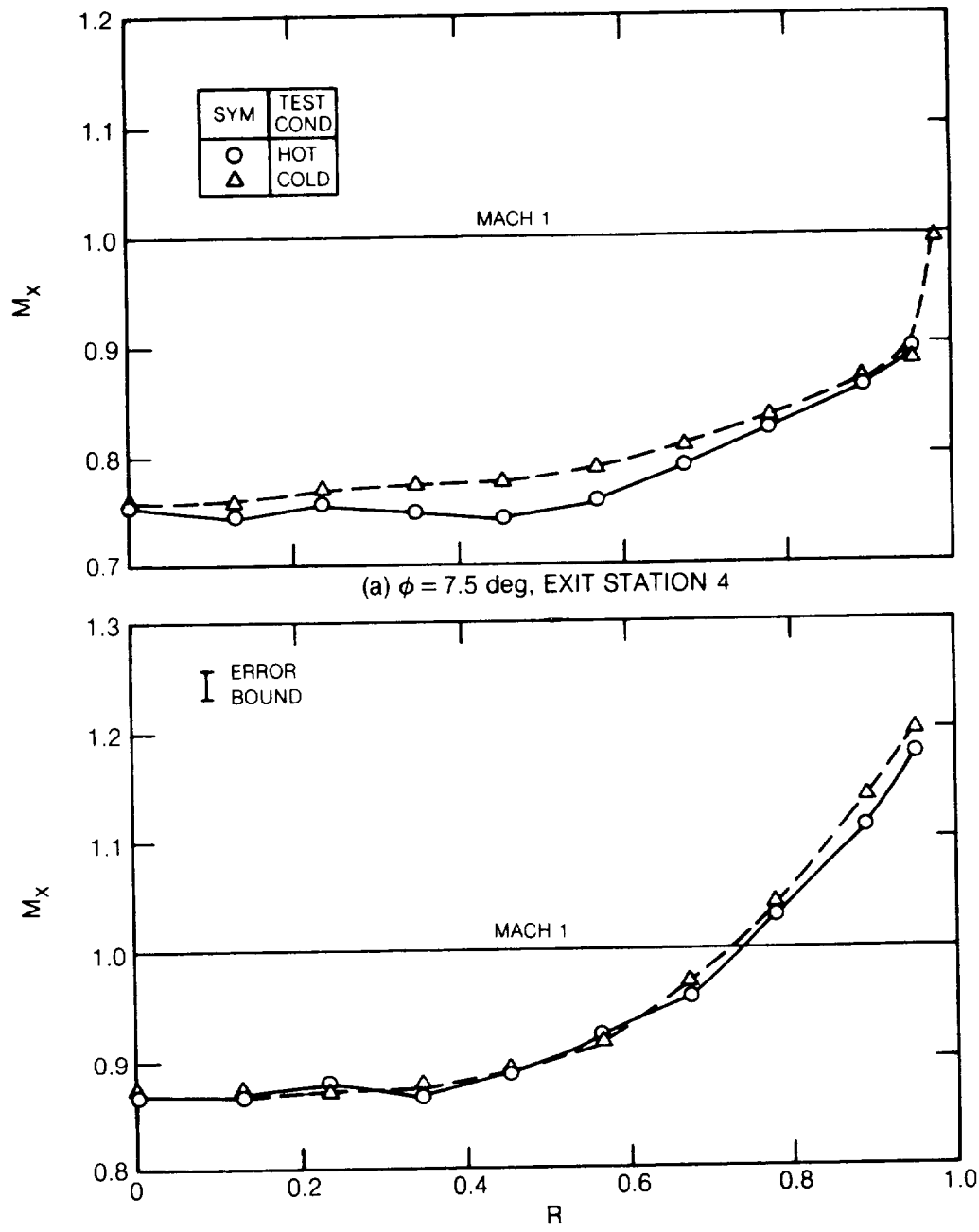

Figure 12 — Axial Mach Number Distributions for Hot and Cold Flow Test Conditions at Exit Station 4 and Plume Plane Station 3

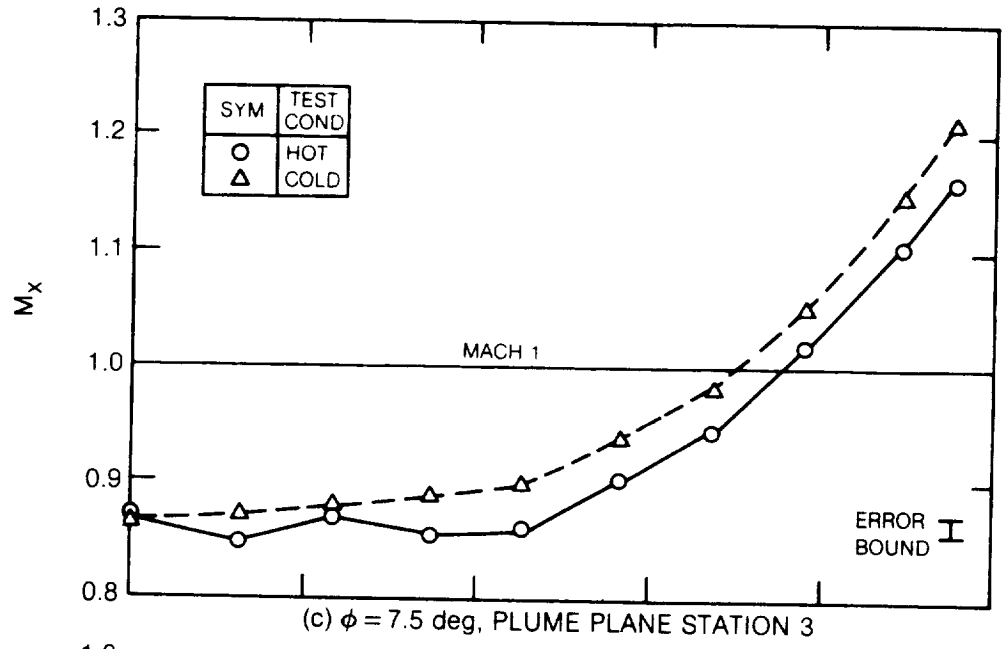

(c) $\phi = 7.5$ deg, PLUME PLANE STATION 3

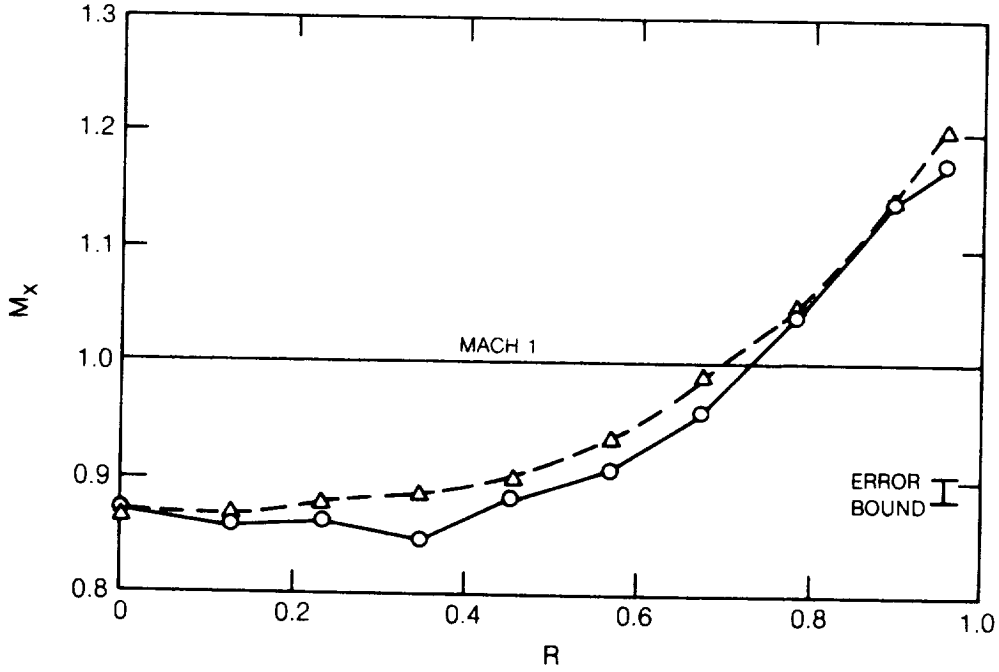

(d) $\phi = 15$ deg, PLUME PLANE STATION 3

Figure 12 — Concluded

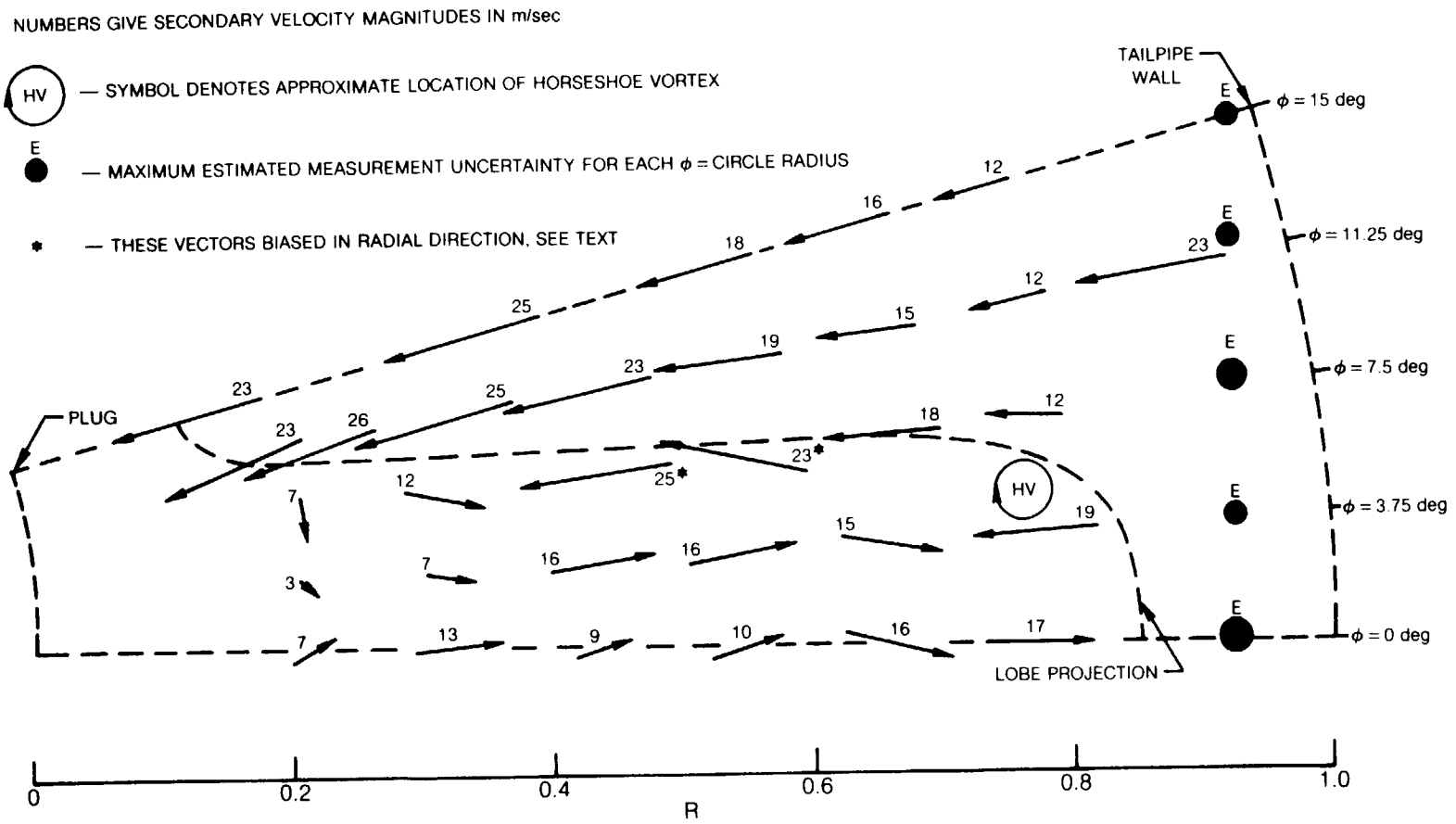

(a) HOT FLOW, INLET STATION 1

Figure 13 — Secondary Flow Velocity Vectors for Hot and Cold Test Conditions

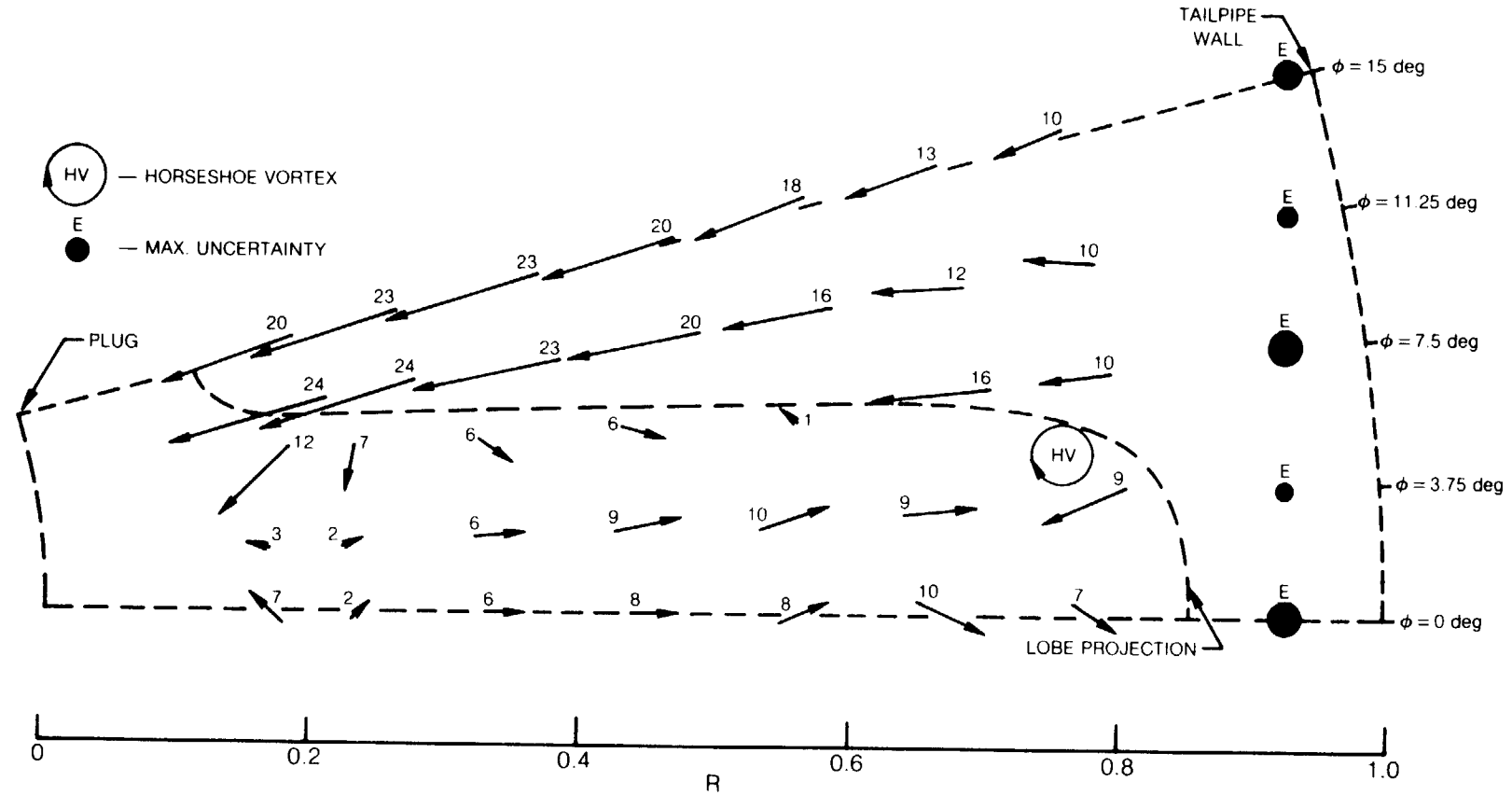

(b) COLD FLOW, INLET STATION 1

Figure 13 — Secondary Flow Velocity Vectors for Hot and Cold Test Conditions (Continued)

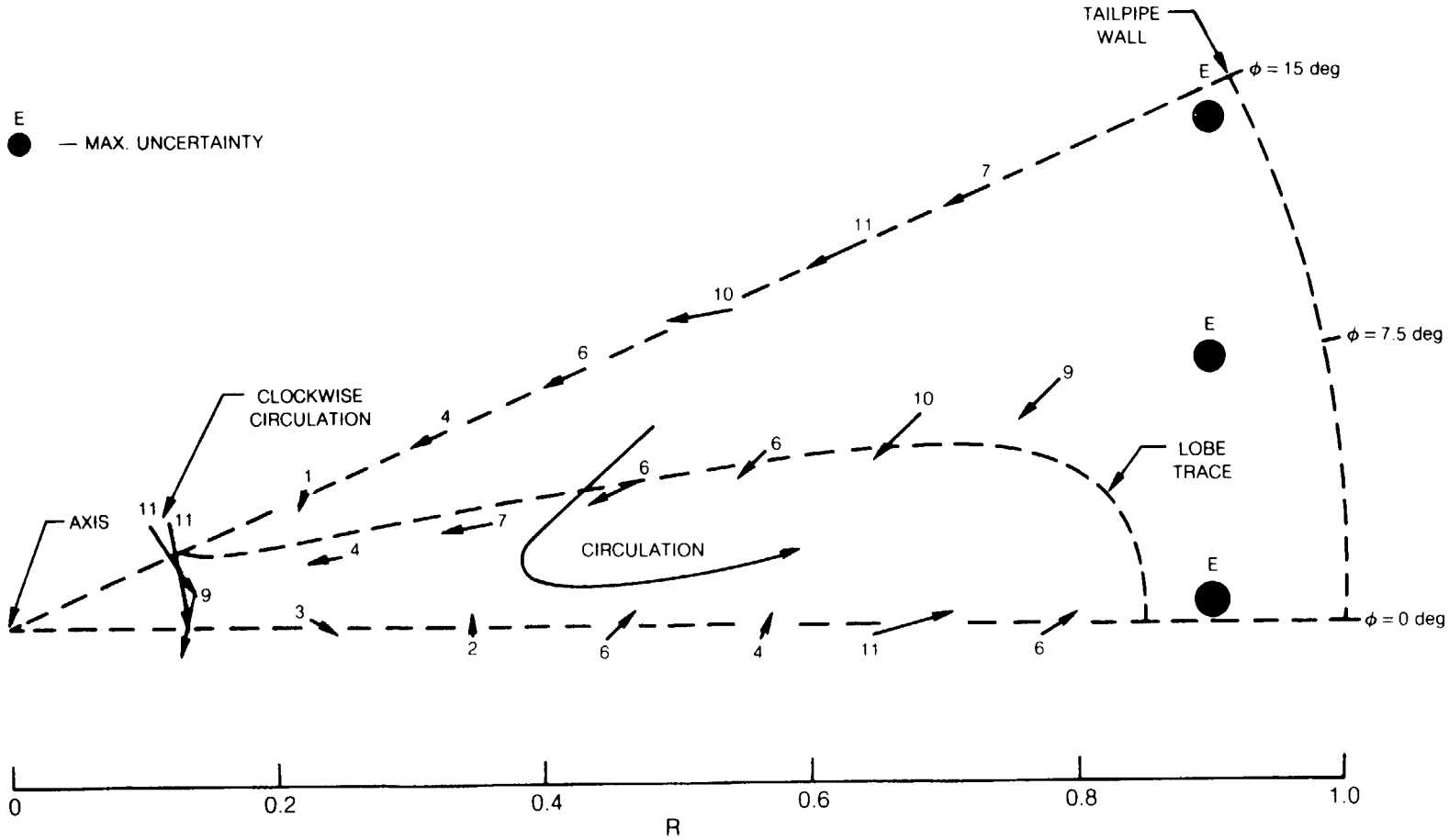

(c) HOT FLOW, INTERMEDIATE STATION 2

Figure 13 — Secondary Flow Velocity Vectors for Hot and Cold Test Conditions (Continued)

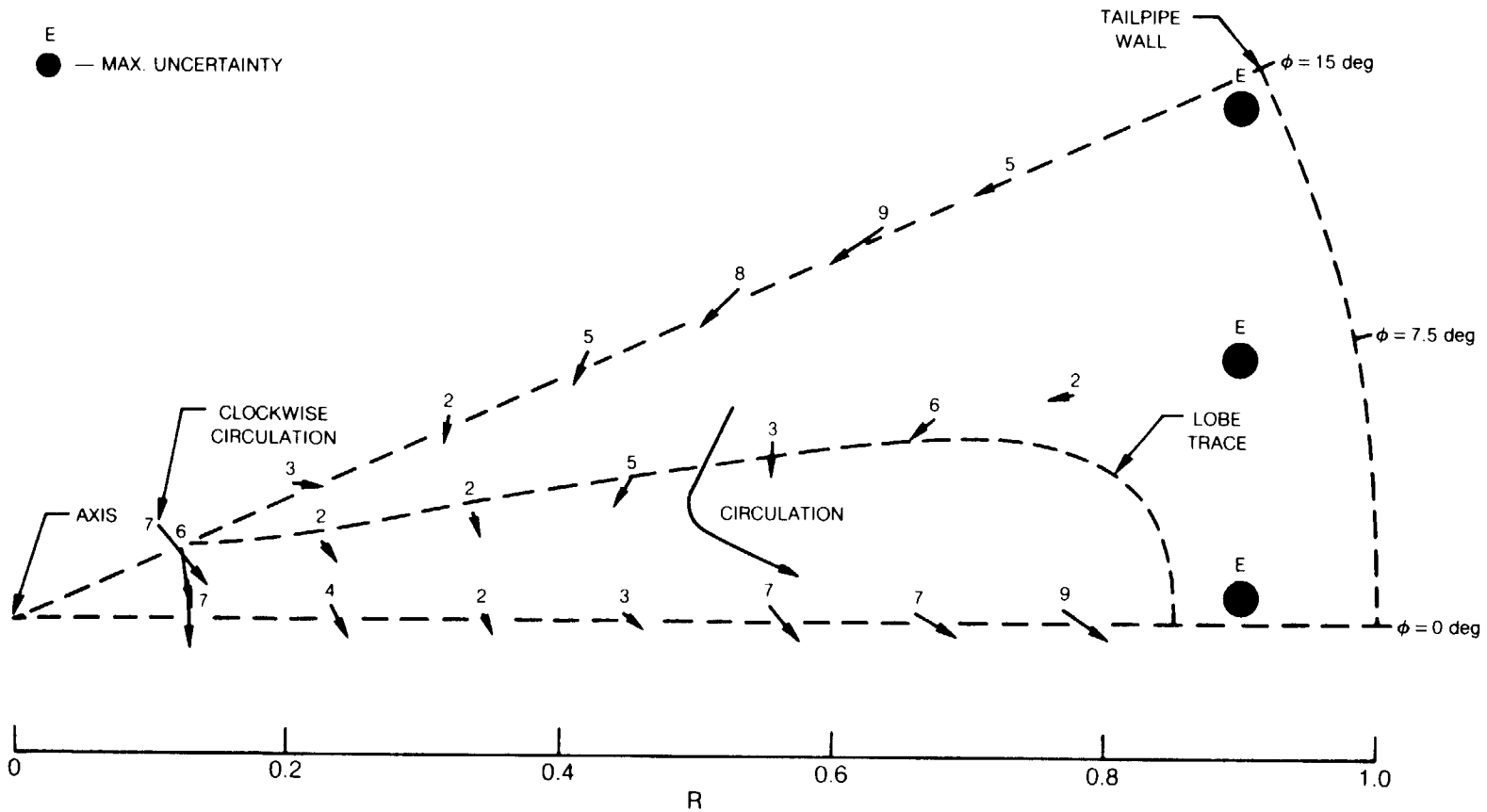

(d) COLD FLOW, INTERMEDIATE STATION 2

Figure 13 — Secondary Flow Velocity Vectors for Hot and Cold Test Conditions (Continued)

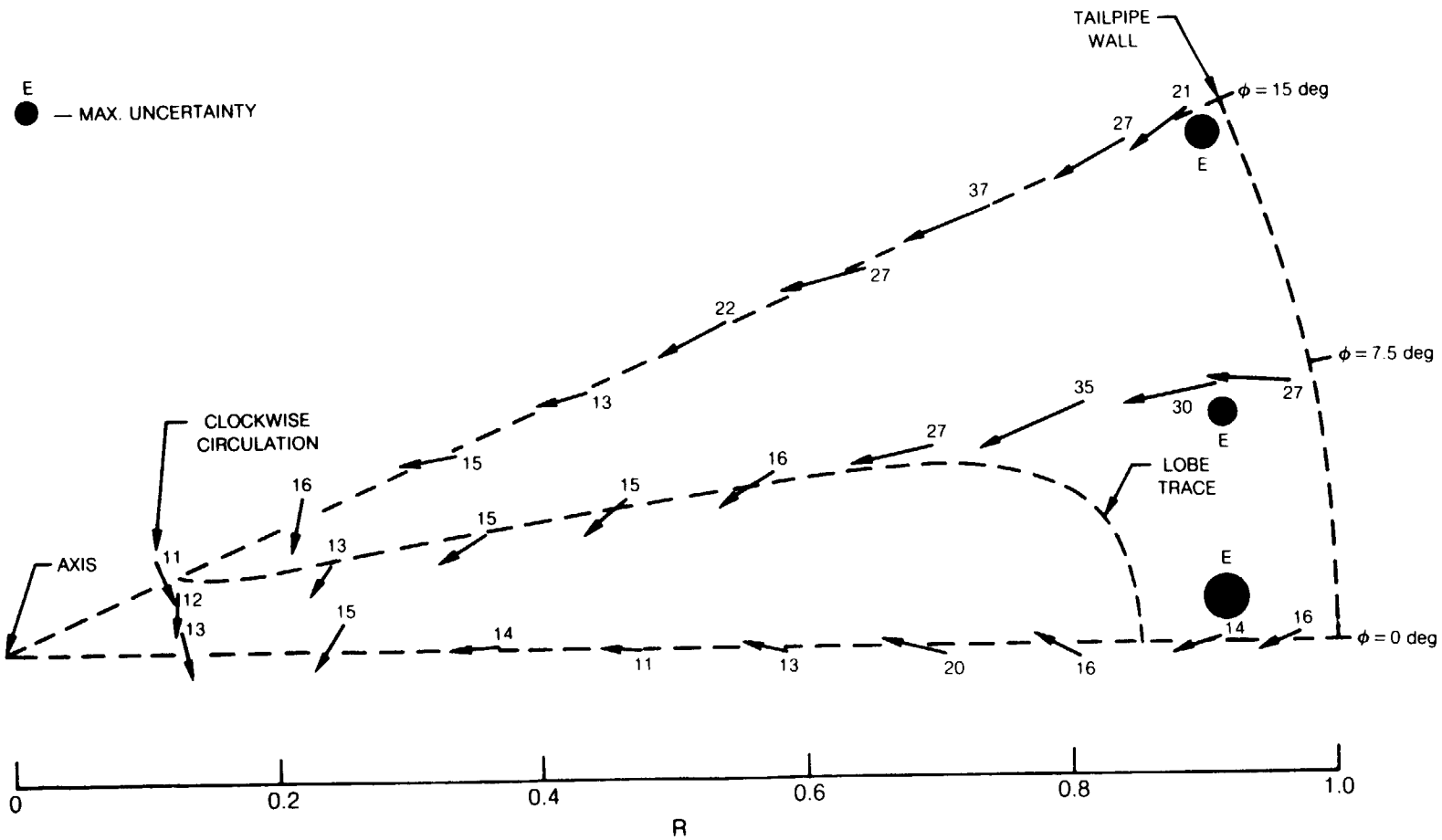

(e) HOT FLOW, PLUME PLANE STATION 3

Figure 13 — Secondary Flow Velocity Vectors for Hot and Cold Test Conditions (Continued)

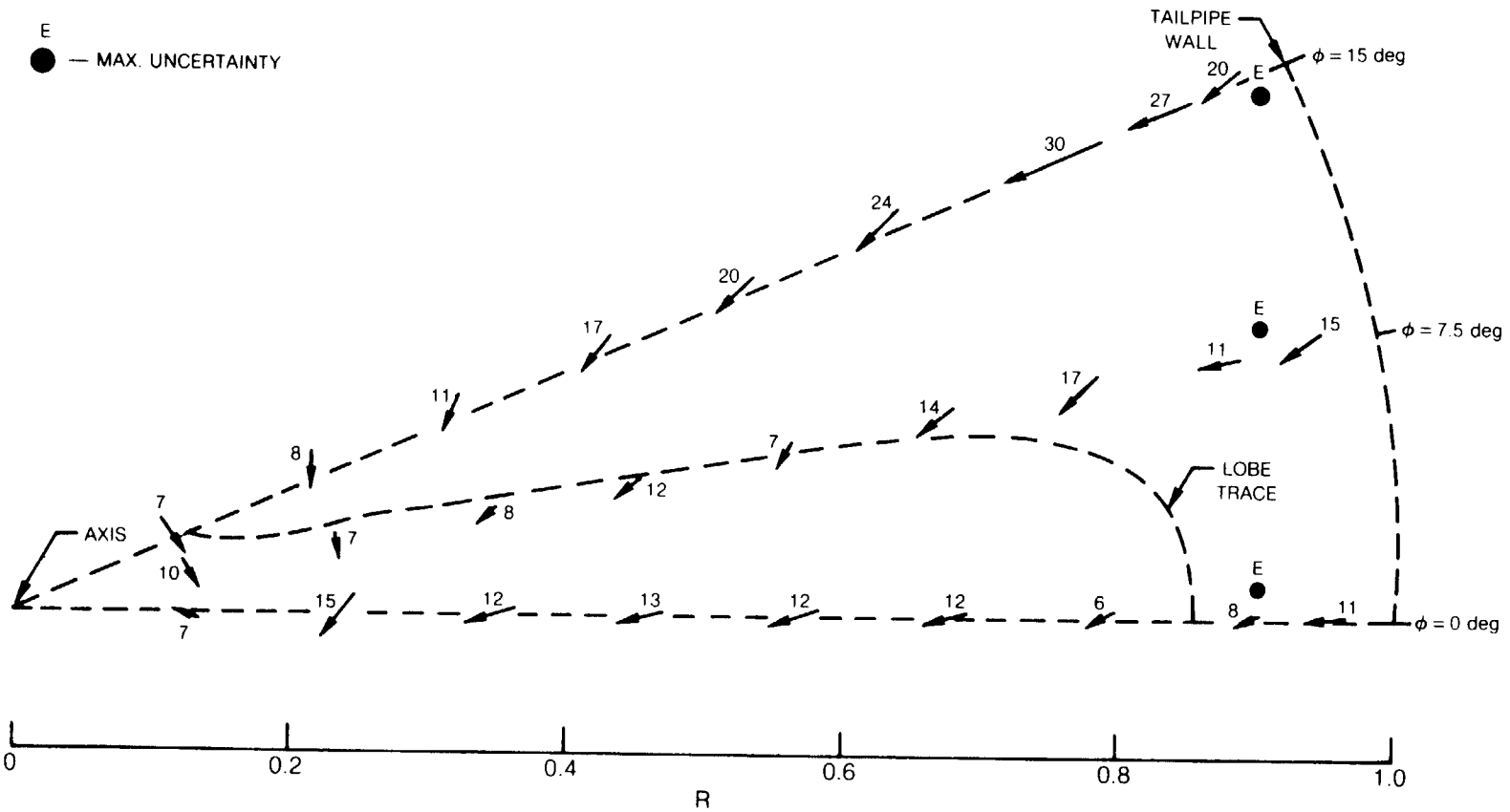

(f) COLD FLOW, PLUME PLANE STATION

Figure 13 — Secondary Flow Velocity Vectors for Hot and Cold Test Conditions (Concluded)

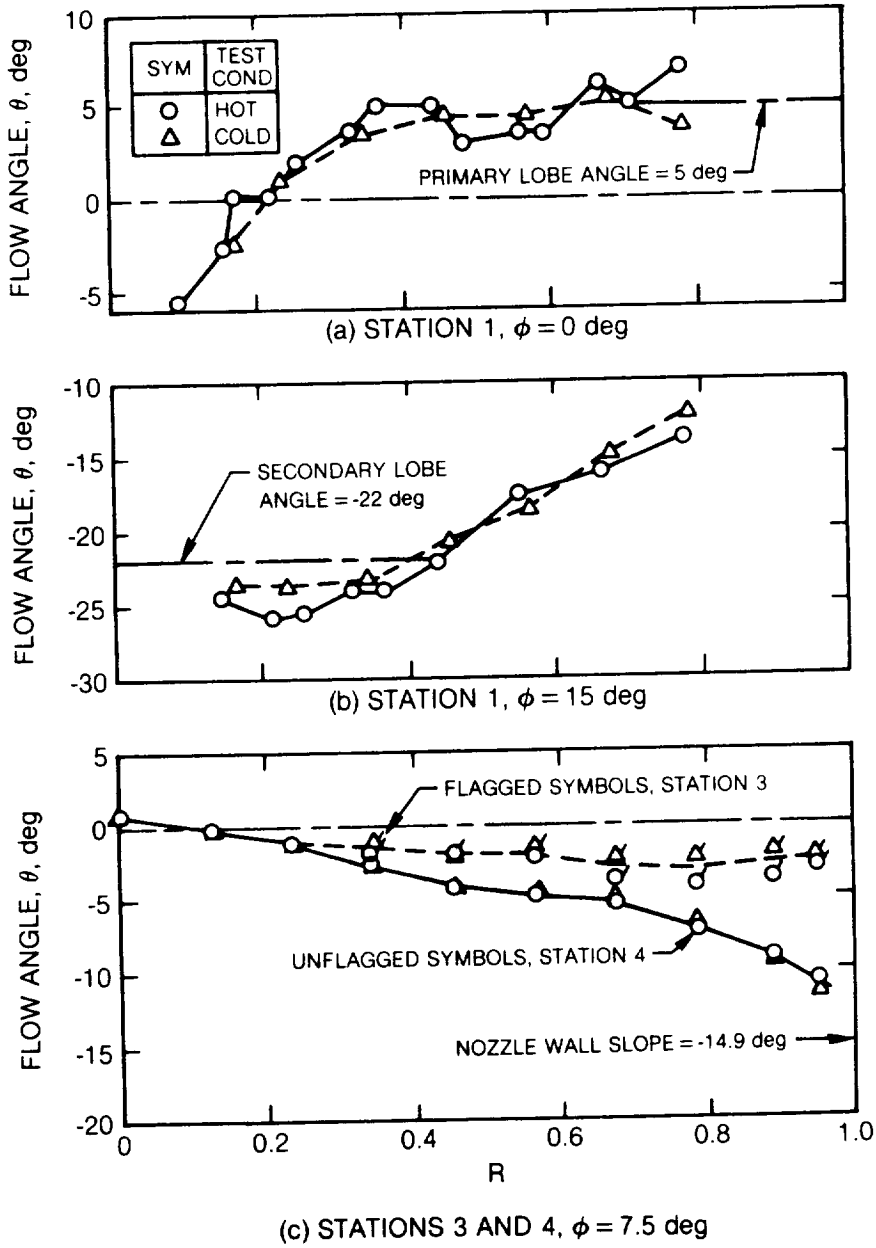

Figure 14 — Flow Angle in Radial-Axial Plane at Inlet Station 1, Plume Plane Station 3 and Exit Plane Station 4

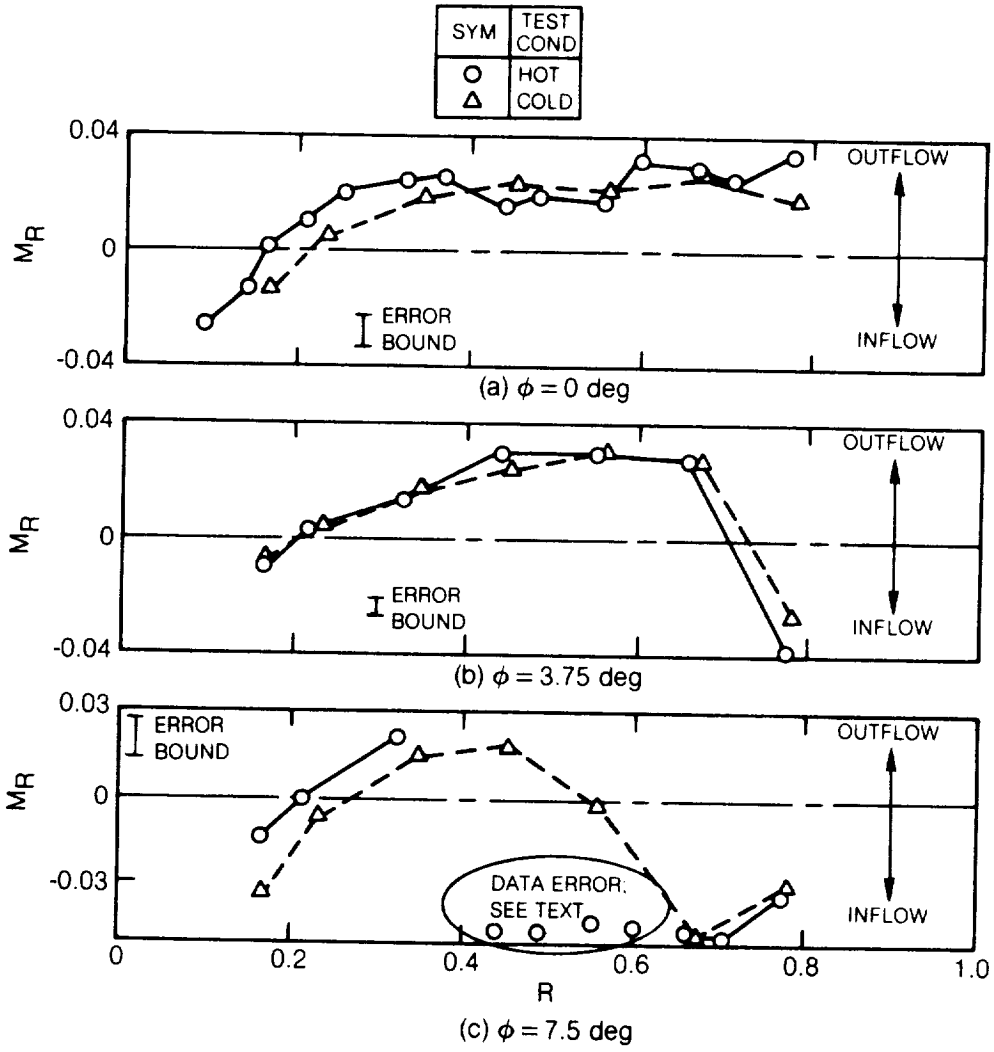

Figure 15 — Radial Mach Number Distributions for Hot and Cold Flow Test Conditions at Inlet Station 1

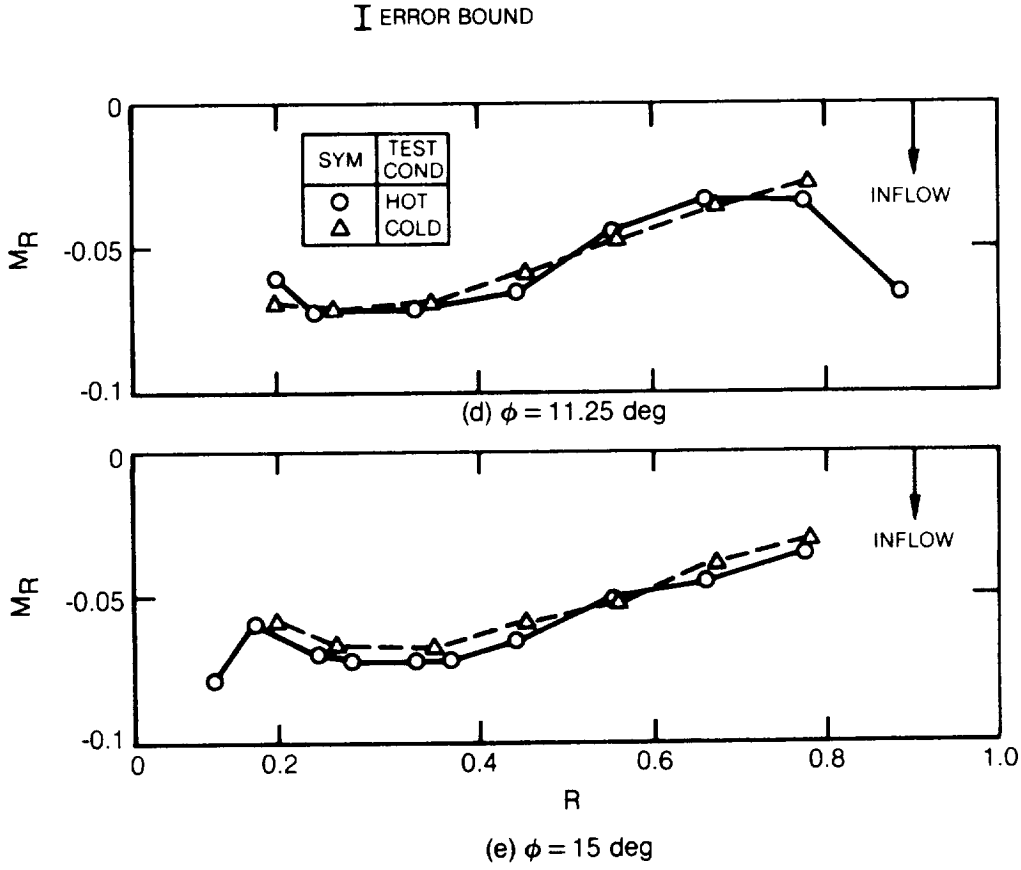

Figure 15 — Concluded

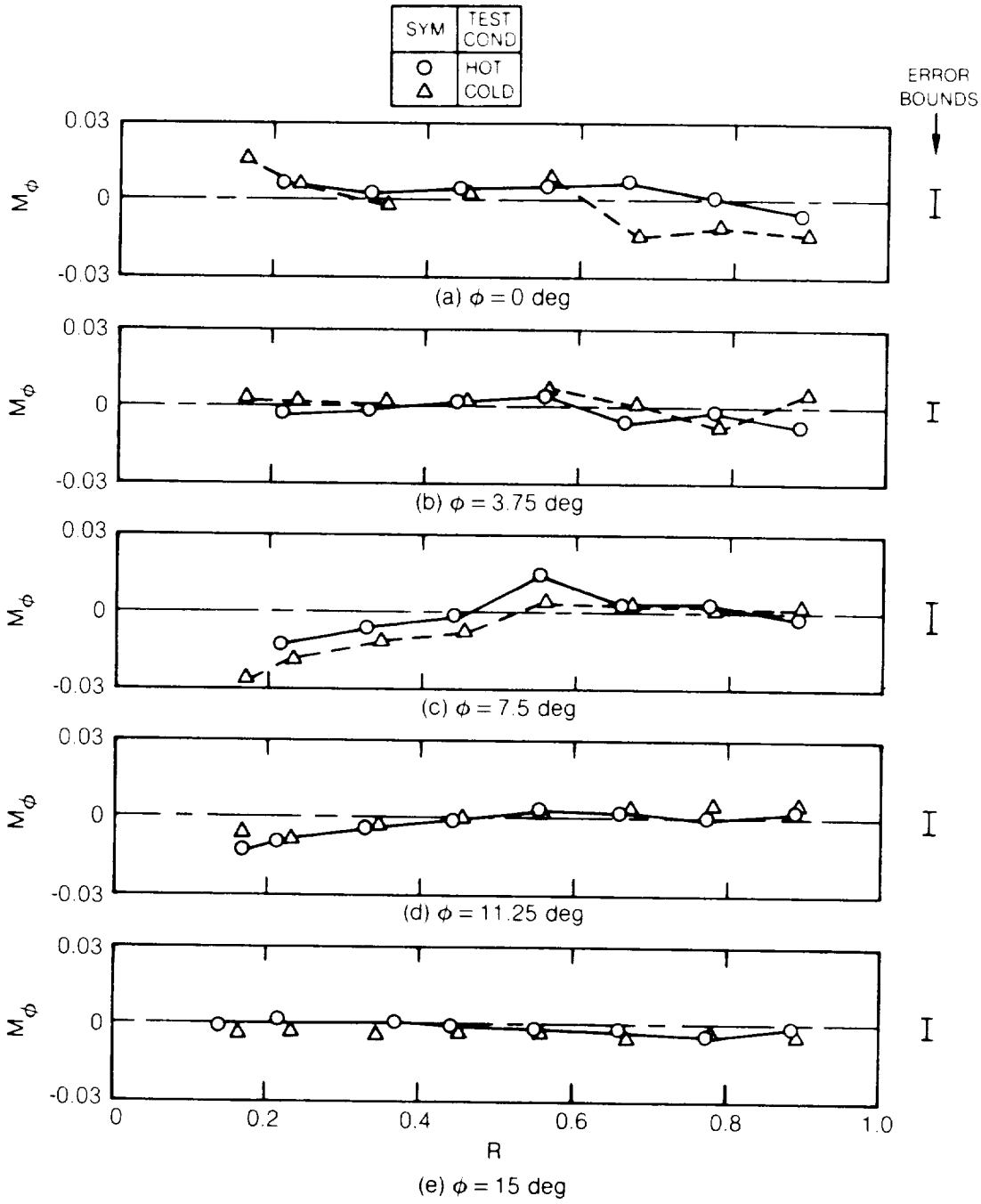

Figure 16 — Azimuthal Mach Number Distribution for Hot and Cold Flow Test Conditions at Inlet Station 1

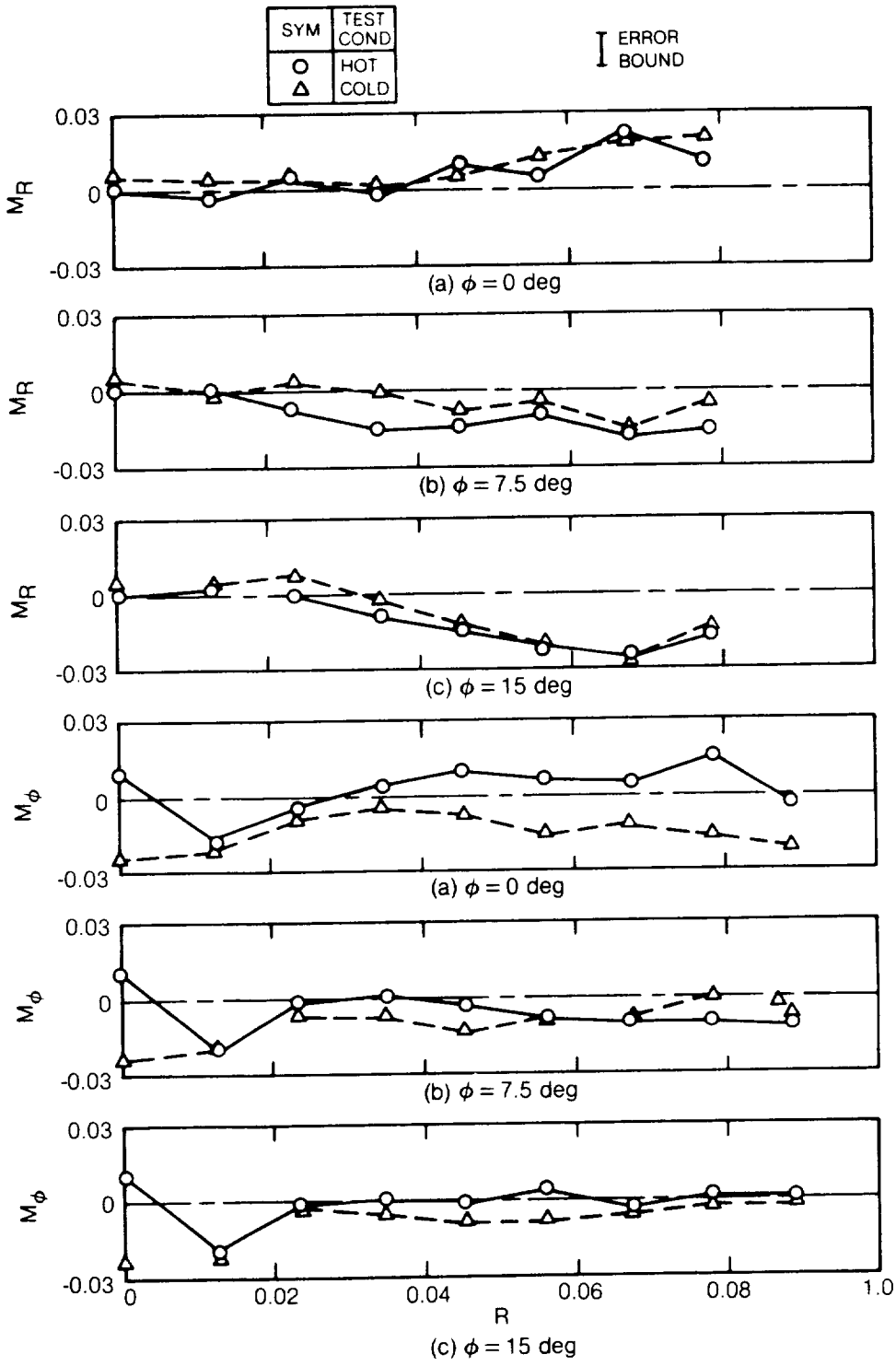

Figure 17 — Radial and Azimuthal Mach Number Distributions for Hot and Cold Flow Test Conditions at Intermediate Station 2

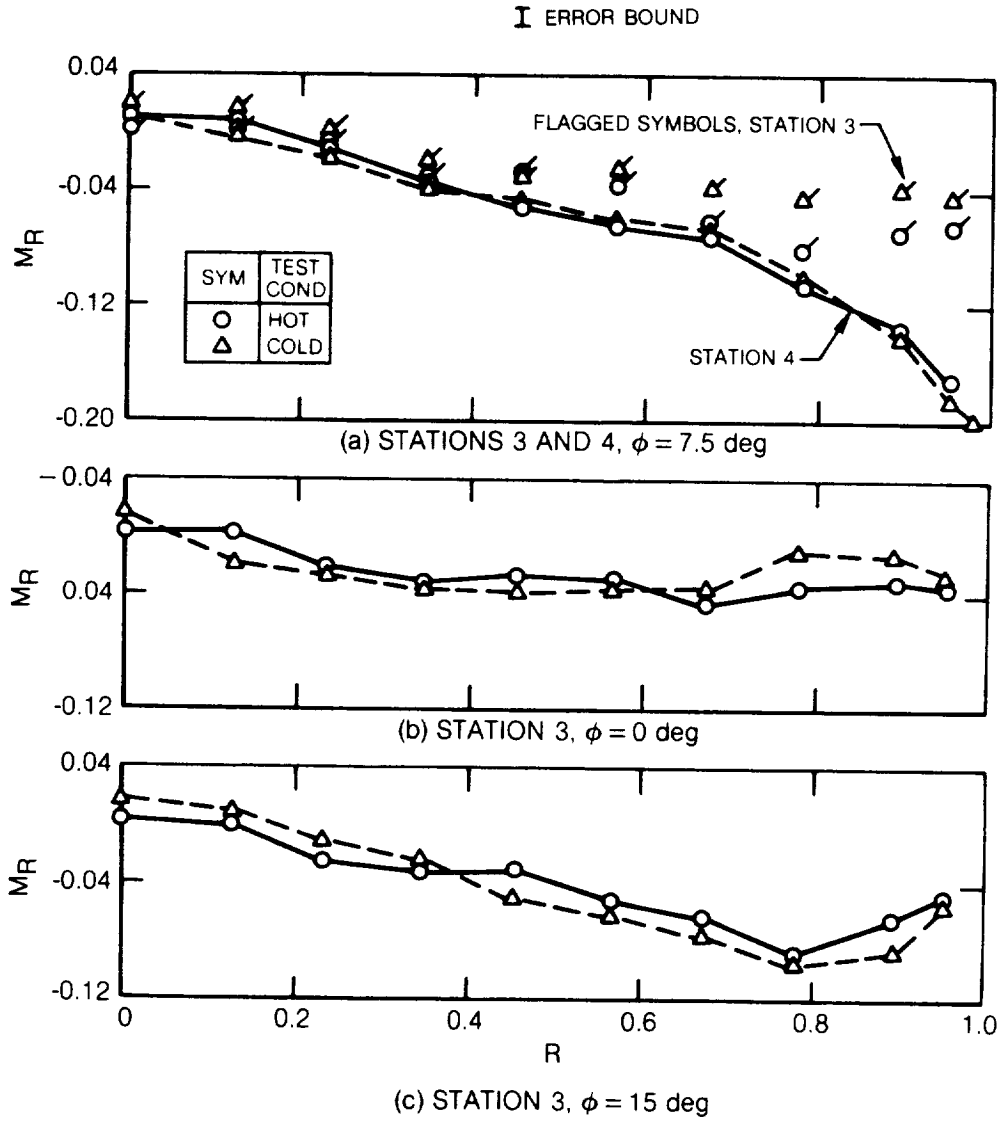

Figure 18 — Radial Mach Number Distributions for Hot and Cold Test Conditions at Exit Station 4 and Plume Plane Station 3

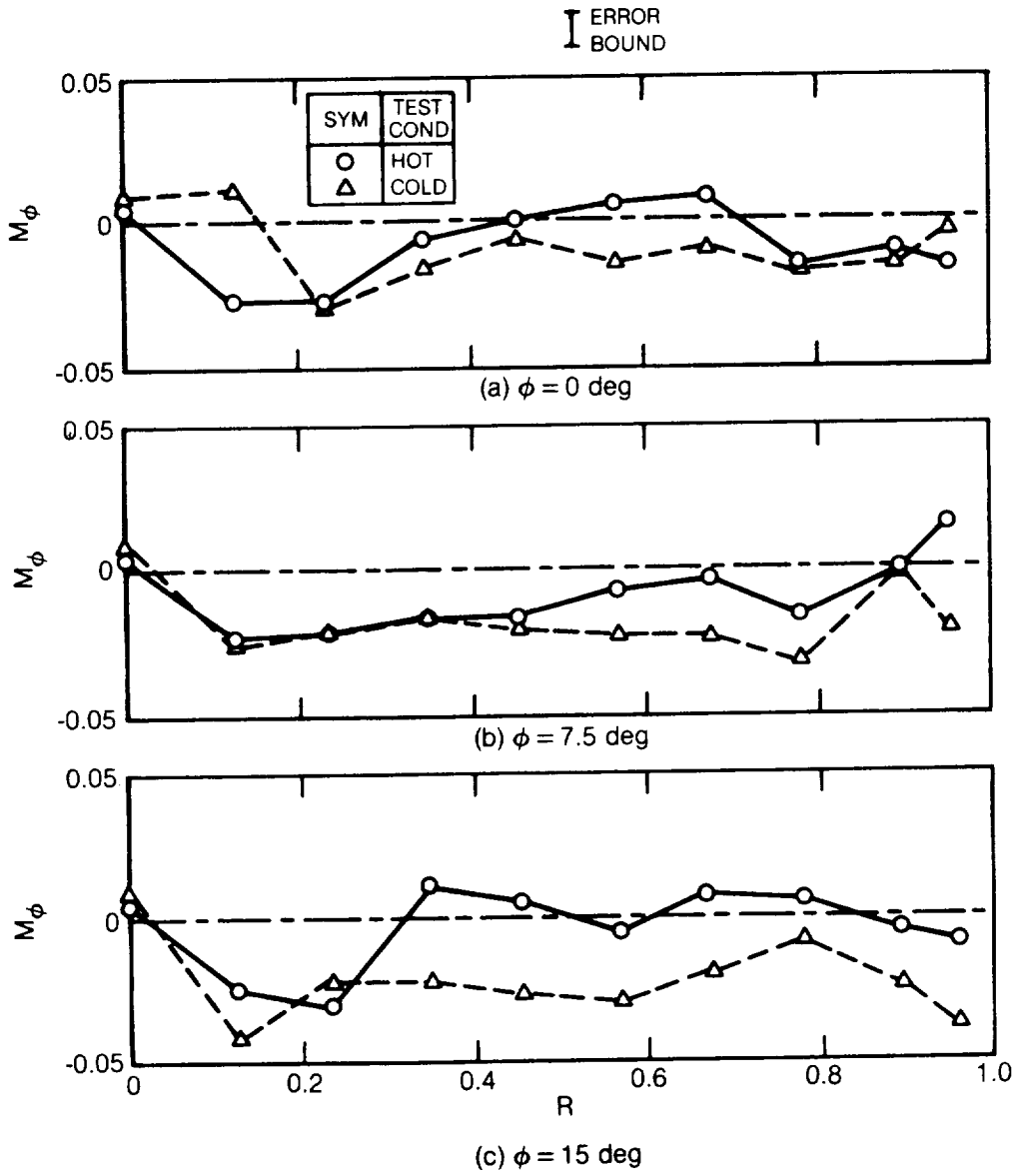

Figure 19 — Azimuthal Mach Number Distributions for Hot and Cold Test Conditions at Plume Plane Station 3

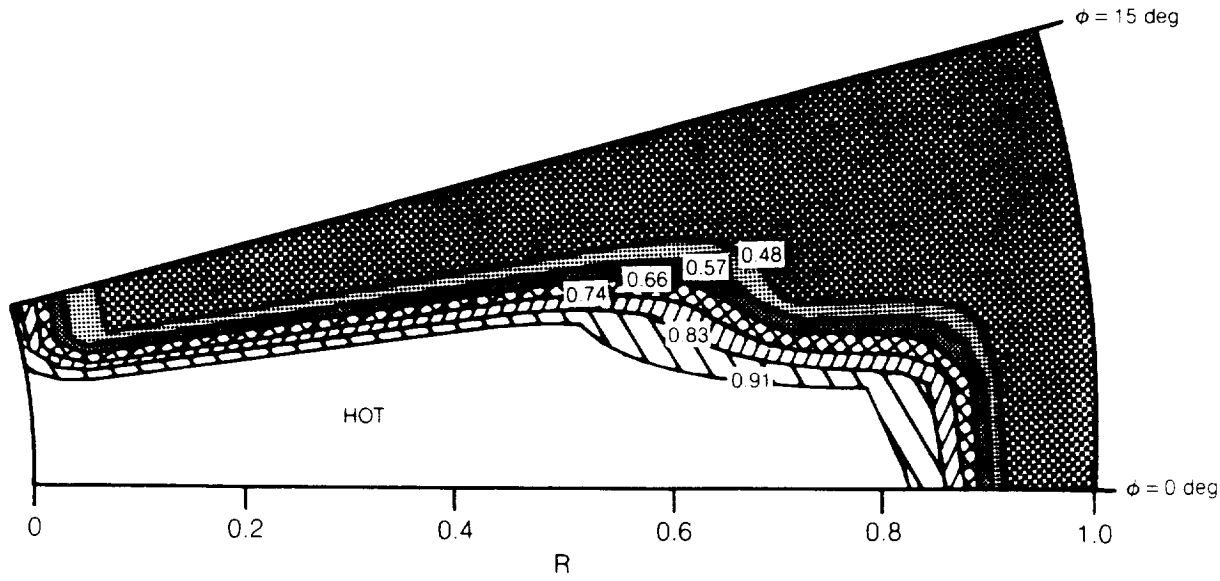

(a) T_T/T_{op} CONTOURS

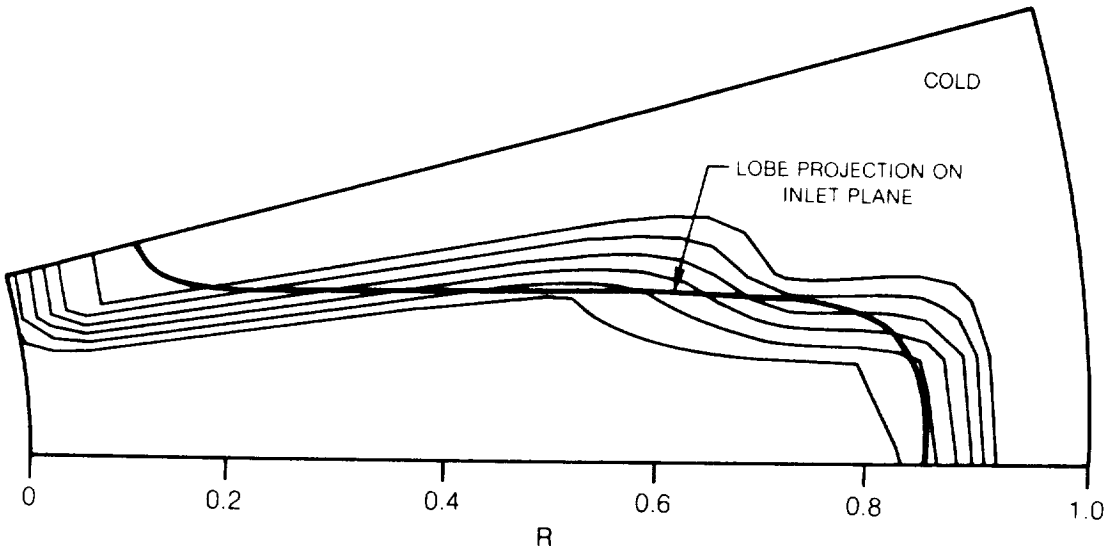

(b) CONTOURS RELATIVE TO LOBE PROJECTION

Figure 20 — Total Temperature Contours for Hot Flow Test Condition at Inlet Station 1

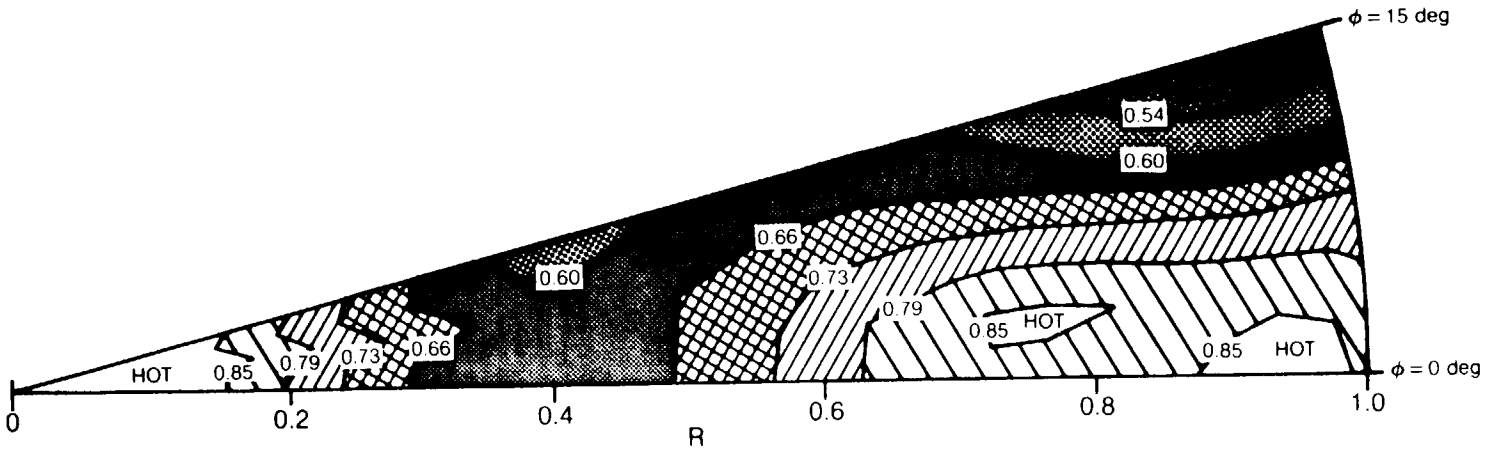

(a) T/T_{op} CONTOURS

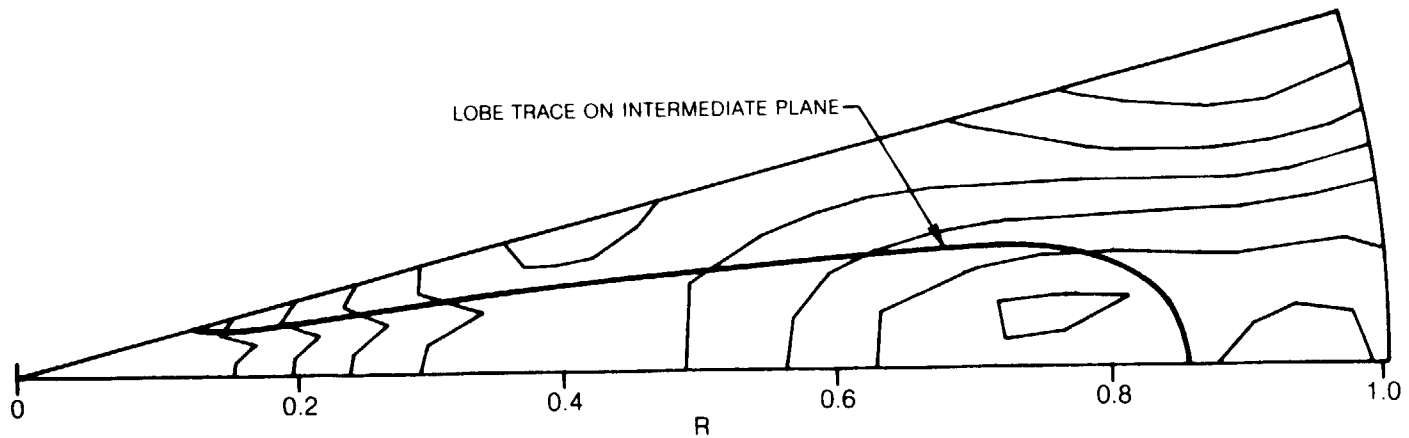

(b) CONTOURS RELATIVE TO LOBE TRACE

Figure 21 — Total Temperature Contours for Hot Flow Test Condition at Intermediate Station 2

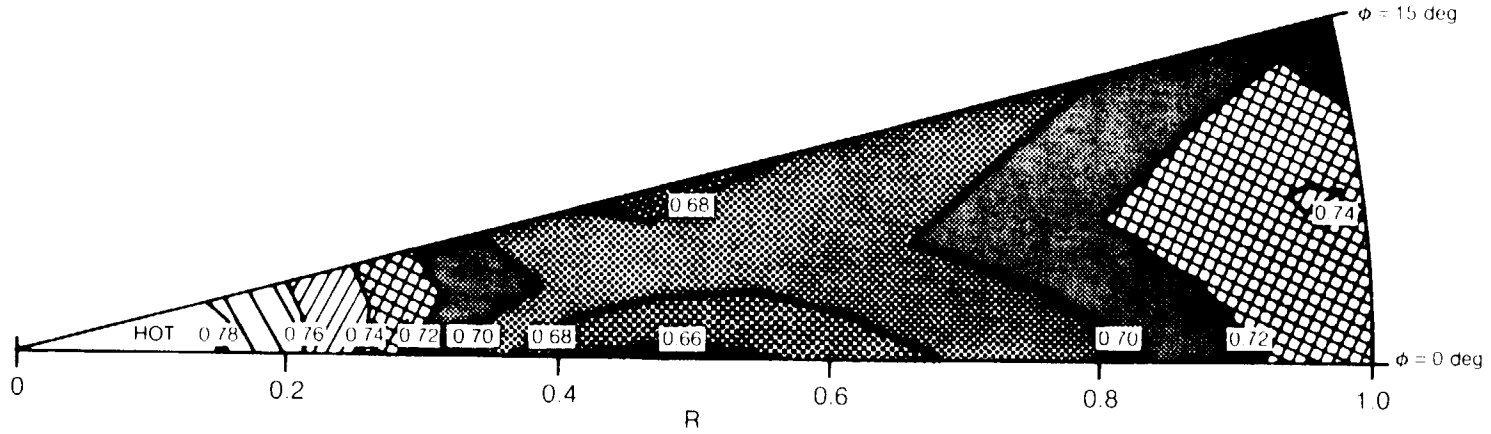

(a) T/T_{op} CONTOURS

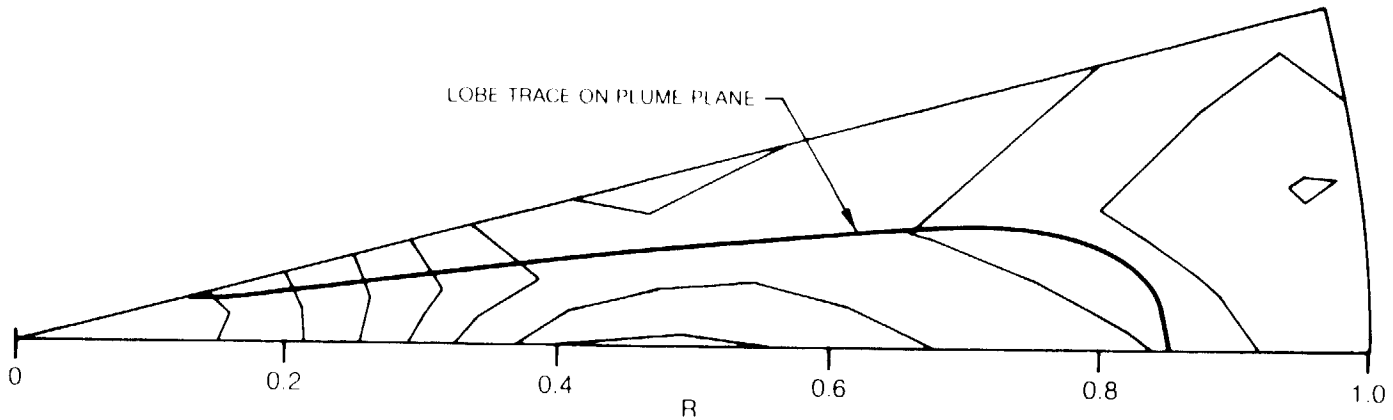

(b) CONTOURS RELATIVE TO LOBE TRACE

Figure 22 — Total Temperature Contours for Hot Flow Test Condition at Plume Plane Station 3

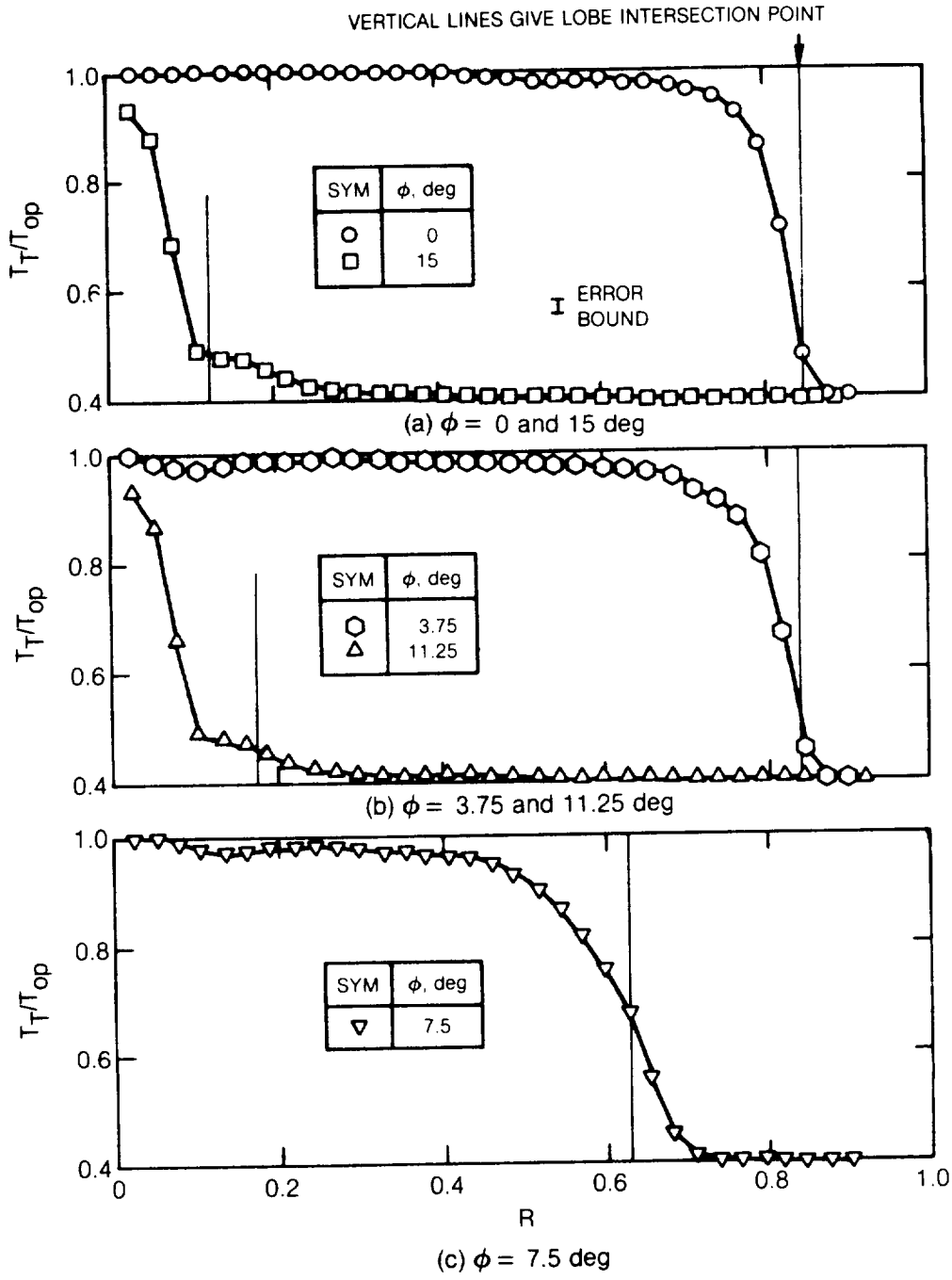

Figure 23 — Total Temperature Distributions for Hot Flow Test Condition at Inlet Station 1

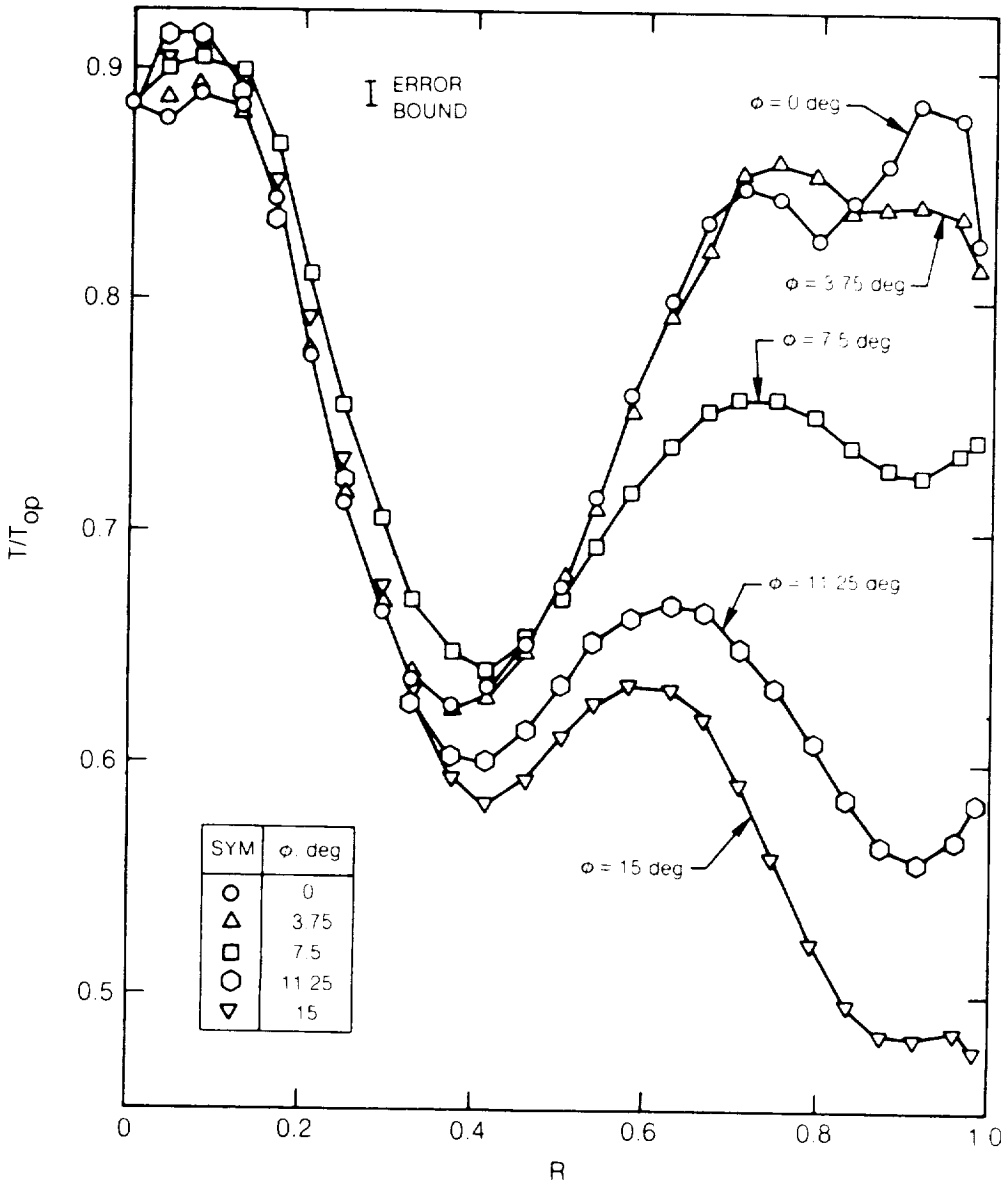

Figure 24 — Total Temperature Distributions for Hot Flow Test Condition at Intermediate Station 2

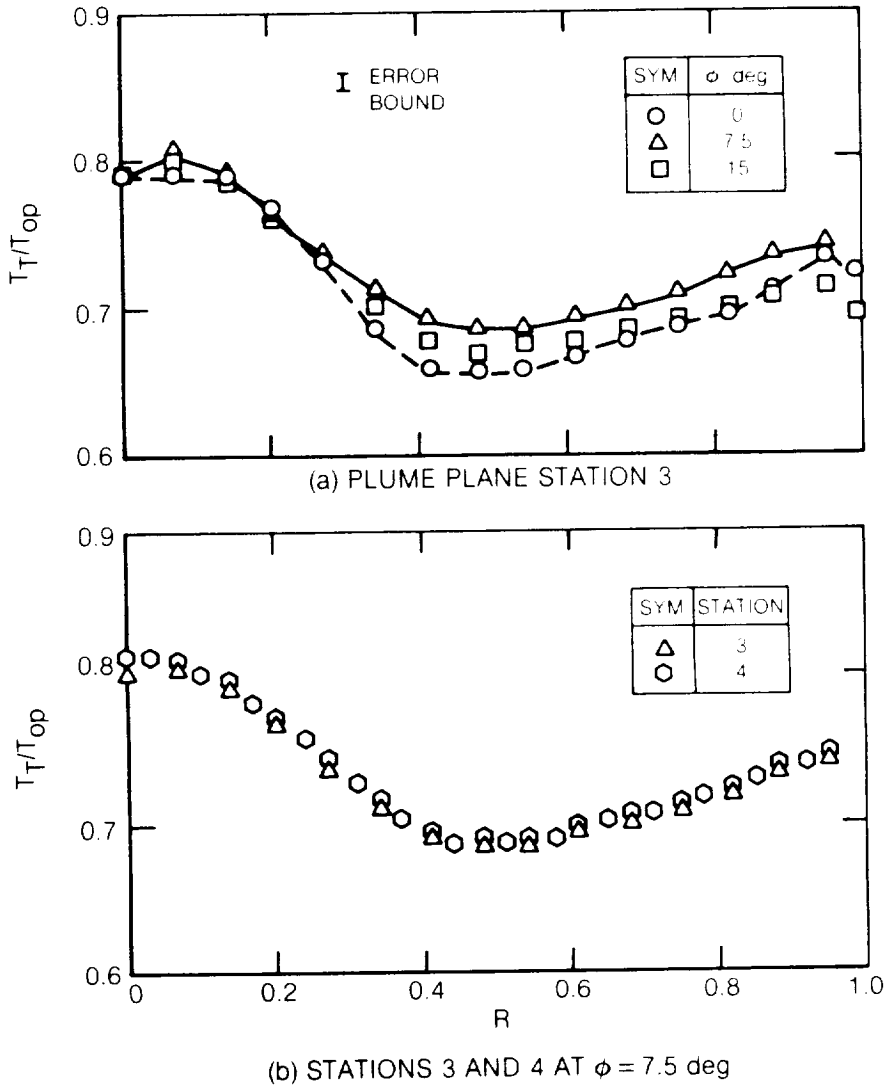

Figure 25 — Total Temperature Distributions for Hot Flow Test Condition at Plume Plane Station 3 and Exit Plane 4

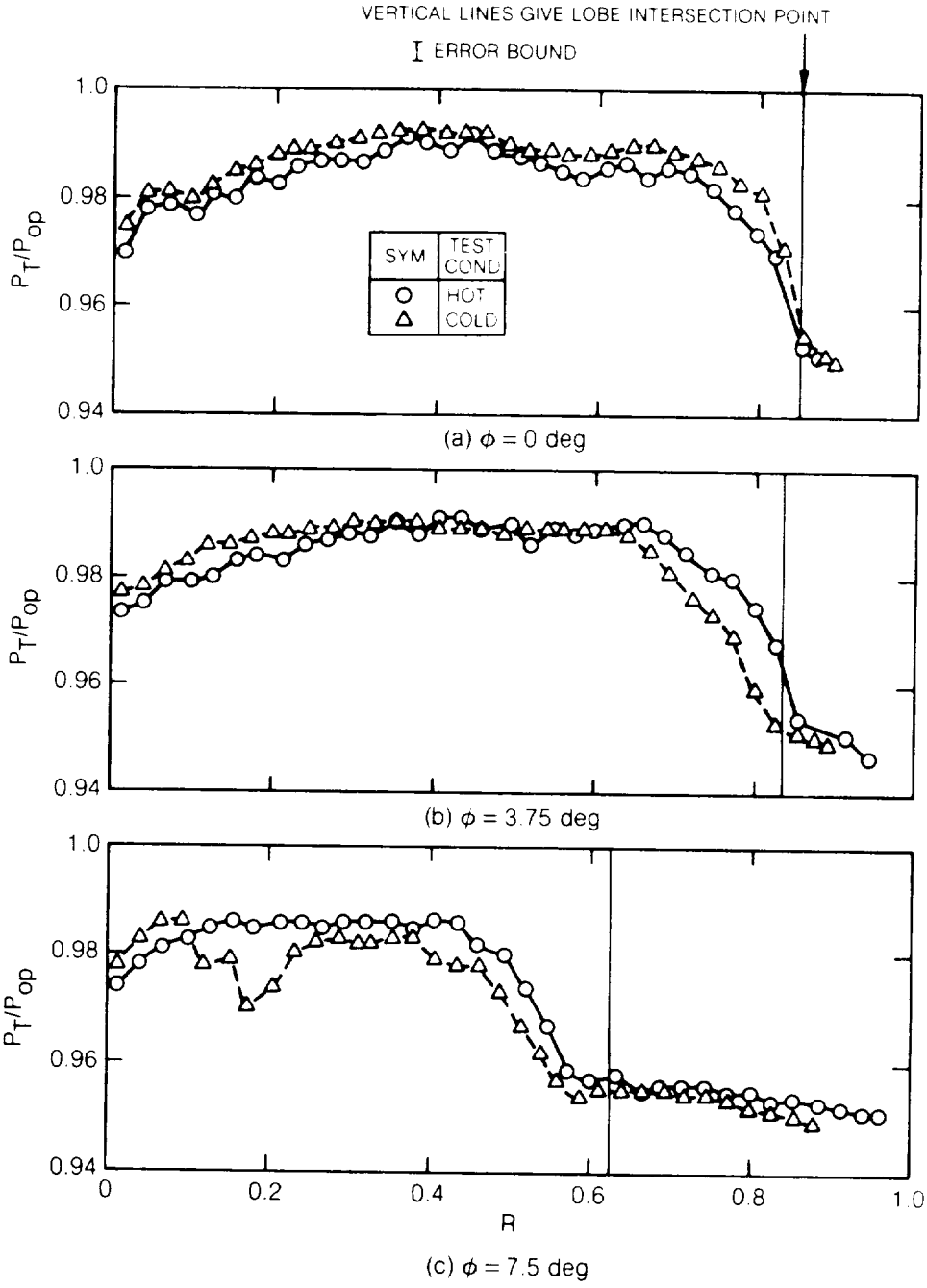

Figure 26 — Total Pressure Distributions for Hot and Cold Flow Test Conditions at Inlet Station 1

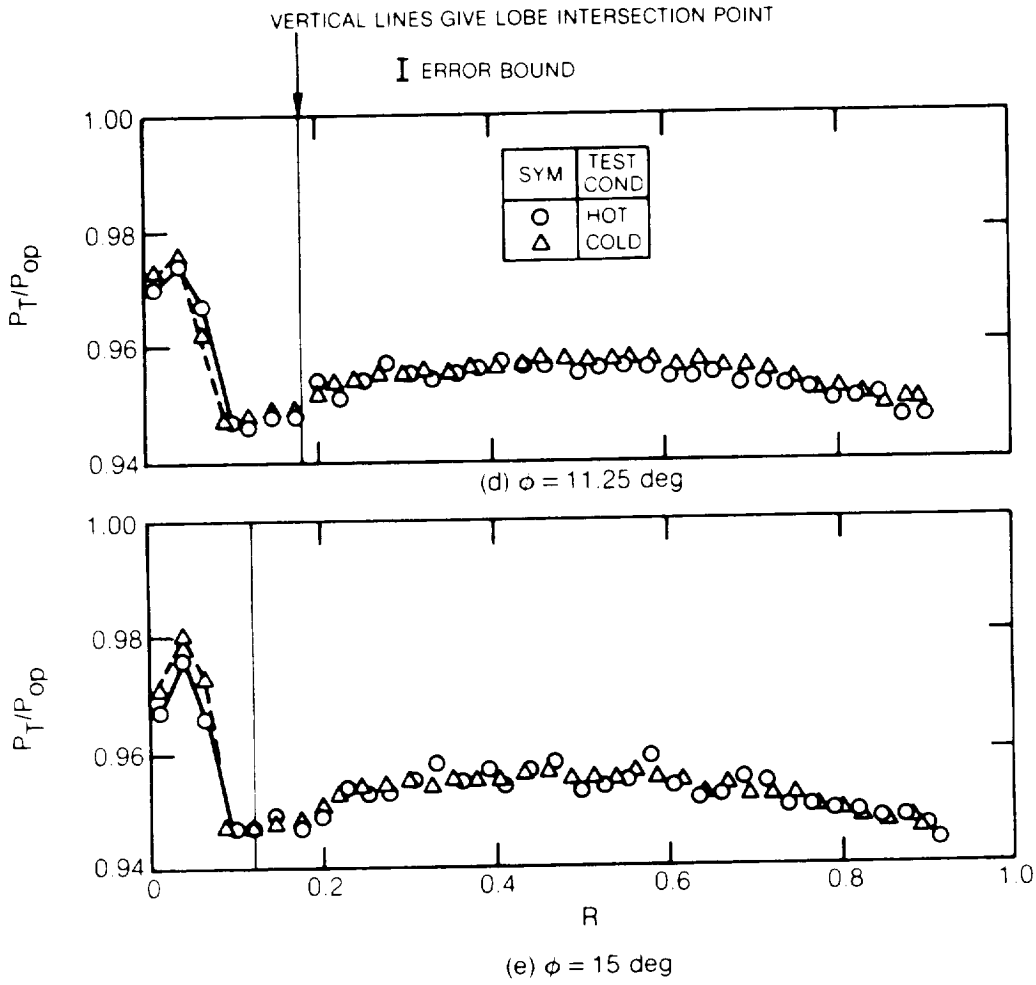

Figure 26 — Concluded

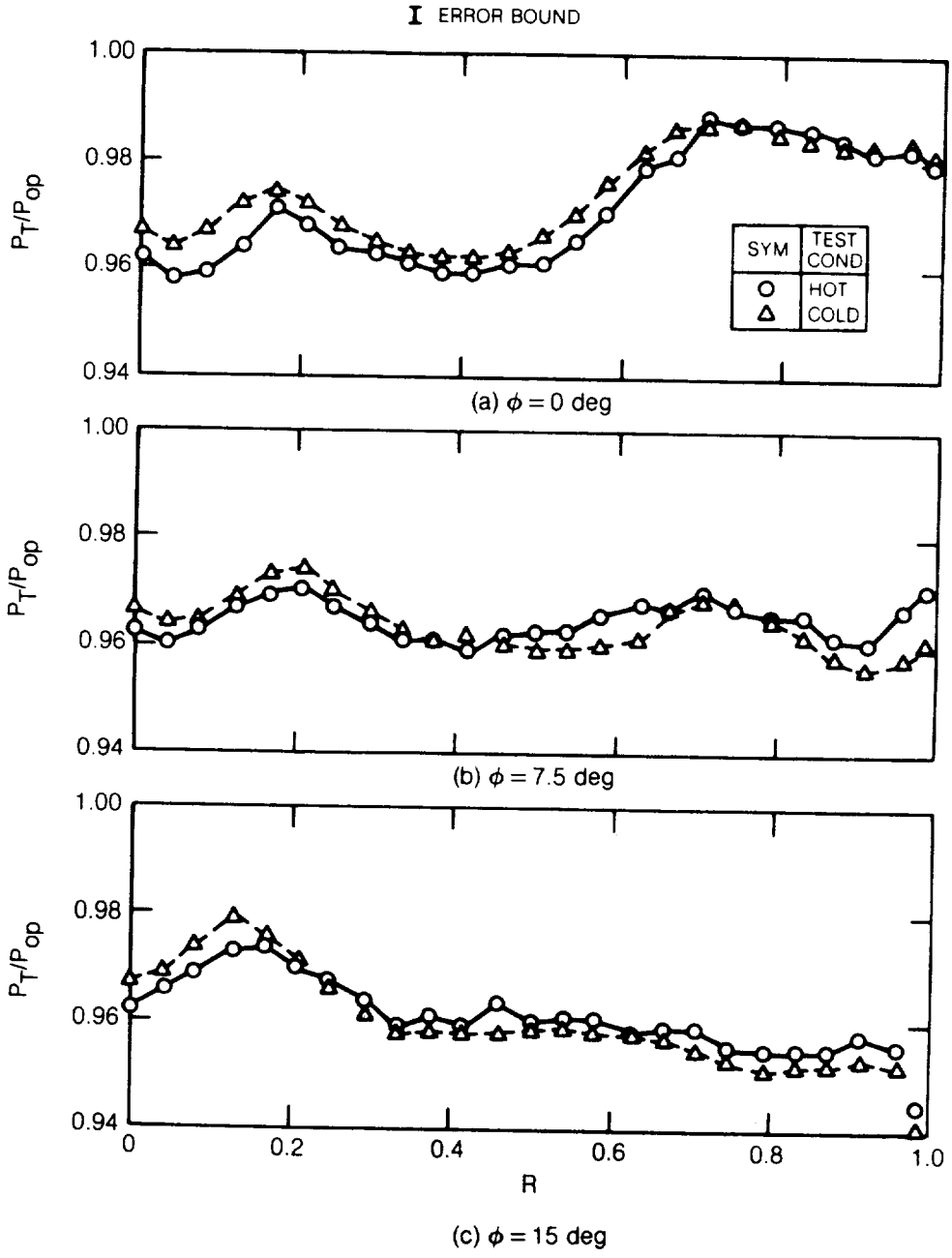

Figure 27 — Total Pressure Distributions for Hot and Cold Flow Test Conditions at Intermediate Station 2

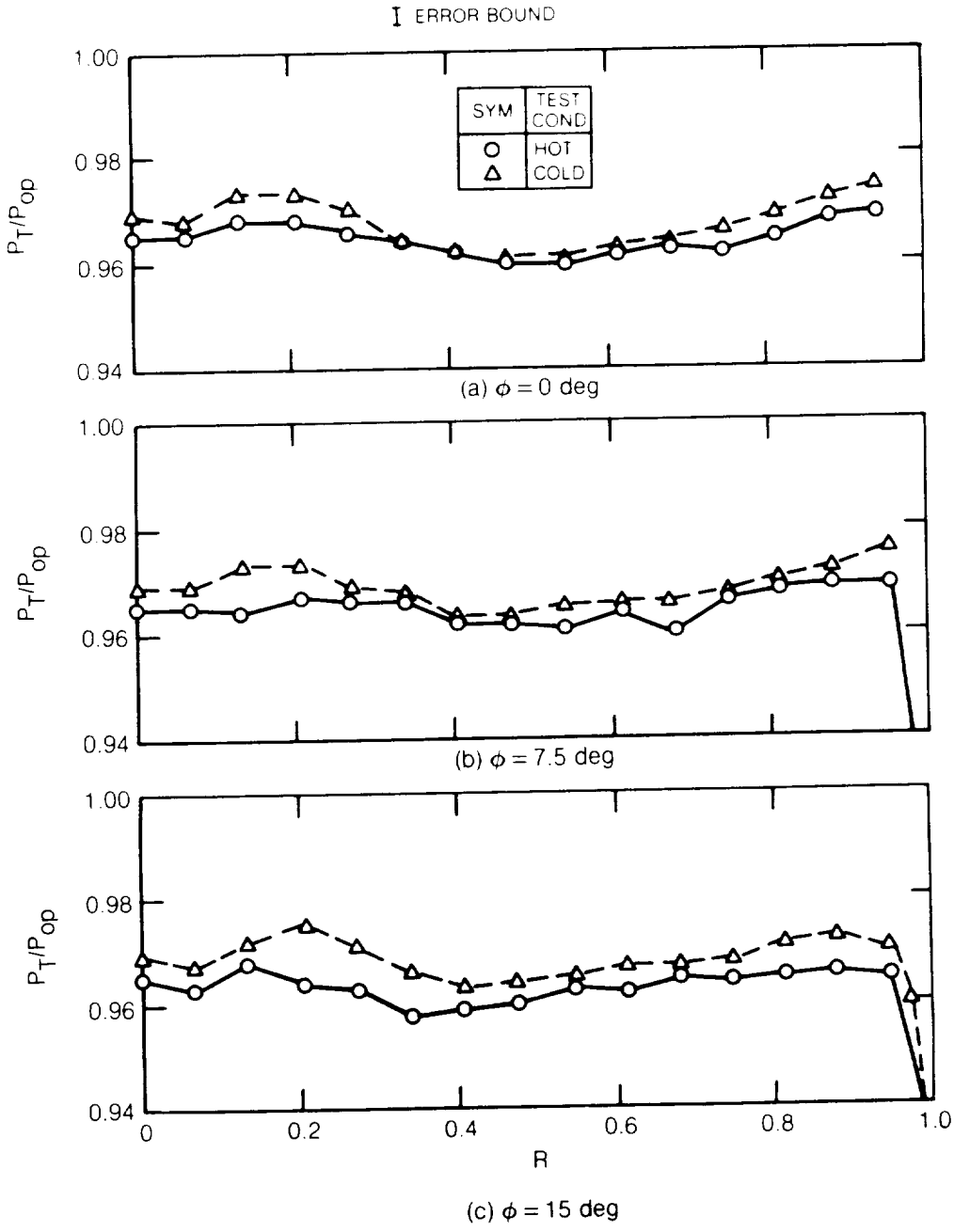

Figure 28 — Total Pressure Distributions for Hot and Cold Flow Test Conditions at Plume Plane Station 3

SYMBOL	MEANING
CCW	COUNTER CLOCKWISE
CW	CLOCKWISE
B L	BOUNDARY LAYER

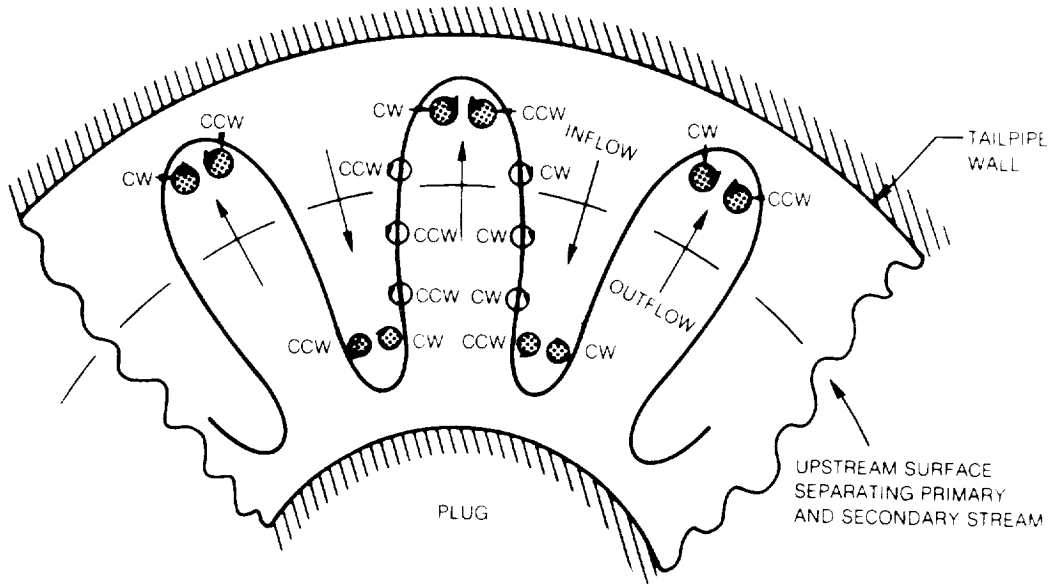

a) OBSERVED LOBE EXIT VORTEX SYSTEM AS VIEWED FROM NOZZLE EXIT

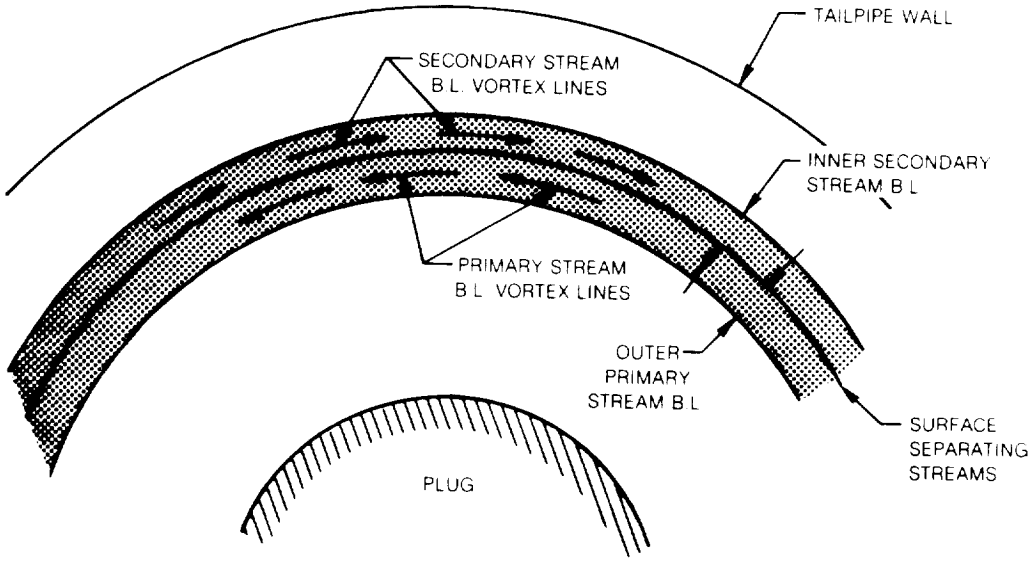

b) BOUNDARY LAYER VORTEX LINE ORIENTATIONS UPSTREAM OF LOBES AS VIEWED FROM NOZZLE EXIT

Figure 29 — Mixer Nozzle Vortex System

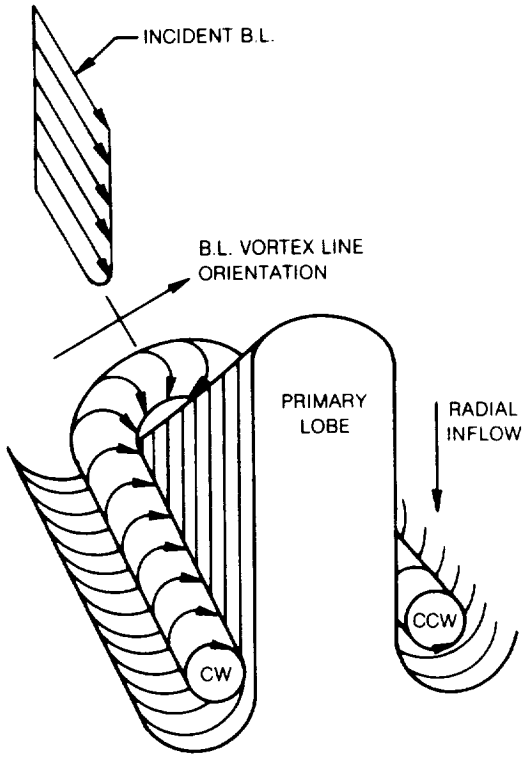

a) SCHEMATIC REPRESENTATION OF SECONDARY STREAM HORSESHOE VORTEX FORMATION

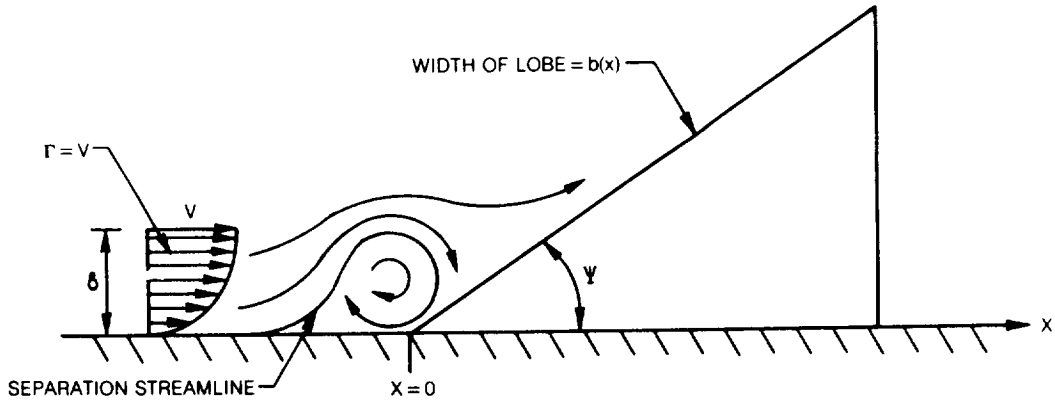

b) PARAMETERS AFFECTING VORTEX SIZE AND INTENSITY

Figure 30 — Lobe Horseshoe Vortex Formation

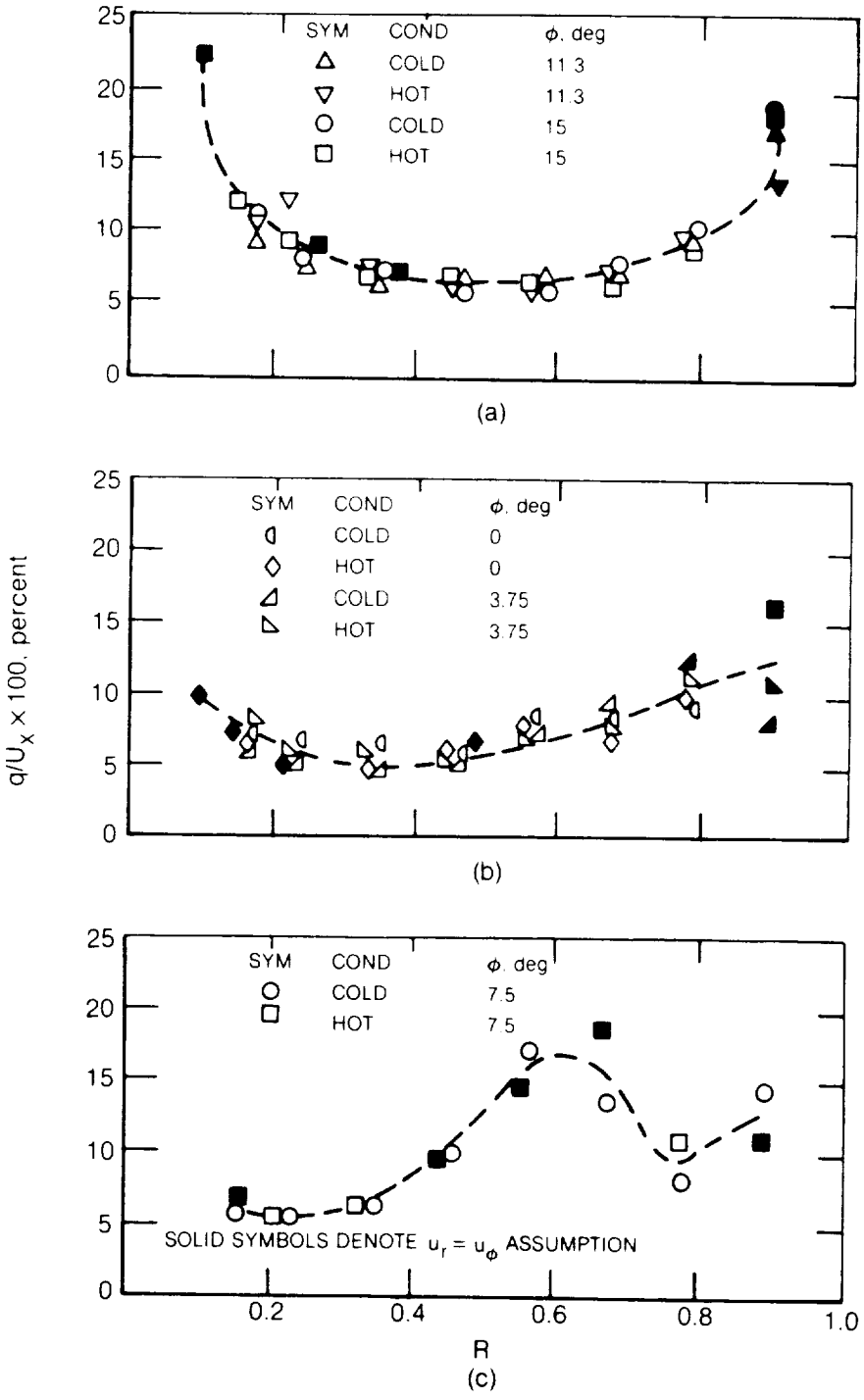

Figure 31 — Turbulence Level Distributions at Station 1; $q = \sqrt{u_x^2 + u_r^2 + u_\phi^2}$

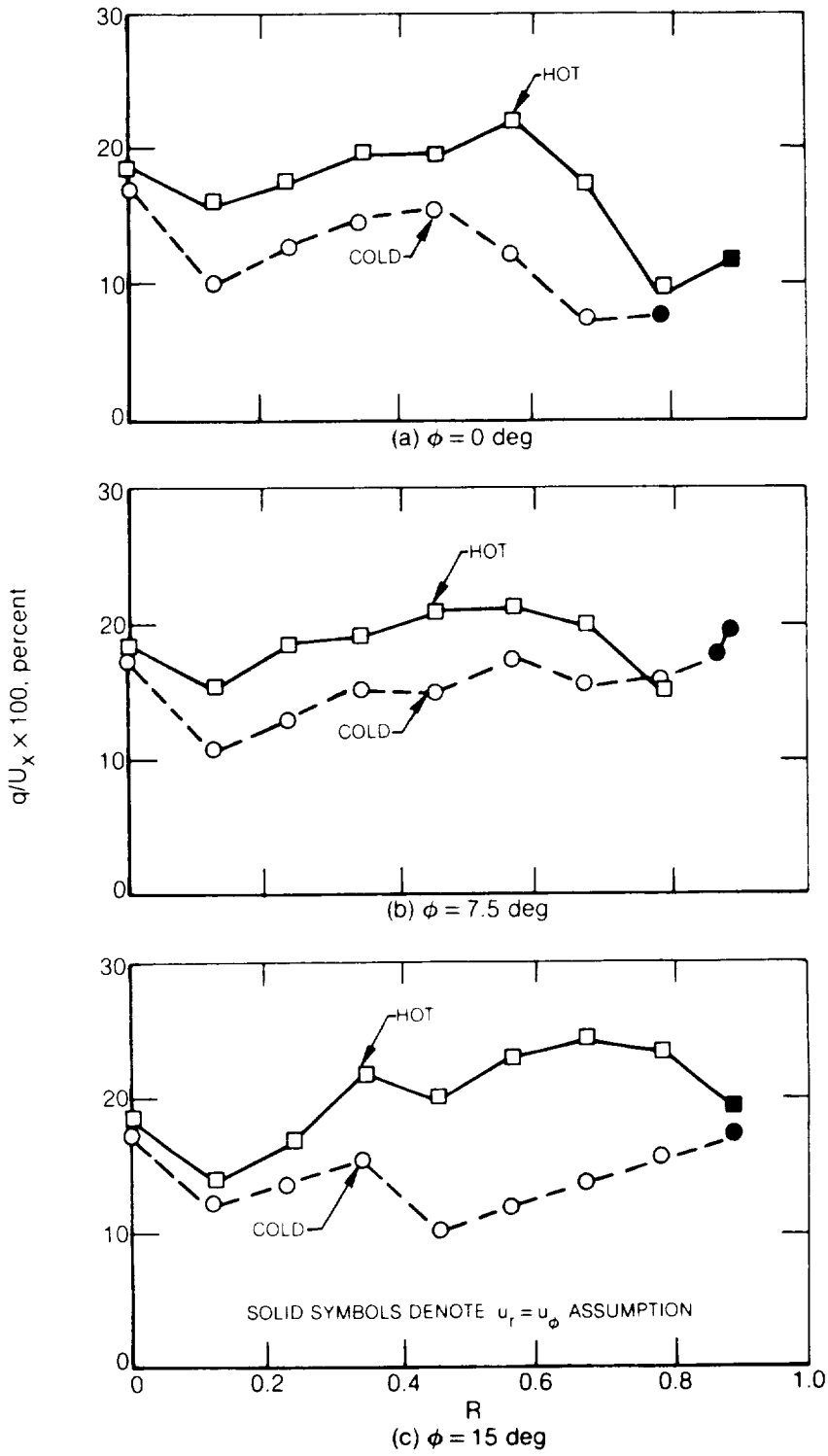

Figure 32 — Turbulence Level Distributions at Station 2; $q = \sqrt{u_x^2 + u_r^2 + u_\phi^2}$

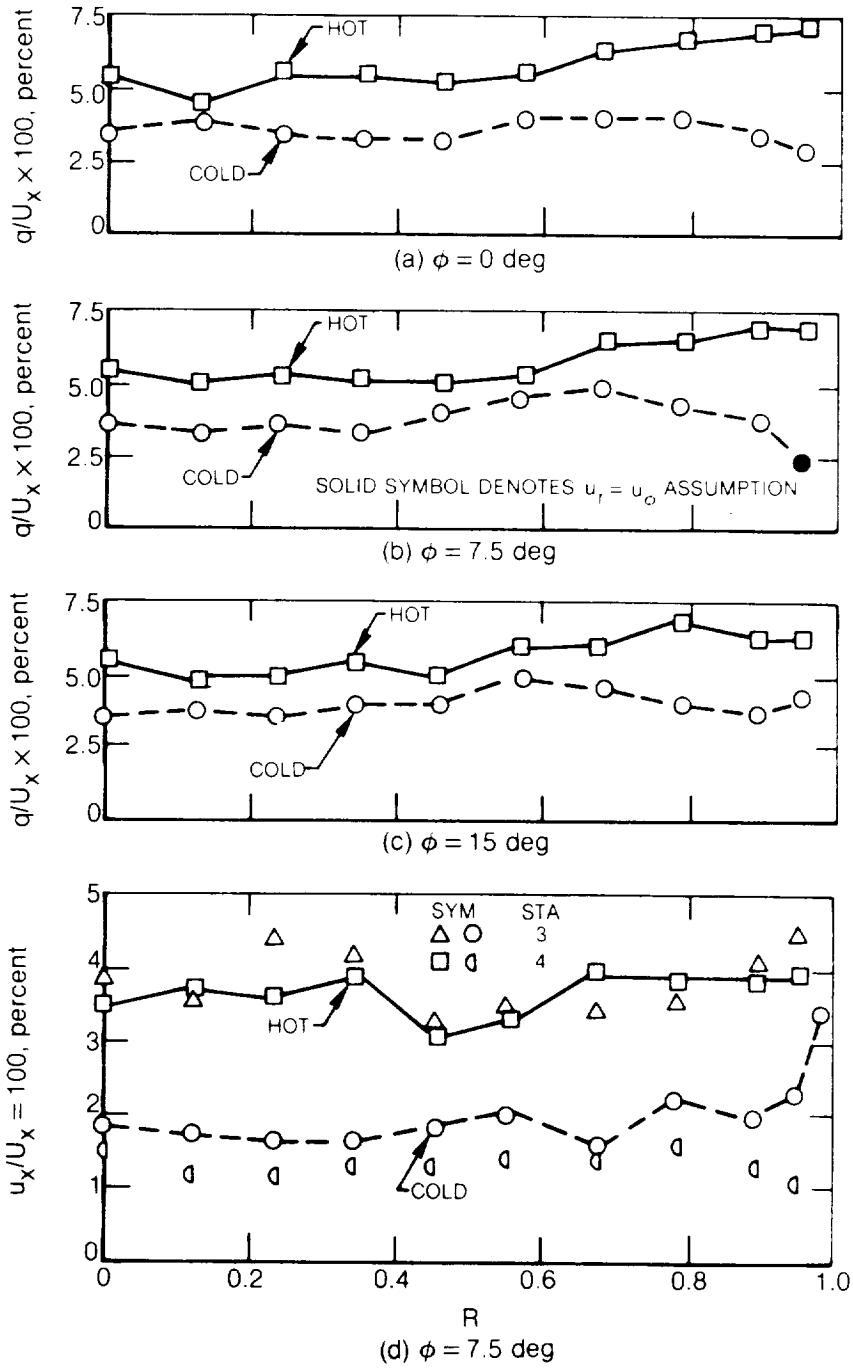

Figure 33 — Turbulence Level Distributions at Stations 3 and 4; $q = \sqrt{u_x^2 + u_r^2 + u_\phi^2}$

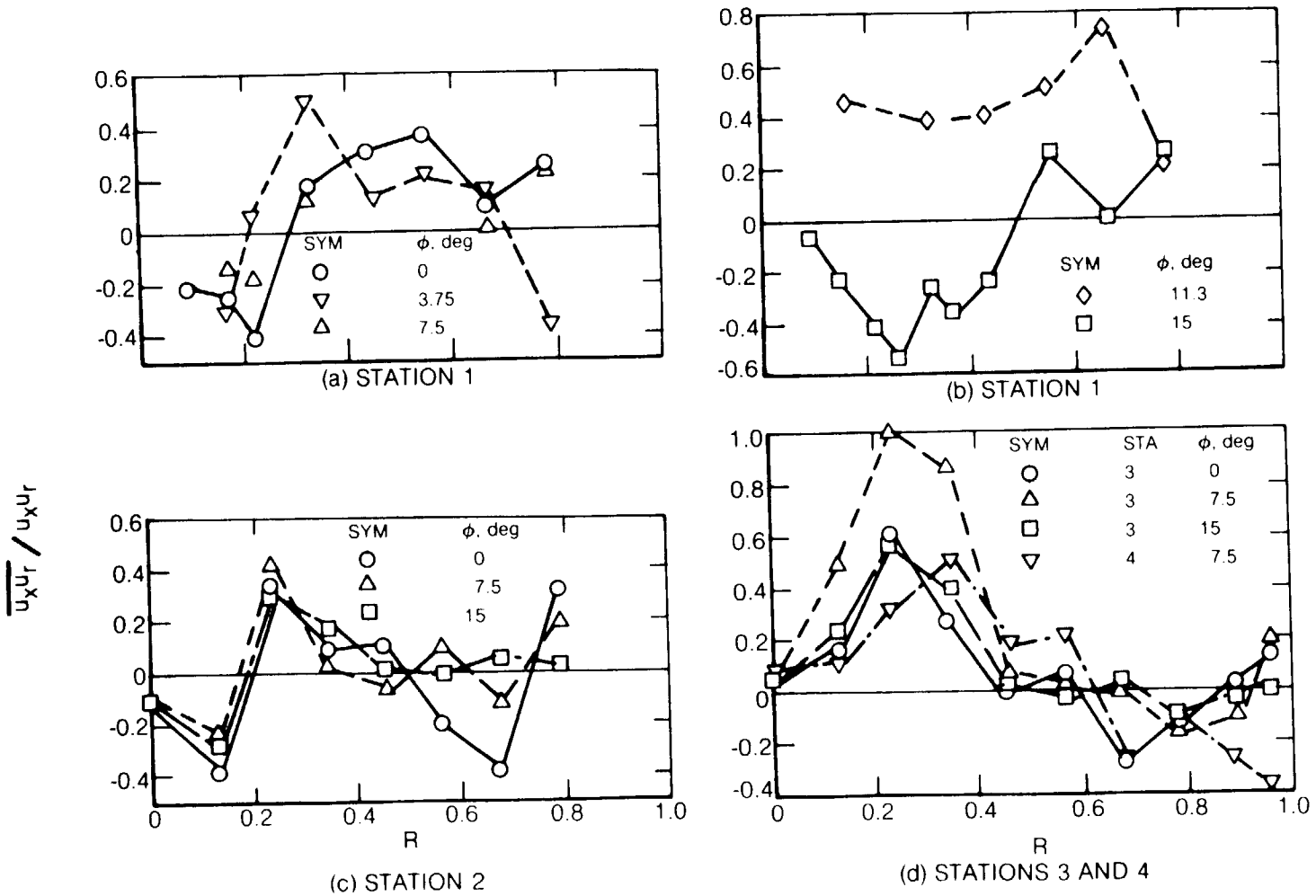

Figure 34 — Axial-Radial Turbulence Correlation Coefficient Distributions for Hot Flow Test Conditions

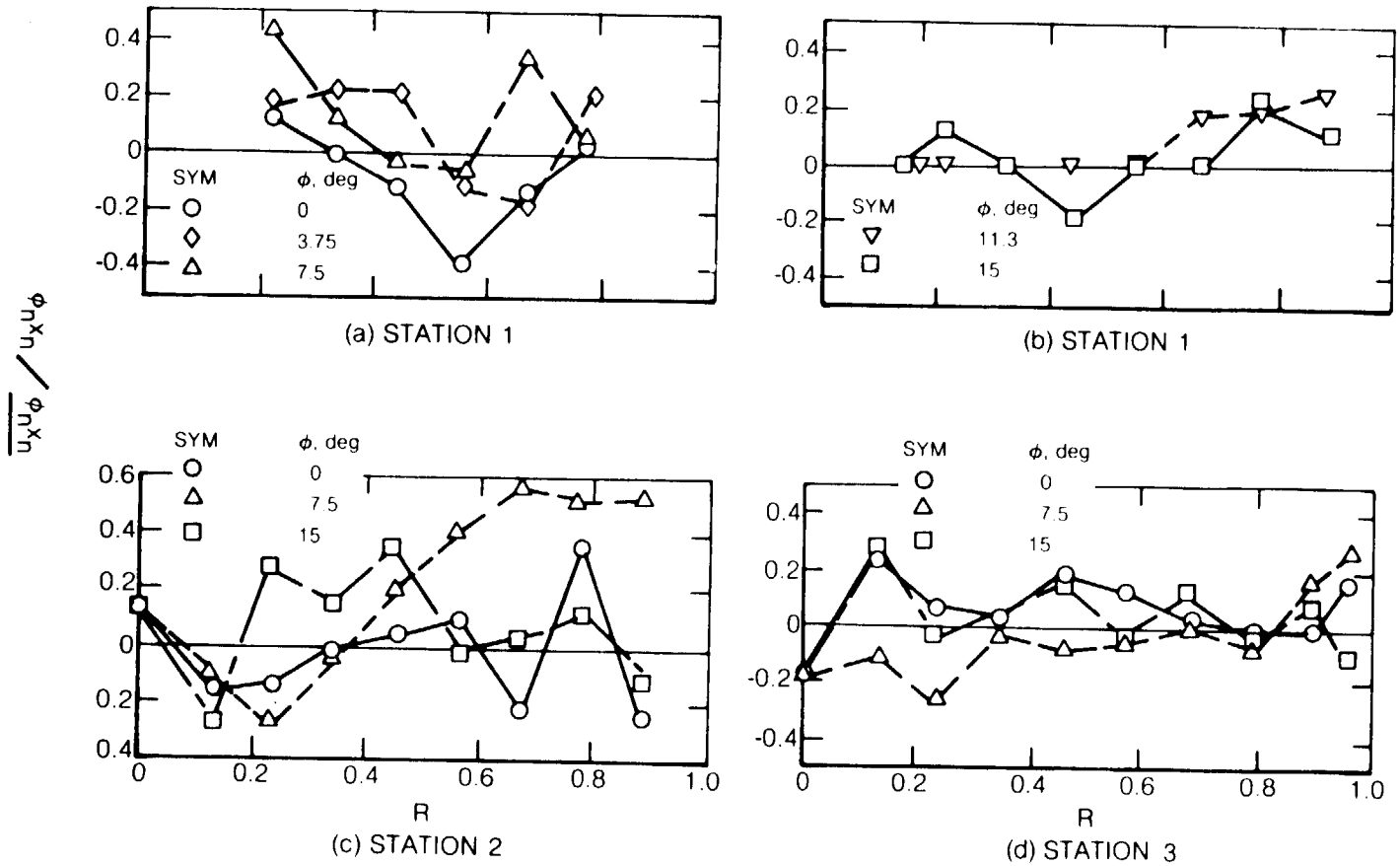

Figure 35 — Axial-Azimuthal Turbulence Correlation Coefficient Distributions for Hot Flow Test Conditions

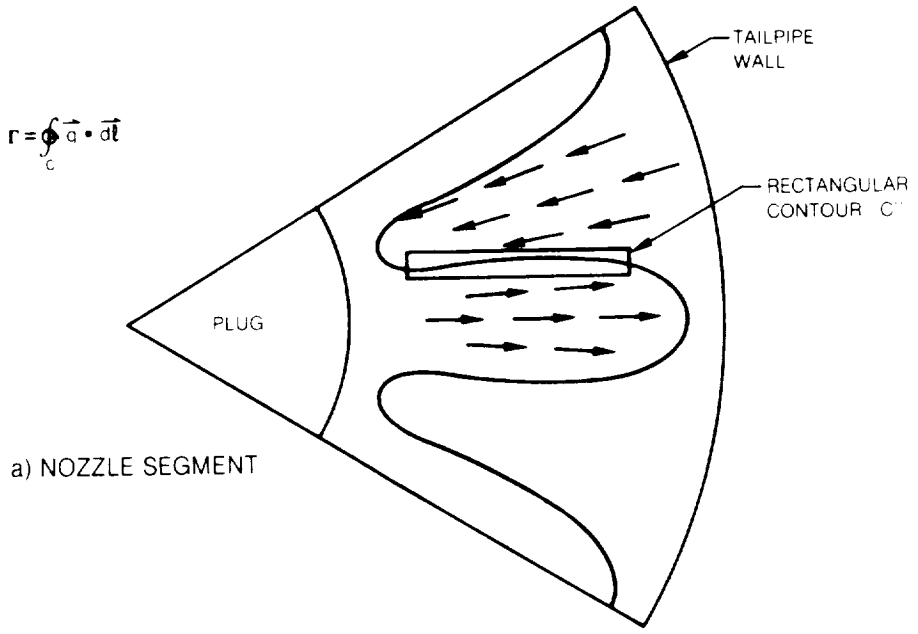

a) NOZZLE SEGMENT

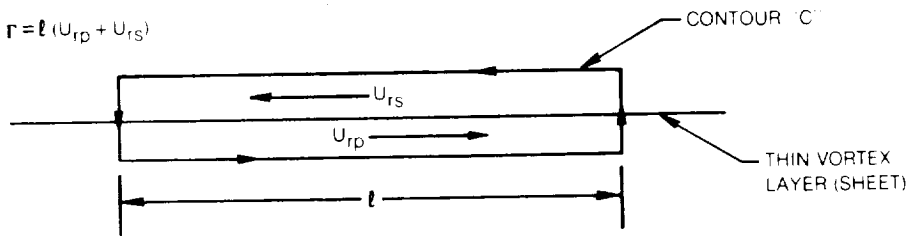

b) VORTEX LAYER REPRESENTATION OF VELOCITY DISCONTINUITY WITHIN CONTOUR "C"

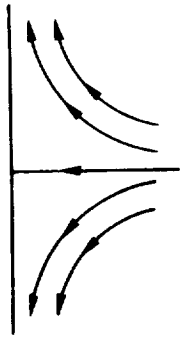

c) IRROTATIONAL STAGNATION POINT FLOW

Figure 36 — Lobe Exit Flow

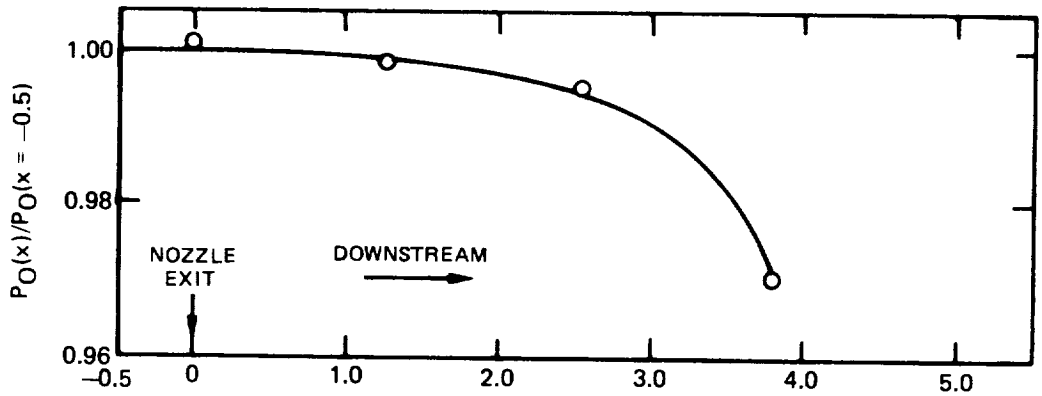

(a) AXIAL TOTAL PRESSURE DISTRIBUTION

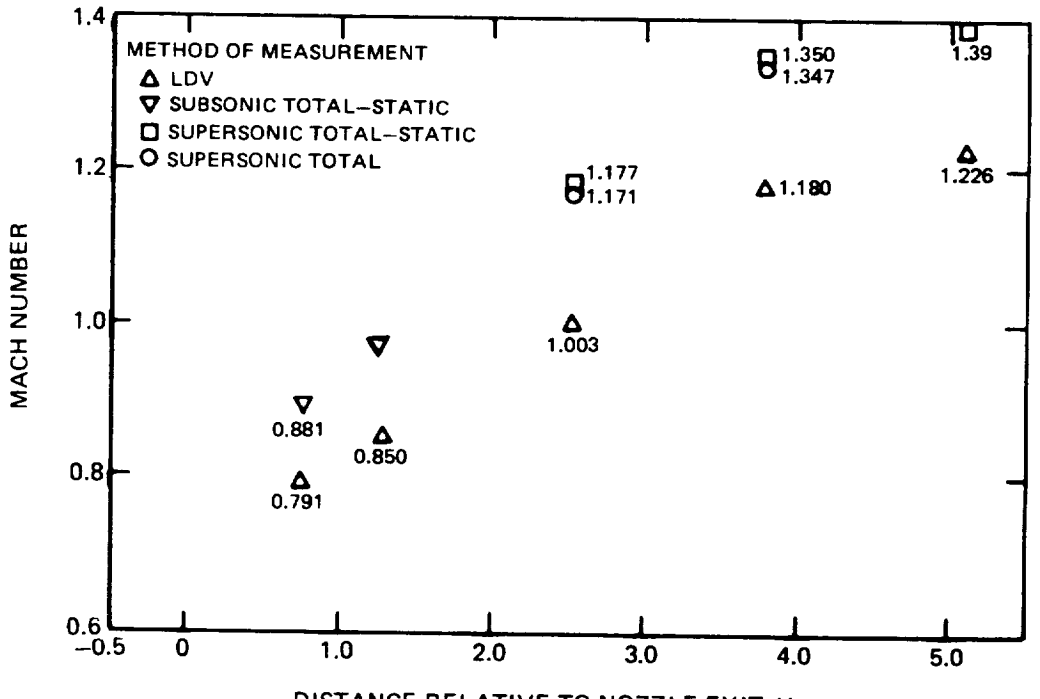

(b) AXIAL MACH NUMBER DISTRIBUTION
(PITOT–LDV COMPARISON)

Figure 37 — LDV Measurement Accuracy Assessment for Mixer Nozzle in Transonic Flow

1. Report No.	2. Government Accession No.	3. Recipient's Catalog No.
NASA CR-3492		

4. Title and Subtitle	5. Report Date
TURBOFAN FORCED MIXER-NOZZLE INTERNAL FLOWFIELD I - A BENCHMARK EXPERIMENTAL STUDY	April 1982
	6. Performing Organization Code

7. Author(s)	8. Performing Organization Report No.
Robert W. Paterson	None
	10. Work Unit No.

9. Performing Organization Name and Address	11. Contract or Grant No.
United Technologies Research Center East Hartford, Connecticut 06108	NAS3-20951
	13. Type of Report and Period Covered
12. Sponsoring Agency Name and Address	Contractor Report
National Aeronautics and Space Administration Washington, D.C. 20546	14. Sponsoring Agency Code
	505-32-12

15. Supplementary Notes

Final report. Project Manager, Louis A. Povinelli, Aerothermodynamics and Fuels Division, NASA Lewis Research Center, Cleveland, Ohio 44135.

16. Abstract

This report describes an experimental investigation of the flowfield within a model turbofan forced-mixer nozzle. The objective of the study was to provide detailed velocity and thermodynamic state variable data for use in assesing the accuracy and assisting the further development of computational procedures for predicting the flowfield within mixer nozzles. Velocity and temperature data suggested that the nozzle mixing process was dominated by circulations (secondary flows) of a length scale on the order of the lobe dimensions which were associated with strong radial velocities observed near the lobe exit plane. This report, as Volume I of a three volume series, constitutes a self-contained treatment of the "benchmark" model mixer experiment conducted for code assessment purposes. Volume II, subtitled "Computational Fluid Dynamic Predictions" provides detailed comparisons of the present experimental results with prediction while Volume III, subtitled "A Computer Code for 3-D Mixing in Axisymmetric Nozzles" describes the code used for prediction.

17. Key Words (Suggested by Author(s))	18. Distribution Statement
Turbofan engine Mixer nozzles	Unclassified - unlimited STAR Category 34

19. Security Classif. (of this report)	20. Security Classif. (of this page)	21. No. of Pages	22. Price*
Unclassified	Unclassified	130	A07

* For sale by the National Technical Information Service, Springfield, Virginia 22161

NASA-Langley, 1982